UNIVERSITY OF CALIFORNIA SAN DIEGO

Engineering Micro/Nanorobots Towards Biomedical Applications: Targeted Delivery, Surgery and Detoxification

A dissertation submitted in partial satisfaction of the requirements for the degree

Doctor of Philosophy

in

NanoEngineering

by

Fernando Soto

Committee in charge:

Professor Joseph Wang, Chair
Professor Yi Chen
Professor Henrik I. Christensen
Professor Mercedes T. Oropeza-Guzman
Professor Mike Tolley
Professor Liangfang Zhang

2019

The Dissertation of Fernando Soto is approved, and it is acceptable in quality and form for publication on microfilm and electronically:

_____

_____

_____

_____

_____

_____

Chair

University of California San Diego

2019

DEDICATION

To my family and the illusion of free will.

EPIGRAPH

“diré las palabras que se dicen

y comeré las cosas que se comen

y soñaré las cosas que se sueñan

y sé muy bien que no estarás”

Julio Cortazar

TABLE OF CONTENTS

SIGNATURE PAGE iii
DEDICATION iv
EPIGRAPH v
TABLE OF CONTENTS vi
LIST OF FIGURES viii
ACKNOWLEDGEMENTS x
VITA xiii
ABSTRACT OF THE DISSERTATION xiv
Chapter 1 Introduction 1
1.1 Micro/Nano Robotics Opportunities and Challenges 1
1.2 Powering devices at the micro/nano scale 2
1.3. Motion Control of Micro/Nanomotors 5
1.4 References 8
Chapter 2. Use of robotic platform for transport microscale transport 13
2.1 Introduction 13
2.2 Experimental Methods 15
2.3 Experimental Results 17
2.4 Conclusions 27
2.5 References 29
Chapter 3 Use of robots platforms for surgery 31
3.1 Acoustic microcannons: Toward advanced microballistics 31
3.1.1 Introduction 31
3.1.2 Experimental Methods 33
3.1.3 Experimental Results 37
3.1.4 Conclusions 51
3.1.5 References 53
3.2 Mechano-chemical blood clot degradation by acousto-ballistic microengines 57
3.2.1 Introduction 57
3.2.2 Experimental Methods 58

3.2.3 Experimental Results 61
3.2.4 Conclusions 68
3.2.5 References 68
3.3 Non-invasive Transdermal Delivery System of Lidocaine Using an Acoustic Droplet-Vaporization Based Wearable Patch 72
3.3.1 Introduction 72
3.2.2 Experimental Methods 73
3.3.3 Experimental Results 77
3.3.4 Conclusions 84
3.3.5 References 85
Chapter 4. Use of robotic plataform for Decontamination 89
4.1 Introduction 89
4.2 Experimental Methods 91
4.3 Experimental Results 95
4.4 Conclusions 110
4.5 References 111
Chapter 5- Summary and Perspectives 115
5.1 Summary 115
5.2 Perspectives 116

LIST OF FIGURES

Figure 2.1 Schematic of the nanoshell fabrication method and operation. 17

Figure 2.2. Effect of the motor density of propulsion..... 19

Figure 2.3. Effect of the motor size on the nanoshell propulsion. 21

Figure 2.4. Magnetic guidance of the nanoshells 23

Figure 2.5. Nanoshell internalization and propulsion inside a MCF-7 GFP cancer cell. . 26

Figure 3.1.1. Ultrasound triggered Microcannons 37

Figure 3.1.2. Schematic of the Ultrasound Set up. 38

Figure 3.1.3. SEM characterization of multiple nanobullet-loaded Microcannons 39

Figure 3.1.4. Time-lapse images Microcannon activation. 40

Figure 3.1.5. Tunable nB loading density in the gel matrix 41

Figure 3.1.6. US-triggered firing inside a tissue phantom gel matrix..... 43

Figure 3.1.7. Experimental and theoretical behaviors. 44

Figure 3.1.8. Use of microcannon patch for OP nerve agent decontamination. 50

Figure 3.2 1. Use of cardiobullet as a surgical tool for unclogging blocked vessels. 61

Figure 3.2 2. Static Assay Evaluation of blood clot degradation..... 63

Figure 3.2 3. Fabrication and characterization of clogged microfluidic channel 64

Figure 3.2 4. Unclogging microfluidic blocked mimicking vessels. 66

Figure 3.3.1. Principles of the wearable ADV-based drug-delivery patch. 77

Figure 3.3.2. Proposed translational system towards future tests 78

Figure 3.3 3. Application of ADV patch..... 78

Figure 3.3.4. Characterization of ADV patch. 79

Figure 3.3.5. Square wave voltammograms for different concentrations of lidocaine. 80

Figure 3.3.6. ADV-based lidocaine delivery evaluation..... 81

Figure 3.3.7. ADV delivery in pigskin model.. 84

Figure 4.1. Mechanism for the formation of the rotibot. 95

Figure 4.2. Transfer of microbeads from the cilia onto the inner mouth lip..... 96

Figure 4.3. Polydopamine coated fluorescent microbeads based rotibots 97

Figure 4.4. Time-lapse micrographs of a typical cilia stroke pattern. 98

Figure 4.5. Rotibot enabled fluid mixing and hydrodynamics. 99

Figure 4.6. Visualization of mixing generated by freely swimming rotibot..... 100

Figure 4.7. Modeling the rotibot. 102

Figure 4.8. Rotifer fluid mixing experiment and modeling comparison. 104

Figure 4.9. Lysozyme-modified rotibot-based antibacterial treatment..... 106

Figure 4.10. Use of rotibots for chemical pollutant remediation. 108

Figure 4.11. Increased motility of rotibot under influence of caffeine. 109

ACKNOWLEDGEMENTS

I want to acknowledge my advisor professor Joseph Wang for giving me the life-changing opportunity to work on his lab. Through his advice and patience, I have accomplished my dream to pursue a carrier in science. Working at this lab has shown me the importance of having inspiring mentors and invested team members, as it takes a whole lab community to train a scientist. I am very grateful for having an interdisciplinary education where I could explore completely new ideas and be on the cutting edge of science.

I want to thank my lab mates, classmates and undergrad researcher that are too numerous to mention, but I will make a special mention for the great mentors who took me under their wings during my first year at UCSD, this group is composed of Sirilak, Victor and Jair. Without their guidance I would not have been able to transition into a high standard of professionalism and dedication required to succeed in the group.

I offer special thanks to my committee for their support and advice through my dissertation, and also Dana Jimenez, who in my opinion, is the greatest asset of the Nanoengineering department.

UCSD is a wonderful place to grow as a scientist, as it offer me multiple groups to grow, as the Contextual Robotics Institute and Robograds student organization, where I was exposed to cutting edge research in robotics. I also got excellent traing through the IGE center and the Rady School of Business, that change the way I aproach problem selection. Finally, I want to thank my collegues at the Jacobs Graduate Student Concil. In the past two years we achieved great success with our programs, in particular the JGSC student council award.

In addition, I would like to thank the MEXUS-CONACYT fellowship for providing funding for my graduate studies. I also thank the Gordon Center for recognizing my work and granting me a very generous financial award.

My graduation was possible, due to the support and encouragement from my family members, who are my key inspiration for persuing the idea of a good and fulfilling life.

Chapter 1 is based, in part, on the material as it appears in Advanced Functional Materials, 2019, by Chuanrui Chen, Fernando Soto, Emil Karshalev, Jinxing Li, Joseph Wang. The dissertation author was the primary investigator and author of this paper.

Chapter 2 is based, in part, on the material as it appears Nanoscale, 2016, Fernando Soto, Gregory L Wagner, Victor Garcia-Gradilla, Kyle T Gillespie, Deepak R Lakshmipathy, Emil Karshalev, Chava Angell, Yi Chen, Joseph Wang. The dissertation author was the primary investigator and author of this paper.

Chapter 3.1 is based, in part, on the material as it appears ACS Nano, 2015, Fernando Soto, Aida Martin, Stuart Ibsen, Mukanth Vaidyanathan, Victor Garcia-Gradilla, Yair Levin, Alberto Escarpa, Sadik C Esener, Joseph Wang. and Advanced Materials Technologies, 2017 Fernando Soto, Rupesh K. Mishra, Robert Chrostowski, Aida Martin, Joseph Wang. The dissertation author was the primary investigator and author of these papers.

Chapter 3.3 is based, in part, on the material as it appears Small, 2018, Fernando Soto, Itthipon Jeerapan, Cristian Silva-López, Miguel Angel Lopez-Ramirez, Ingrid Chai,

Lu Xiaolong, Jian Lv, Jonas F Kurniawan, Ian Martin, Krishnan Chakravarthy, Joseph Wang. The dissertation author was the primary investigator and author of this paper.

Chapter 4 is based, in part, on the material as it appears Advanced Functional Materials, 2019, Fernando Soto, Miguel Angel Lopez-Ramirez, Itthipon Jeerapan, Berta Esteban-Fernandez de Avila, Rupesh Kumar Mishra, Xiaolong Lu, Ingrid Chai, Chuanrui Chen, Daniel Kupor, Amir Norhani, Joseph Wang. The dissertation author was the primary investigator and author of this paper.

Chapter 5 is based, in part, on the material as it appears in Advanced Functional Materials, 2019, by Chuanrui Chen, Fernando Soto, Emil Karshalev, Jinxing Li, Joseph Wang. The dissertation author was the primary investigator and author of this paper.

VITA

2013 Bachelor of Science, Tijuana Institute of Technology, México

2015 Master of Science, University of California San Diego

2019 Doctor of Philosophy, University of California San Diego

SELECTED PUBLICATIONS

1. Chen, C., Soto, F., Karshalev, E., Li, J. and Wang, J., 2019. Hybrid Nanovehicles: One Machine, Two Engines. Advanced Functional Materials, 29(2), p.1806290.
2. Soto, F., Wagner, G.L., Garcia-Gradilla, V., Gillespie, K.T., Lakshmipathy, D.R., Karshalev, E., Angell, C., Chen, Y. and Wang, J., 2016. Acoustically propelled nanoshells. Nanoscale, 8(41), pp.17788-17793.
3. Soto, F., Martin, A., Ibsen, S., Vaidyanathan, M., Garcia-Gradilla, V., Levin, Y., Escarpa, A., Esener, S.C. and Wang, J., 2015. Acoustic microcannons: Toward advanced microballistics. ACS nano, 10(1), pp.1522-1528.
4. Soto, F., Mishra, R.K., Chrostowski, R., Martin, A. and Wang, J., 2017. Epidermal Tattoo Patch for Ultrasound-Based Transdermal Microballistic Delivery. Advanced Materials Technologies, 2(12), p.1700210.
5. Soto, F., Jeerapan, I., Silva-López, C., Lopez-Ramirez, M.A., Chai, I., Xiaolong, L., Lv, J., Kurniawan, J.F., Martin, I., Chakravarthy, K. and Wang, J., 2018. Noninvasive Transdermal Delivery System of Lidocaine Using an Acoustic Droplet-Vaporization Based Wearable Patch. Small, 14(49), p.1803266.
6. Soto, F., Lopez-Ramirez, M.A., Jeerapan, I., Esteban-Fernandez de Avila, B., Mishra, R.K., Lu, X., Chai, I., Chen, C., Kupor, D., Nourhani, A. and Wang, J., 2019. Rotibot: Use of Rotifers as Self-Propelling Biohybrid Microcleaners. Advanced Functional Materials, p.1900658.

FIELDS OF STUDY

Major Field: Nanoengineering, Bioengineering, and Material Science

Studies in Nanoengineering

Professor Joseph Wang

ABSTRACT OF THE DISSERTATION

Engineering Micro/Nanorobots Towards Biomedical Applications: Targeted Delivery, Surgery and Detoxification

by

Fernando Soto

Doctor of Philosophy in NanoEngineering

University of California San Diego, 2019

Professor Joseph Wang, Chair

Over the past decade, micro/nanomotors have emerged as novel and versatile nanotools demonstrating considerable promise for many environmental and biological applications. This dissertation aims to demonstrate unique advantages of micro/nanorobot platforms.

The first theme focuses on developing the use of ultrasound propelled nanostructures for diverse applications, including “on-the-move” capture and the transport of multiple cargoes and internalization and movement inside live MCF-7 cancer cells.

The second theme explores the use of acoustically triggered microcannons. This principle was tested towards mechanochemical blood clot degradation and enhancing drug permeability through the epidermis.

The third theme describes the use of biohybrid robotics systems for detoxification and decontamination of environmental pollutants, including bacteria (*E. coli*), nerve agent (methyl paraoxon) and heavy metal ions (Cd and Pb) from aqueous solutions. In the not-so-distant future. Micro/nanorobots could serve as robust and versatile platform for potentially improving medical diagnosis and treatment.

Chapter 1 Introduction

1.1 Micro/Nano Robotics Opportunities and Challenges

Over the technological evolution of humankind people have combined different tools and energy sources to improve their living conditions and achieve breakthroughs previously thought impossible. For example, at the dawn of the agriculture revolution most works was performed by human labor alone. Nevertheless, the first human societies combined plows pulled by animals, and stone mills powered by wind, to significantly increase food production leading to the development of more advanced civilizations.[1]

Indeed, people have always strived to advance their technology to solve everyday tasks more efficiently. At the current moment, we are at the dawn of a new industrial revolution. Recent advances in robotics hold promise to improve our living conditions by allowing us to avoid dull and repetitive task and achieve breakthroughs previously thought impossible by performing tasks that are too dangerous or outside our human capabilities. Despite widespread adoption of robotic systems in all aspects of life, one of the unmet needs and significant challenge moving forward in robotics, relies on scaling down the size of these tools. Current robotic designs are dominated by robots as an assembly of discrete parts composed of hard links, junctions, and actuators. Much of their designs are rigid and limited to a few functionalities, making it hard for them to translate towards smallest scales where autonomy and simplicity are required. [2]

The realization of miniaturized robots of a few micrometers or less, would allow access to previously inaccessible places and serve as a powerful microfabrication tools, and perform new activities that our current macroscale tools cannot do. For example, these

micro/nanorobot structures could access areas of the body that are inaccessible to large scale tools, and perform minimally invasive tasks such as targeted drug delivery or surgery.[3]

Nanorobots are nano/micron size machines that convert energy into controlled and unidirectional locomotion and actuation, intended to perform tasks in the service of specific targets. In particular, medical nanorobotics abilities have progressed regarding the energy efficiency, complexity and the precision of movements, as well as the task they can achieve; The state-of-the-art motile microrobots have proven successful for performing diverse tasks including transport and delivery of cargo, application of mechanical force for manipulation or deformation, and enhance fluid mixing in small volumes. Such developments illustrate that micro-robotic platforms are not just exciting and promising but also highly capable and functional at this early stage.[5-10]

The biggest challenge to apply micro/nanomotors in real-life applications still relies on how to power such tiny machines in a compatible fashion to their designated environment. This will require new developments and multidisciplinary collaboration bridging the gap between biotechnology nanotechnology, and chemical sciences.

1.2 Powering devices at the micro/nano scale

Researchers have devoted time and energy toward expanding the biocompatibility, energy efficiency and identifying the specific niche where micro/nanorobots can present unique advantages. Central to any robotic design is the motor that convert fuel, be it chemical or physical, into kinetic energy in a controlled manner producing movement or

other physical change. When trying to design new motors, we should consider that they faced distinct challenge that those macroscopic 'controllable' Newtonian motion machines, as these objects are dominated by gravity and inertia. at microscopic scales, viscous forces dominate over inertial forces when objects are relatively small, and Brownian motion can even dominate over directional motion. The critical design aspect that has allowed solving these challenges rely in asymmetric energy conversion,

Multiple paths to power nanomachines have been taken by utilizing sources of energy stimuli. Synthetic micro-/nanomotors can harvest energy from their surroundings and convert it to autonomous motion.[11-14] They are classified according to their significantly different power sources, varying from catalyzed chemical reactions to applied external fields. A classic approach to power nanomachines is the use of external physical inputs, such as ultrasound waves or magnetic fields. Tailored nanostructure designs are incorporated into nanomachines that can respond to these external physical inputs. For example, an asymmetric geometry is usually required in ultrasound powered nanomotors to facilitate locomotion *via* the establishment of pressure gradients,[15,16] microstreaming,[17,18] or bubble cavitation.[19,20] The ultrasound actuation offers a robust propulsion strategy, fast locomotion and preconcentrating capability[21-25], despite constraints such as specialized equipment, limited chamber size and the difficulties in individual manipulation.

Magnetic actuation is another excellent candidate to power micro/nanomotors. The colloidal magnetic particles align in external uniform magnetic field and are readily actuated akin a fish’s tail or snake’s body by oscillating the magnetic field. Later, a variety

of magnetic propelled micro/nanomotors emerged, ranging from flexible tails[26-28] to magnetic helical swimmers.[29-31] The magnetic field approach offers robust spatial maneuverability, efficient propulsion regardless of chemical environment, and even presents initial steps towards automation.[32-34] However, magnetically powered micromotors suffer limitations such as small power output, requirement of complex manipulation equipment, slow propulsion speed.

In general, physical propulsion methods are ideal for applications where precision, spatial maneuverability and long-lasting operation in diverse environments is desired, such as microsurgery, cargo transport or nanofabrication as their propulsion is not affected by high ionic strength environments, catalyst poisoning and biofouling or prolonged use. However, physical propulsion strategies also experience shortcomings due to their scalability issues and the requirement of complex actuation systems designating their use to specialized settings. In addition, it is still an open question if crucial external physical inputs can be established in the human body in a predictable and controllable manner without causing obvious side effects.

Chemical compounds are abundant in biological and environmental scenarios, thus powering micro/nanomotors by using chemical reactions represents another major route towards nanoscale propulsion. Chemically powered micro/nanomotors rely on the conversion of fuel into motion, based on noble metal enabled catalysis or active metal replacement reactions, which result in an asymmetric concentration gradient or microbubble ejection.[39-40] In general, two factors are indispensable in the chemically powered micro/nanomotor. Firstly, an asymmetric structure is required to break the

geometrical symmetry and allow for the formation of chemical gradients or bubble streams. Secondly, a chemical reaction with a rapid product formation rate is needed to generate a strong enough propulsion force. A variety of bimetallic nanowires, Janus particles, or hollow microtubes[41-44] have been developed for chemically-based propulsion at the microscale. Their motion relies on the decomposition or reaction of chemical fuels, including hydrogen peroxide (H_2O_2)[45,46], sea water[47-49], glucose[50-51], urea[52-53] or gastrointestinal fluid.[54-56] The chemical propulsion stimuli are ideal for applications where autonomy and scalability are paramount, such as drug delivery[57-59] or environmental clean-up and detoxification.[60-63] Nevertheless, their applicability suffers shortcomings due to the difficulty in modulating the propulsion behavior *in situ*, the toxicity of certain fuels and the short lifespan caused by the exhaustion of the fuel. Moreover, such strategies could induce an adverse response in *in vivo* conditions, such as changes of the local chemical environment.[64] More recently, the concept of biohybrid systems based on the coupling of motile microorganisms with synthetic structures, has offer unique capabilities, as microorganisms already possess locomotion, energetic autonomy, and sensing capabilities that are well beyond the state of the art in engineering. Nevertheless, their operation is limited to biocompatible environments and their functionality is limited by each particular microorganism and they remain hard to control.

1.3. Motion Control of Micro/Nanomotors

Chemically powered micromotors move spontaneously when in contact with the fuel solution hence using a second hybrid trigger to control their moving behavior is of importance to improve their overall performance. In this direction, a large number of

studies have focused on using external physical stimuli to achieve on-demand control and collective behavior over chemically propelled micromachines. Foundational reports in the field of active motion management by using hybrid triggers. For instance, the use of dual stimuli offers multiple practical solutions to precisely guide micromotors through predetermined paths. Chemically and physically propelled micromotors have been integrated with diverse ferromagnetic segments (Ni, Fe, Co) to establish control over the micromotor directionality by aligning them with a magnetic field or *via* magnetic torque applied to the motor structure. Such magnetic fields can be produced by a magnetic bar which offer directly manipulation or with a Helmholtz coil that produces a highly accurate three-dimensional control.[65-70]

Another example of the use of external stimuli to modulate propulsion of chemically powered micro engines relies on the use of acoustic fields. Ultrasound can cavitate, coalesce, and collapse gas bubbles. Work by the Wang group used this principle to hinder the bubble evolution and ejection process on the opening of the microtubular motor responsible for propulsion.[71] This method manifests itself nearly instantaneously (within 0.1 s) with fully reversible ON/OFF activation and speed modulation. Furthermore, unlike thermal or optical stimuli, this approach does not affect the fuel or reaction rate allowing for maintaining chemical propulsion integrity. More recent studies have shown that apart from ON/OFF motion, the ultrasound fields can induce oscillations of bubble aggregates and hinder bubble forming phenomena of the microrocket resulting in change of directionality.[72]

Moreover, the use of acoustic fields can lead to the exhibition of collective behavior of micromotors. This phenomenon was demonstrated with chemically propelled nanowires[73,74] and magnetic nanomotors.[75] For both cases, the swarming was generated by pressure gradients produced by a standing wave, which triggers the rapid migration and assembly of nanomotor around the nearest pressure node. Changing the applied frequency results in the collective movement of the swarm to the new node position.[76] Interestingly, the addition of UV light while chemically propelled nanowires are held in a swarm by the acoustic field, results in a "firework" like behavior.[77] Different parameters including the intensity, excitation voltage, transmission, and density of materials produced different swarming behavior.

Chapter 1 is based, in part, on the material as it appears in Advanced Functional Materials, 2019, by Chuanrui Chen, Fernando Soto, Emil Karshalev, Jinxing Li, Joseph Wang. The dissertation author was the primary investigator and author of this paper.

1.4 References

1. N. H. Yuval, Sapiens: A brief history of humankind, McClelland & Stewart, 2014.

2. J.M. Diamond, J.M. Guns, germs, and steel, 1999.

3. B. Bryson, R. Matthews, A short history of nearly everything, Broadway Books, 2003.

4. J.M. Jordan, 2016. Robots. The MIT Press.

5. J. Wang, Nanomachines: fundamentals and applications, John Wiley & Sons, 2013.

6. M. Guix, C. C. Mayorga-Martinez, A. Merkoçi, Chem. Rev. 2014, 114, 6285.

7. J. Li, B. Esteban-Fernández de Ávila, W. Gao, L. Zhang, J. Wang, Science Robotics 2017, 2, eaam6431.

8. E. Karshalev, B. Esteban-Fernández de Ávila, J. Wang, J. Am. Chem. Soc. 2018, 140, 3810.

9. H. Wang, M. Pumera, Adv. Funct. Mater. 2018, 28, 1705421.

10. F. Peng, Y. Tu, D. A. Wilson, Chem. Soc. Rev. 2017, 46, 5289.

11. W. Wang, W. Duan, S. Ahmed, T. E. Mallouk, A. Sen, Nano Today 2013, 8, 531.

12. S. Sánchez, L. Soler, J. Katuri, Angew. Chem. Int. Ed. 2015, 54, 1414.

13. T. Xu, W. Gao, L. P. Xu, X. Zhang, S. Wang, Adv. Mater. 2017, 29, 1603250.

14. S. Palagi, P. Fischer, Nat. Rev. Mater. 2018, 3, 113.

15.W. Wang, L. A. Castro, M. Hoyos, T. E. Mallouk, ACS Nano 2012, 6, 6122.

16. F. Soto, G. L. Wagner, V. Garcia-Gradilla, K. T. Gillespie, D. R. Lakshmipathy, E. Karshalev, C. Angell, Y. Chen, J. Wang, Nanoscale 2016, 8, 17788.

17. T. Qiu, S. Palagi, A. G. Mark, K. Melde, F. Adams, P. Fischer, Adv. Mater. Interfaces. 2017, 4, 1700933.

18. D. Ahmed, M. Lu, A. Nourhani, P. E. Lammert, Z. Stratton, H. S. Muddana, V. H. Crespi, T. J. Huang, Sci. Rep. 2015, 5, 9744.

19. J. J. Kwan, R. Myers, C. M. Coviello, S. M. Graham, A. R. Shah, E. Stride, R. C. Carlisle, C. C. Coussios, Small 2015, 11, 5305.

20. F. Soto, A. Martin, S. Ibsen, M. Vaidyanathan, V. Garcia-Gradilla, Y. Levin, A. Escarpa, S. C. Esener, J. Wang, ACS Nano 2015, 10, 1522.

21. V. Garcia-Gradilla, J. Orozco, S. Sattayasamitsathit, F. Soto, F. Kuralay, A. Pourazary, A. Katzenberg, W. Gao, Y. Shen, J. Wang, ACS Nano 2013, 7, 9232.

22. W. Wang, S. Li, L. Mair, S. Ahmed, T. J. Huang, T. E. Mallouk, Angew. Chem. Int. Ed. 2014, 53, 3201.

23. B. Esteban-Fernández de Ávila, A. Martín, F. Soto, M. A. Lopez-Ramirez, S. Campuzano, G. M. Vásquez-Machado, W. Gao, L. Zhang, J. Wang, ACS Nano 2015, 9, 6756.

24. K. J. Rao, F. Li, L. Meng, H. Zheng, F. Cai, W. Wang, Small 2015, 11, 2836.

25. F. Zhang, R. Mundaca-Uribe, H. Gong, B. E. F. D. Ávila, M. Beltrán-Gastélum, E. Karshalev, A. Nourhani, Y. Tong, B. Nguyen, M. Gallot, Y. Zhang, L. Zhang, J. Wang, Advanced Materials 2019, 31, 1901828.

26. W. Gao, S. Sattayasamitsathit, K. M. Manesh, D. Weihs, J. Wang, J. Am. Chem. Soc. 2010, 132, 14403.

27. B. Jang, E. Gutman, N. Stucki, B. F. Seitz, P. D. Wendel-García, T. Newton, J. Pokki, O. Ergeneman, S. Pané, Y. Or, and B. Nelson, Nano Lett. 2015, 15, 4829.

28. T. Li, J. Li, K. I. Morozov, Z. Wu, T. Xu, I. Rozen, A. M. Leshansky, L. Li, J. Wang, Nano Lett. 2017, 17, 5092.

29. L. Zhang, J. J. Abbott, L. Dong, B. E. Kratochvil, D. Bell, B. J. Nelson, Appl. Phys. Lett. 2009, 94, 064107.

30. D. Walker, B. T. Käsdorf, H.-H. Jeong, O. Lieleg, P. Fischer, Sci. Adv. 2015, 1, e1500501.

31. S. Tottori, L. Zhang, F. Qiu, K. K. Krawczyk, A. Franco-Obregón, B. J. Nelson, Adv. Mater. 2012, 24, 811.

32. D. Schamel, A. G. Mark, J. G. Gibbs, C. Miksch, K. I. Morozov, A. M. Leshansky,P. Fischer, ACS Nano 2014, 8, 8794.

33. F. Qiu, S. Fujita, R. Mhanna, L. Zhang, B. R. Simona, B. J. Nelson, Adv. Funct. Mater. 2015, 25, 1666.

34. A. Servant, F. Qiu, M. Mazza, K. Kostarelos, B. J. Nelson, Adv. Mater. 2015, 27, 2981.

35. X. Lu, F. Soto, J. Li, T. Li, Y. Liang, J. Wang, ACS Applied Materials & Interfaces 2017, 9, 38870.

36. X. Lu, K. Zhao, W. Liu, D. Yang, H. Shen, H. Peng, X. Guo, J. Li, J. Wang, ACS Nano 2019, 13, 11443.

37. X. Lu, A. Martin, F. Soto, P. Angsantikul, J. Li, C. Chen, Y. Liang, J. Hu, L. Zhang, J. Wang, Advanced Materials Technologies 2018, 1800374.

38 J. Li, I. Rozen, J. Wang, ACS nano, 2016, 10, 5619.

39. C. Chen, E. Karshalev, J. Guan, J. Wang, Small, 2018,1704252.

40. E. Karshalev, B. Esteban-Fernández de Ávila, J. Wang, JACS, 140, 3810.

41. S. Fournier-Bidoz, A.C. Arsenault, I. Manners, G.A. Ozin, Chem Commu, 2005, 4, 441.

42. J.G. Gibbs, Y.P. Zhao. Applied Physics Letters, 2019, 94, 163104.

43. W. Gao, S. Sattayasamitsathit, J. Orozco, J. Wang, JACS, 2011, 133, 11862.

44. H. Wang, M. Pumera, Chemical reviews, 2015, 115, 8704.

45. W.F. Paxton, K.C. Kistler, C.C. Olmeda, A. Sen, S.K St. Angelo,. Y. Cao,Mallouk, P.E. Lammert, V.H. Crespi, JACS, 2004, 126, 13424.

46. A.A. Solovev, Y. Mei, E. Bermúdez Ureña, G. Huang, O.G. Schmidt, 2009, Small, 5, 1688.

47. F. Mou, C. Chen, H. Ma, Y. Yin, Q. Wu, J. Guan, Angew. Chem. Int. Ed., 52, 7208.

48. W. Gao, X. Feng, A. Pei, Y. Gu, J. Li, J. Wang, Nanoscale, 2013, 5, 4696.

49. E. Chen, E. Karshalev, J. Li, F. Soto, R. Castillo, I. Campos, F. Mou, J. Guan, J. Wang, ACS Nano, 2016, 10, 10389.

50. D. Pantarotto, W.R. Browne, B.L. Feringa, Chem Comm, 2008, 13, 1533.

51. P.S. Schattling, M.A. Ramos-Docampo, V. Salgueiriño, B. Städler, ACS Nano, 2017, 11, 3973.

52. X. Ma, X. Wang, K. Hahn, S. Sánchez, ACS Nano, 2016, 10, 3597.

53. T. Patiño, N. Feiner-Gracia, X. Arqué, A. Miguel-López, A. Jannasch, T. Stumpp, E. Schäffer, L. Albertazzi, S. Sánchez, JACS, 2018, 140, 7896. 54. W. Gao, R. Dong, S. Thamphiwatana, J. Li, W. Gao, L. Zhang, J. Wang. ACS nano, 2015, 9, 117.

55. J. Li, S. Thamphiwatana, W. Liu, B.Esteban-Fernández de Ávila, , P. Angsantikul, E. Sandraz, E. Wang, T. Xu, F. Soto, V. Ramez, X. Wang, ACS nano, 2016, 10, 9536.

56. B.E.F., P de Ávila,. Angsantikul, J. Li, M.A. Lopez-Ramirez, D. Ramírez-Herrera, S. Thamphiwatana, C. Chen, J. Delezuk, R. Samakapiruk, V. Ramez, M. Obonyo. Nature communications, 2017, 8, p.272.

57. M. Luo, Y. Feng, T. Wang, J.Guan, Adv Funct Mat, 2018, 1706100.

58. K. Kim, J. Guo, Z. Liang, D. Fan, D Adv FuncT Mat, 2018, 1705867.

59. M. Medina-Sánchez, H. Xu, O.G. Schmidt, Ther Deliv, 2018, 9, 303.

60. W. Gao, J. Wang, ACS Nano, 2014, 8, 3170.

61. D. Vilela, J. Parmar, J. Zeng, Y. Zhao, S. Sánchez,Nano Letters, 2016, 16, 2860.

62. M. Safdar, S.U. Khan, J. Jänis, Adv Mat, 2018, 30,1703660.

63. J. Li, P. Angsantikul, W. Liu,B. Esteban-Fernández de Ávila, X. Chang, E.Sandraz, Y. Liang, S. Zhu, Y. Zhang, C. Chen, W. Gao, Adv Mat. 2018, 30, 1704800.

64. J. Li, P. Angsantikul, W. Liu, B. Esteban-Fernández De Ávila, S. Thamphiwatana, M. Xu, E. Sandraz, X. Wang, J. Delezuk, W. Gao, L. Zhang, J. Wang, Angew. Chem. Int. Ed. 2017, 129, 2188.

65. T.R. Kline, W.F. Paxton, T.E. Mallouk, A. Sen, Angew. Chem. Int. Ed. 2015 44, 744.

66. G. Zhao, S. Sanchez, O.G. Schmidt, M. Pumera. Chem Comm, 2012, 48, 10090.

67. Z. Li, L. Bai, C. Zhou, X. Yan,L. Mair, A. Zhang, L, Zhang, W. Wang, Particle & Particle Systems Characterization, 2017, 34, 1600277.

68. P. Fischer, A. Ghosh. Nanoscale, 2011, 3, 557.

69. R.S. Rikken, R.J. Nolte, J.C. Maan, J.C. van Hest, D.A. Wilson, P.C. Christianen. Soft Matter, 2014, 10, 1295.

70. E. Karshalev, C. Chen, G. Marolt, A. Martín, I. Campos, R. Castillo, T, Wu, J. Wang, Small, 2017, 13, 1700035.

71. T. Xu, F. Soto, W. Gao, V. Garcia-Gradilla, J. Li, X. Zhang, J. Wang, JACS, 2014, 136, 8552.

72. J.G.S. Moo, C.C. Mayorga-Martinez, H Wang, W.Z. Teo,B.H. Tan, T.D. Luong, S.T. Gonzalez-Avila, C.D. Ohl,. M. Pumera. Adv Funct Mat, 2018, 28, 1702618.

73. W. Wang, W. Duan, Z. Zhang, M. Sun, A. Sen, T.E. Mallouk, Chem. Comm. 2015, 51,1020.

74. T. Xu, F. Soto, W. Gao, R. Dong, V. Garcia-Gradilla, E. Magaña, X. Zhang, J. Wang, JACS, 2015, 137, 2163.

75. J. Li, T. Li,T. Xu, M. Kiristi, W. Liu, W. Wu, J. Wang, Nano letters, 2015, 15, 4814.

76. D. Zhou, Y. Gao, J. Yang, Y.C. Li, G. Shao, G. Zhang, T. Li, L. Li, Adv. Sci., 2018, 5, 1800122.

77. S. Tang, F. Zhang, J. Zhao, W. Talaat, F. Soto, E. Karshalev, C. Chen, Z. Hu, X. Lu, J. Li, Z. Lin, H. Dong, X. Zhang, A. Nourhani, J. Wang, Adv Funct Mat. 2019, 29, 1809003.

Chapter 2. Use of robotic platform for transport microscale transport

2.1 Introduction

Recent progress in the field of synthetic nanomotors has opened the door for new breakthrough applications. Yet, our ability to power, operate and propel nanomotors requires innovative approaches for overcoming the viscous forces that dominate at the low Reynolds numbers regime.[1-3] New propulsion strategies have thus been introduced, focusing on the conversion of localized chemical fuels or external forces into motion at the nanoscale.[4-10] Despite the attractive performance of chemically-powered nanomotors, they present several drawbacks towards biomedical applications. Specifically, these catalytic nanomotors rely on harvesting energy from chemical fuels that are commonly not biocompatible and their swimming behavior is commonly hard to modulate.[11-17] On the other hand, recently introduced acoustically-powered motors make use of acoustic fields sound waves that are relatively innocuous and easy to manipulate, offer unique advantages for enabling efficient and controllable motion (in different biological media), and allow for diverse surface functionalization.[18-26] Mallouk's group[18] and our team[23] described acoustically-propelled nanomotors based on an asymmetric gold nanowire containing a concave-end segment. These studies attributed the differential scattering of acoustic waves through the concave end of the nanowire as the mechanism responsible for acoustic propulsion. Nadal and Lauga proposed recently a new model, based on acoustic streaming to explain the acoustic propulsion of small bodies.[25] this theoretical model indicates that the propulsion is based on steady streaming stress produced over the asymmetric surface of a particle. While the majority of the work on acoustically propelled nanomotors has

relied on template-prepared nanowires (of around 2 μm length and 200 nm diameter),[21] different nanomotor designs may lead to improved performance and new advantages.

Herein, we present the efficient movement, attractive performance and new applications of nanoshells propelled by an acoustic field. These shell-shaped nanomotors offer a simple approach to realize asymmetric geometry while offering a high surface-area-to-volume ratio, efficient scaling of different size motors and higher towing capacity compared to common acoustically propelled nanowire motors. These highly efficient nanoshell motors are prepared by a simple and scalable sphere template fabrication method. A detailed study of the relevant parameters to acoustic propulsion, including the material density, size, and shape, indicated that the nanoshells exhibited different propulsion behavior than those predicted by recent theoretical and experimental models for near-sphere bodies[25] and metallic nanowires.[24] Such behavior suggests that a general model based only on the particle geometry may not be sufficient to predict the efficiency and directionality of acoustically-propelled micromotors. Finally, we demonstrate the ability of these nanoscale acoustic swimmers to perform complex tasks, including "on-the-move" capture and transport of multiple cargoes, and internalization and propulsion inside live MCF-7 cancer cells.

2.2 Experimental Methods

Reagents and Apparatus

All controlled-potential experiments were performed with a CHI 660D potentiostat (CH Instruments, Austin, TX). A Nikon Eclipse 80i microscope, coupled with a 10x and 20x objective, a Photometrics CoolSnap HQ2 CCD camera, and MetaMorph 7.6 software (Molecular Devices, Sunnyvale, CA) were used for capturing videos.

Experiment equipment

The sample reservoir was made of Kapton tape protective layer (5 mm diameter, and 240 μm height covered by an 18 mm x 18 mm x 0.15 mm glass slide for acoustic reflection). A piezoelectric transducer (Ferroperm PZ26 disk 10 mm diameter, 0.5 mm thickness), used for making the acoustic field, was placed below the bottom center of the steel plate. The continuous acoustic sine wave was applied via a piezoelectric transducer, through an Agilent 15 MHz arbitrary waveform generator while being connected to a home-made power amplifier. The applied continuous sine waveform had a frequency of 2.66 MHz and a voltage amplitude of 5 V, with both parameters essential for controlling the intensity of the ultrasonic wave.

Fabrication of nanomotors

The nanoshell motor deposition is illustrated in Figure 2.1A. First, polystyrene spheres were dropped cast on a glass slide. After drying, various layers of metals were deposited over them by e-beam evaporation, as reported previously in the literature.[17] First,

a titanium layer was used to ensure attachment of the subsequent layers to the polystyrene sphere. Next, a gold layer was added. After the metal deposition, the polystyrene spheres were dissolved in methylene chloride. To fabricate the Au/Ni/Au nanowires, a template electrodeposition synthesis protocol was performed using Garcia-Gradilla's [23] conditions.

Cell culture

Michigan Cancer Foundation-7 (MCF7-GFP) cells were obtained from the University of California, San Diego (UCSD), and Nanomaterials & Nanomedicine Laboratory. The cell lines were grown in Corning cellular DMEM media with 4.5 g/L glucose, L-glutamine, and sodium pyruvate purchased from Fisher Scientific; 10% HyClone Fetal Bovine Growth Serum (FBS) purchased from VWR International and 1% penicillin streptomycin purchased from Core Bio Services, and the cells were used immediately for the experiments. To prepare the cells suspension, first the cell culture media was removed, and then the cells were detached from the flask by treating them with 2 mL of Trypsin-EDTA (0.25%), obtained from Core Bio Services, for 2 minutes. The trypsin was then inactivated using the supplemented media, centrifuged for 5 min at 0.7 RCF, and suspended to the correct concentration in media using a hemocytometer in order to achieve a concentration of ~5000 cells per well. The cells were then treated with the acoustically propelled nanoshells and incubated in a 96 well plate at 37°C overnight. After incubation, the media was removed and replaced with phosphate buffered saline (PBS), for 5 minutes in order to wash away any motors that were not internalized in the cell. This PBS was removed and a second washing step with additional PBS was performed. After removing the second volume of PBS, each well was treated with trypsin-EDTA (0.25%)

and then mixed with the modified media to inactivate the trypsin. The resuspended cells were then treated with the acoustic field again and imaged.

2.3 Experimental Results

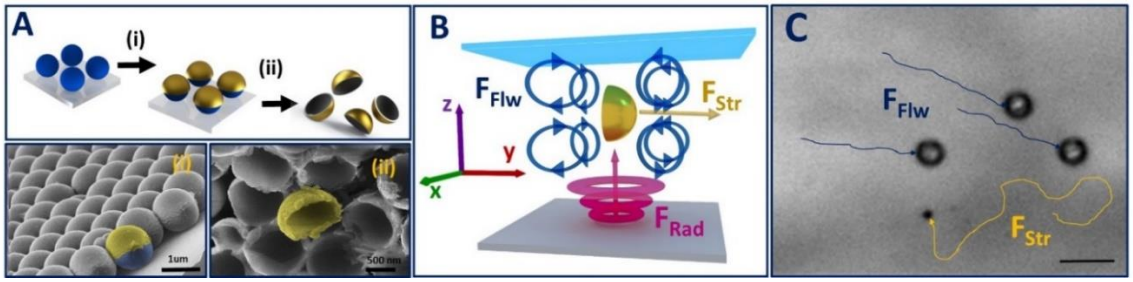

Figure 2.1 A) Schematic of the nanoshell fabrication method and operation. First, a thin metal film is deposited over a (i) template particle. Next, (ii) the template is dissolved to produce the desired nanoshell structure. SEM images illustrate the (i) template deposition and the (ii) shell after removing the template. B) Acoustic propulsion mechanism. Upon application of an ambient acoustic field, composed of ambient fluid flow (FFlw) and acoustic radiation (FRad) forces, particles migrate to a levitation plane in the middle of the reservoir. The sum of steady streaming stress produced over the surface of the nanoshell does not cancel out due to its asymmetric shape, producing the driving force for nanoshell propulsion (FStr). C) Simultaneous motion of nanoshells propelled by FStr (Yellow track line) and tracer particles dragged by FFlw (Blue track line) using 5 V and 2.66 MHz. Scale bar, 20 μm.

The fabrication of the nanoshell motors is illustrated in Figure 2.1A. First, polystyrene beads were dispersed over a glass slide. These beads served as the template over which a thin metallic bilayer (consisted of a titanium adhesion layer and gold layer as the main body) was deposited to cover half the surface of the beads in order to realize the final nanomotor's hollow shell structure. To release the nanoshells, the polystyrene beads were dissolved in methylene chloride. Further collection and washing were performed before, finally, re-suspending the remaining nanoshells in deionized water. The final

structure of the nanoshell consists of a thin hemispherical cup-shape featuring a hollow concave interior and convex exterior, such defined shape asymmetry is ideal for generating the pressure gradient needed for motion.[23] Shell-shaped nanomotors have been designed earlier for chemical propulsion,[27-29] but have not been described for fuel-free nanomotors, in general, or for acoustic nanomotors.

The acoustic propulsion of rigid nanoparticles relies on the local conversion of energy from an ambient acoustic field into motion.[18,25] Three distinct acoustic related phenomena commonly result from the application of an acoustic field. The first is an 'ambient fluid flow' (FFlw) produced by non-linearity in the incident acoustic field.[30] This ambient streaming flow exists regardless of the presence of nanoparticles. The second is the 'acoustic radiation force' (FRad) arising from rectification between the oscillatory stress exerted on the particle by the ambient acoustic field and the oscillatory and out-of-phase particle motion.[31] This force is responsible for the migration of particles towards a levitation plane and acoustic nodes. The third one is an 'acoustic streaming' (FStr) force that produces the propulsion of asymmetric particles based on the disturbance fields induced by particle motion.[25,26]

Acoustic self-propulsion allows each nanoshell to move independently rather than being dragged in aggregate by the ambient fluid flow or acoustic radiation forces; such effect can be clearly visualized in Figure 2.1C. Here, three tracer particle beads (blue track line) are dragged by the ambient fluid flow, while the acoustically propelled nanoshell (yellow track line) moves even against the flow, indicating that its directionality and propulsion are not driven by the direction of the fluid flow. The propulsion of the

nanoshells can be controlled by changing the applied acoustic field. When the acoustic field is turned off, the nanoshell motion is halted rapidly within 0.1 s, displaying a negligible net displacement (reflecting the Brownian motion). Upon reapplying the acoustic field, the nanoshells resume their movement quickly within 0.1 s. Such rapid 'stop/go' operation can be repeated multiple cycles, as the process relies only on the applied acoustic field.[23] It should be noted that the levitation plane disappears when the acoustic field is turned off, causing the particles to settle at the bottom of the reservoir. The critical parameters for generating the acoustic propulsion of nanoshells (material density, size and shape asymmetry) and their use in complex tasks will be discussed in the following sections.

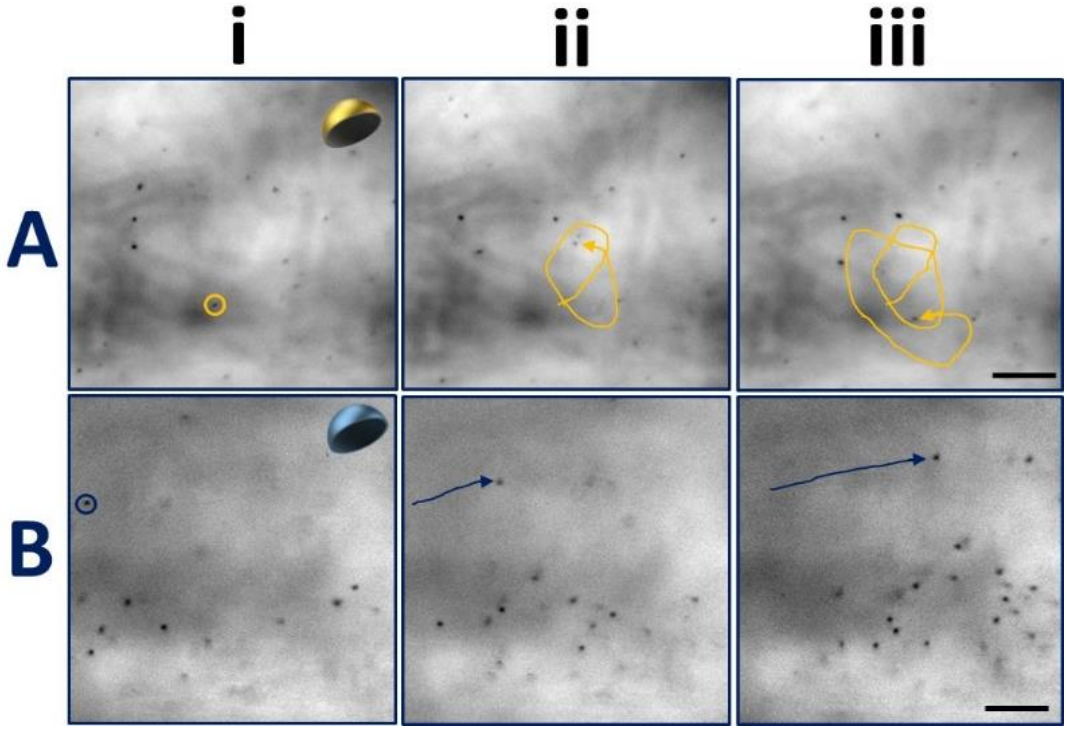

Figure 2.2. Effect of the motor density of propulsion: A) high-density (Au) nanoshells presents autonomous motion, while B) low-density (SiO_2) nanoshells are dragged by the ambient fluid flow, despite the shape asymmetry of both nanoshells. Times and acoustic parameters: i= start, ii= 0.5s, iii= 1s, 5 V, 2.66 MHz; scale bar, 10 µm.

First, we tested the effect of density on the propulsion by comparing the trajectories of high-density metallic nanoshells to those of low-density nanoshells (with a density similar to that of the fluid) and similar size (1 μm in diameter). The low-density nanoshells were fabricated following a similar protocol but covering half the surface with a silicon dioxide layer instead of the metallic film previously used. The high-density nanoshells (Figure 2.2A) presented autonomous motion in independent trajectories, whereas the low-density nanoshells (Figure 2.2B) were dragged by the ambient fluid flow in a vortex-like trajectory despite their shape asymmetry.

This different motion behavior stems from the differences in the density ratios ($\rho_{water}/\rho_{particle}$) between each particle ($\rho_{particle}$) and the density of water (ρ_{water} = 0.997 g/cm^3). Specifically, Nadal and Lauga suggested that the parameter (1-β), where $\beta = \rho_{water}/\rho_{particle}$ is proportional to the propulsion speed.[21,26] This dependence could explain why the relative velocity and acoustic streaming force exerted on high-density particles (gold with ρ = 20.5 g/cm^3 and β = 0.049) is significantly greater than on low-density particles (silicon dioxide with ρ = 2.65 g/cm^3 and β = 0.376). The experimental results show that this prediction is qualitatively correct, since the measured propulsion speeds decrease with (1-β). On the other hand, the prediction is quantitatively incorrect, since the model predicts that a 40% difference in 1-β should correspond to a 40% difference in the propulsion speed, a behavior not observed experimentally. It should be noted that the velocity of the low density nanoshells is not strictly 0 μm/s, but the propulsion force generated might not be strong enough to overcome the fluid flow.

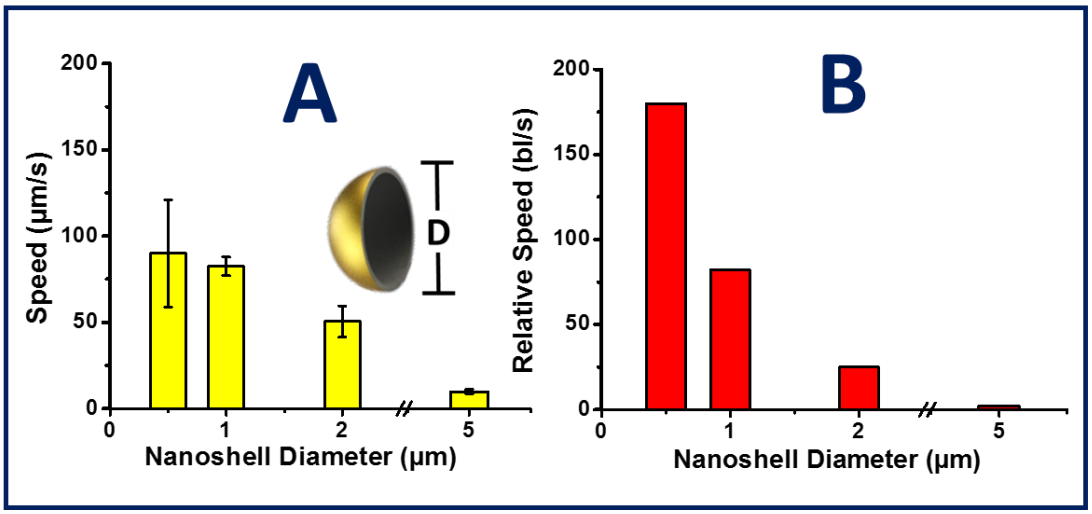

Figure 2.3. A) Effect of the motor size on the nanoshell propulsion. The absolute speed (measured in μm/s) increases 10 fold upon reducing the nanoshell size from 5 μm to 0.5 μm. B) Effect of the nanoshell size upon the relative speed (measured in body lengths/s). Measurements were carried out using an acoustic field with 5 V and 2.66 MHz.

Next, we examined the effect of nanoshell size on the propulsion by comparing the speed of nanoshells of varying diameters. The simple fabrication method allows convenient preparation of a wide range of nanoshell sizes by simply changing the size of the bead template. Figure 2.3A demonstrates that the propulsion speed increases upon decreasing the diameter of the nanoshell. Using an amplitude of 5 V and frequency of 2.66 MHz for generating the ambient acoustic field, nanoshells of 5.0, 2.0, 1.0 and 0.5 μm display speeds of 9.9 ± 1.2, 50.5 ± 9.1, 82.4± 5.4 and 89.9± 31.1 μm/s, respectively. A nearly 10-fold change in the absolute speed is thus observed upon reducing the nanoshell diameter from 5 μm to 0.5 μm. Furthermore, the same experiment yields a 90 fold increase in the relative speed (from 1.98 to 179.96 body lengths/s) upon decreasing the size (Figure 2.3B). This

result cannot be explained by the near-sphere model of Nadal and Lauga,[26] which predicts that the streaming-induced speeds increase linearly with the radius of a near-sphere particle.

There are two possible reasons for this discrepancy. First, the strongly non-spherical shape of our nanoshell suggests that the physics of its propulsion is not adequately described by the near-sphere model of Nadal and Lauga. The second reason is that Nadal and Lauga assume that the viscous parameter λ is significantly smaller than 1 with $\lambda = R(\omega/\nu)^{1/2}$, with R the particle radius, ω the acoustic frequency and ν the kinematic fluid viscosity.[31] In our experiments, R ranges from 250 to 2500 nm, while ω = 2.66 MHz and $\nu \approx$ 10-6 m^2/s, and hence λ varies between 0.41 and 4.1. The magnitude of the linear inertia - relative to viscous forces - is measured by $\lambda 2$; when $\lambda \sim 1$, the inertia is of similar magnitude as the viscous stress. The model of Nadal and Lauga does not cover streaming propulsion in this regime, and thus does not accurately explain the size-to-speed relationship observed in our experiments. Further research on a comprehensive theory explaining propulsion in this regime is thus required.

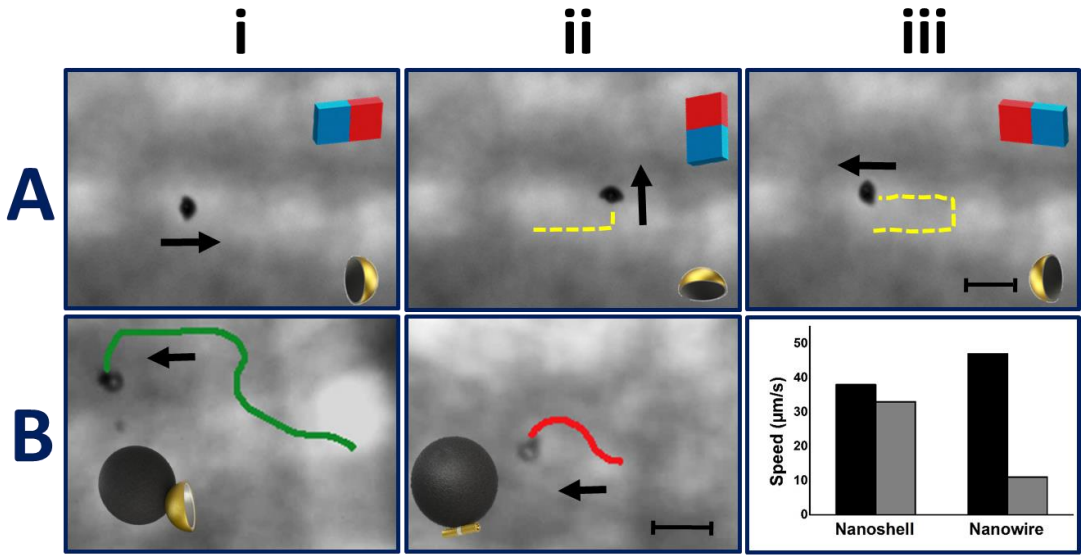

Figure 2.4. Magnetic guidance of the nanoshells. A) Nanoshell movement in the convex exterior direction. First, the nanoshell is moving to the right, next the external magnetic field rotates the nanoshell 90 degrees. Finally, the nanoshell moves to the left, opposite to the initial direction. In all of these three cases, the motion of the nanoshell always follows the direction of the convex side of the shell. B) Comparison of cargo-towing abilities of nanoshell (i) and nanowire (ii) motors. Graph (iii) illustrates the respective velocities of the nanoshell and nanowire motors before (black) and after (grey) capturing the magnetic beads. These images were taken from actual microscope footage, illustrating the towing capabilities of each motor during the same timeframe (4 sec). (Scale bars A and B: 10 μm).

The influence of the shape asymmetry upon the propulsion and magnetic guidance of the nanoshell was also tested. In order to identify the specific direction in which the nanoshells move, an intermediate Ni layer was added in between the internal titanium and external gold layers. This Ni segment allowed precise control of the nanoshell orientation via the application of an external magnetic field (produced by a permanent magnet). As a result, through the combination of this external magnetic field and acoustic-propulsion of the motors, we were able to move and orient the nanoshell in any arbitrary direction.

Furthermore, the experimental results presented in Figure 2.4A(i-iii) indicate that the nanoshell motor (5 μm diameter, oriented magnetically to stand vertically on the levitational plane) moves towards the direction of the convex exterior. Specifically, the nanoshell first distinctly moves to the right and then it rotates 90 degrees via manipulation of the external magnetic field. Finally, after redirecting the magnetic field once more, the nanoshell moves to the left. In all cases, the motion points in the direction of the convex part of the nanoshell. We assume that most of the nanoshells will come in and out of the parallel position in regards of the levitation plane due to the multiple forces acting on them (e.g., particle vibration, fluid flow, acoustic radiation forces); this could explain the chaotic motion patterns of the nanoshells.

The motion directionality presented by the nanoshells differs from recent experiments by Ahmed et al. using bimetallic nanowires of different densities, which suggested two main rules to predict the directionality of acoustically-propelled nanomotors. First, the motion will always follow the direction of the lower-density material; second, if the nanomotor materials are of similar density, then the directionality will be in the direction of the concave asymmetry.[24] The discrepancy between our results and those of Ahmed et al. indicates that these rules are not universal for all particles. Even though a complete theory describing acoustic-powered motion has not been presented yet, we can postulate the reasons as to why our nanoshell experiments are not consistent with such predictions. To do this, we must first consider the prediction that the directionality of the nanoshells will always be towards the lower density material. The non-uniform particle density in the experiments of Ahmed *et al*[24] exerts a significant torque on their slender rods

which affects the particle orientation. Using our uniformly density-layered nanoshells, this torque is likely to be small or absent, greatly hindering its effect on the nanoshells' directionality. Regarding the disagreement with Ahmed *et al*[24] second prediction regarding the propulsion direction, previous models may not be useful for predicting directionality based solely on the particle geometry, as the acoustic propulsion may depend on multiple non-trivial unknown parameters.

Finally, we explore several possible directions in which acoustic nanoshell motors could be applied. First, we illustrate "on-the-move" capture and transport of magnetic cargoes by the acoustically-propelled nanoshells (see Figure 2.4B). For this, we compared the cargo towing capabilities of 2 μm nanoshells to those of acoustically-powered gold nanowires (2 μm long and 200 nm in diameter), with both motors containing a Ni magnetic segment to allow for magnetic guidance. Interestingly, when comparing their cargo towing speed in transporting a 3.3 μm iron oxide magnetic bead, the nanoshell initially presented slower pre-capture speed than the nanowire (38 and 47 μm/s, respectively); however, the nanoshells then exhibited a post-capture towing speed three times higher than that of the wires (33 and 11 μm/s, respectably). This behavior can be explained by considering that a new body shape is formed when the nanowire captures the bead by magnetic attraction. This leads to a significant change in the relative asymmetry, losing the streamlined shape of a rod. In contrast, when the nanoshell captures the magnetic bead, the relative change in relative asymmetry is not as pronounced, allowing the nanoshell to retain its speed.

The effect of the relative shape asymmetry on the propulsion can be further illustrated when comparing the propulsion of gold nanoshells and gold beads with a rough

surface. Although these rough gold beads have high density and some degree of asymmetry, only few of them display autonomous motion, suggesting that the relative shape asymmetry is essential for propulsion. Multiple cargoes can also be captured and transported, where a magnetic nanoshell of 5 μm in diameter is guided to capture and transport multiple 3.3 μm magnetic beads.

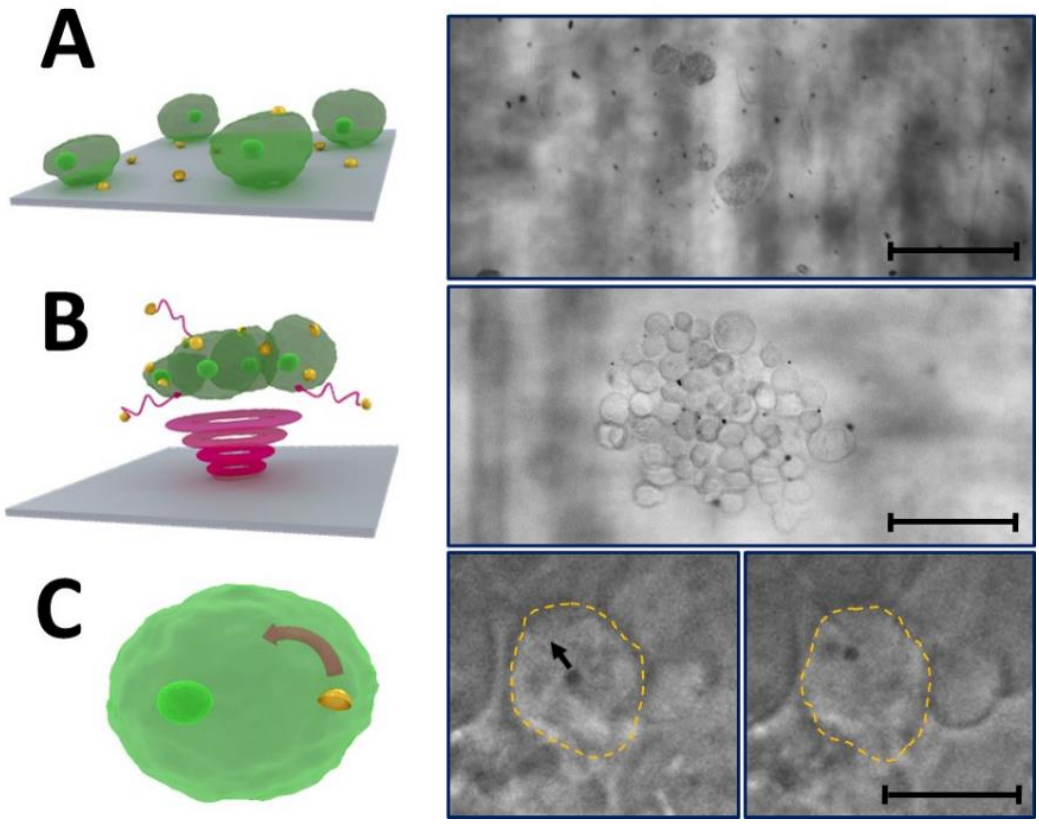

Figure 2.5. Schematic and micrographs illustrating the nanoshell internalization and propulsion inside a MCF-7 GFP cancer cell. A) A mixture of nanoshells and cancer cells is placed initially in a reservoir; B) upon application of the acoustic field the nanoshells and cells migrate into a levitation plane and concentrate in that plane, where the nanoshells propulsion increases their interaction with the surrounding cells. C) After incubation for 24 hours the internalized nanoshells were activated by applying the acoustic field, exhibiting autonomous motion. scale bars, A and B: 50 μm, C: 10 μm.

The nanoshell ability to internalize and move inside live MCF-7 cancer cells has also been demonstrated, as illustrated in Figure 2.5. The experiments consisted of a mixture of nanoshells and MCF-7 cancer cells exposed to the acoustic field. Specifically, the acoustic forces drive the migration of MCF-7 cancer cells towards the levitation plane in the middle of the reservoir allowing for their pre-concentration. Simultaneously, the propulsion of the nanoshells increases their interactions with the cells. Next, the MCF-7 cells and nanoshells were incubated for 24 hours. Following treatment and suspension of the cells (see details in Experimental section), the internalized nanoshells were activated upon exposure to the acoustic field, displaying directional motion inside the cell. The mechanism of such intracellular nanoshell propulsion is similar to the previously presented model in this article, as acoustic fields have been demonstrated to penetrate the cell membrane.[32,33] The autonomous movement of the acoustic motors inside live cells and the viability of the cells after internalization and acoustic exposure[34-36] showcases the applicability of these nanostructures as a source of mechanical force within the cell, towards diverse intracellular processes, such as modulation of gene expression.

2.4 Conclusions

We have developed a new design of acoustic nanoswimmers, based on a nanoshell geometry, fabricated by a sphere template process. Multiple parameters of these swimmers, including the density, size and shape, were examined in order to identify the key factors responsible for the conversion of the acoustic energy into motion. The motion of the new acoustically-propelled nanoshells can be precisely controlled and guided, as was illustrated using “on-off” operation and magnetic navigation, respectively. The inverse relationship

between particle-size and speed is opposite to that predicted by the near-sphere and strongly-viscous models. Additionally, the experimental results indicate that the material density has a greater effect on the motion than the particle asymmetry, but that the geometry still plays a fundamental role in the directionality of the nanoshell. This behavior suggests that further research is needed to understand the physics of nanomotor propulsion in the experimentally-relevant regimes of strong shape asymmetry and where linear inertia and viscous forces are equally important and to predict the behavior of acoustic nanomotors with different geometries. Finally, the practical application of the nanoshell was demonstrated by performing complex tasks, such as the capture and transport of multiple cargoes and the internalization and propulsion of the nanoshells inside live MCF-7 cancer cells. The attractive performance and new capabilities of these acoustically-propelled nanoshells pave the way for creating advanced fuel-free nanomachines capable of performing diverse biomedical tasks and applications.

Chapter 2 is based, in part, on the material as it appears Nanoscale, 2016, Fernando Soto, Gregory L Wagner, Victor Garcia-Gradilla, Kyle T Gillespie, Deepak R Lakshmipathy, Emil Karshalev, Chava Angell, Yi Chen, Joseph Wang. The dissertation author was the primary investigator and author of this paper.

2.5 References

1. R. P. Feynman, Eng. Sci., 1960, 23, 22– 36.

2. E. M. Purcell, Am. J. Phys., 1977, 45, 3-11.

3. W. R. Sanhai, J. H. Sakamoto, R. Canady, M. Ferrari, Nat. Nanotechnol., 2008, 3, 242–244.

4. J. Wang, Nanomachines: Fundamentals and Applications, Wiley-VCH, Weinheim, Germany, 2013, ISBN 978-3-527-33120-8.

5. A. A. Solovev, S. Sanchez, M. Pumera, Y. F. Mei, O. G. Schmidt, Adv. Funct. Mater., 2010, 20, 2430–2435.

6. W. Wang, W. Duan, S. Ahmed, T. E. Mallouk, A. Sen, Nano Today, 2013, 8, 531– 554.

7. H. Wang, M. Pumera, Chem. Rev., 2015, 115, 8704– 8735.

8. S. Tottori, L. Zhang, F. Qiu, K. K. Krawczyk, A. Franco-Obregón, B. J. Nelson, Adv. Mater., 2012, 24, 811–816.

9. K. Kim, J, Guo, X. Xu, D.L. Fan, Small, 2015, 11, 4037– 4057.

10. W. Gao, J. Wang, ACS Nano, 2012, 6, 4745-5751.

11. V. V. Singh, F. Soto, K. Kaufmann, J. Wang, Angew. Chem., Int. Ed., 2015, 54, 6896–6899

12. L. Soler, S. Sánchez, Nanoscale, 2014, 6, 7175-7182.

13. S. K. Srivastava, M. Guix, O. G. Schmidt, Nano Lett., 2016, 16, 817–82.

14. L. K. Abdelmohsen, M. Nijemeisland, G. M. Pawar, G. J. A. Janssen, R. J. Nolte, J. C. van Hest, D.A. Wilson, ACS Nano, 2016, 10, 2652–2660.

15. J. Li, I. Rozen, J. Wang, ACS Nano 2016, 10, 5619–5634.

16. T. C. Lee, M. Alarcón-Correa, C. Miksch, K. Hahn, J. G. Gibbs, P. Fischer, Nano letters, 2014, 14, 2407-2412.

17. W. Gao, X. Feng, A. Pei, Y. Gu, J. Li, J. Wang, Nanoscale, 2013, 5, 4696-4700.

18. W. Wang, L. A. Castro, M. Hoyos, T. E. Mallouk, ACS Nano, 2012, 6, 6122−6132.

19. J. J. Kwan, R. Myers, C. M. Coviello, S. M. Graham, A. R. Shah, A. E. Stride, R. C. Carlisle, C. C. Coussios, Small, 2015, 11, 5305–5314.

20. Z. Wu, T. Li, W. Gao, T, Xu, B. Jurado-Sánchez, J, Li, W. Gao, Q. He, L. Zhang, J. Wang, Adv. Funct. Mater., 2015, 25, 3881.

21. K. J. Rao, F. Li, L. Meng, H. Zheng, F. Cai, W. Wang, Small, 2015, 11, 2836−2846.

22. F. Soto, A. Martin, S. Ibsen, M. Vaidyanathan, V. Garcia-Gradilla, Y. Levin, A. Escarpa, S. C. Esener, J. Wang, ACS Nano, 2016, 10, 1522–1528.

23. V. Garcia-Gradilla, J. Orozco, S. Sattayasamitsathit, F. Soto, F, Kuralay, A. Pourazary, A. Katzenberg, W. Gao, Y. Shen, J. Wang, ACS Nano, 2013, 7, 9232−9240.

24. S. Ahmed, W. Wang, L. Bai, D. T. Gentekos, M. Hoyos, T.E. Mallouk, ACS Nano, 2016, 10, 4763-4769.

25. F. Nadal, E. Lauga, J. Acoust. Soc. Am., 2016, 139, 1081-1092.

26. F. Nadal, E. Lauga, Phys. Fluids, 2014, 26, 082001.

27. G. Zhao, M. Pumera, Nanoscale, 2014. 6, 11177-11180.

28. W. Huang, M. Manjare Y. Zhao, J. Phys. Chem. C, 2013, 117, 21590-21596.

29. M. Safdar, T. Itkonen J. Jänis, RSC Advances, 2015, 5, 13171-13174.

30. J. Lighthill, J. Sound Vib., 1978, 61, 391–418.

31. A. Doinikov, Proc. R. Soc. London Ser. A, 1994, 447, 447.

32. Z. Fan, Y. Sun, D. Chen, D. Tay, W. Chen, C. X. Deng J. Fu, Scientific reports, 2013, 3.

33. M. Afadzi, S. Strand, E. Nilssen, S.-E. Måsøy, T. Johansen, R. Hansen, B. Angelsen C. de, L. Davies, IEEE Trans. Ultrason. Ferroelectr. Freq. Control., 2013, 60, 21–33.

34. W. Wang, S. Li, L. Mair, S. Ahmed, T. J. Huang T. E. Mallouk, Angew. Chem., Int. Ed., 2014, 53, 3201-3204.

35. B. Esteban-Fernández de Ávila, A. Martín, F. Soto, M. A. Lopez-Ramirez, S. Campuzano, G. M. Vásquez-Machado, W. Gao, L. Zhang J. Wang, ACS Nano, 2015, 9, 6756-6764.

36. B. Esteban-Fernández de Ávila, C. Angell, F. Soto, M, A. Lopez Ramirez, D. F. Baez, S, Xie, J, Wang, J. Y. Chen, ACS Nano, 2016, 10, 4997-5005.

Chapter 3 Use of robots platforms for surgery

3.1 Acoustic microcannons: Toward advanced microballistics

3.1.1 Introduction

Magic bullets' that would drive drugs deep into diseased tissues have been a dream of biomedical researchers for over a decade.[1,2] Such 'magic bullet' vision has inspired and encouraged scientists to create efficient delivery devices towards the successful treatment of human diseases. Designing the right tool for efficient tissue penetration at small scales is essential for diverse applications in drug delivery and microsurgery applications. Novel micro/nanoscale ballistic tools could pave the way of deep tissue penetration on small scales, providing distinct advantages, due to their size and ability to reach places where catheters cannot. Powerful machinery, including ballistics, exists on the macroscopic scale to penetrate and cut through tissues. However, these large-scale ballistic tools do not have analogous micro/nanoscale counterparts, hindering the ability to operate at this small scale and resulting in very limited tissue penetration.

Traditional technology cannot be simply scaled down due to the dominating viscosity forces (over inertia forces) at lower scales that affect both the movement and directionality.[3-6] Accordingly, small scale machinery tools need to be powered and actuated by fundamentally different approaches than macroscopic devices. New nanomachine strategies have been developed recently in this direction.[7-13] Such tiny machines are capable of performing diverse applications,[14-17] including some initial reports of microsurgery[18,19] and cell internalization.[20-21] However, obtaining a stable, controlled, powerful, and directed means of penetrating tissue and delivering payloads at these small scales remains a major

technological challenge. Although bullet-shaped microstructure materials have been designed[22] and metallic microbullets are reported as therapeutic tools,[23-24] they do not offer penetration capabilities or motion, but rather they are only incubated with the target. Indeed, there are no earlier reports regarding the controlled firing of nanobullets from a microstructure.

To address this challenge and fill this technological gap, we demonstrate here the use of acoustically-triggered microcannons (Mc), capable of versatile loading and effective firing of nanobullets (nB), as novel tools towards advancing microscale tissue penetration of therapeutic payloads. The electrochemically-synthesized hollow microcannons have been fully loaded with a gel matrix containing the nB and a perfluorocarbon (PFC) emulsion (Figure 3.1.1A). The ultrasound (US) triggered vaporization of the PFC emulsion,[25,26] confined inside the Mc, results in the rapid ejection of the nB, reaching remarkable speeds (on the scale of meters per second), analogous to the firing of a bullet through a barrel of a gun (Figure 3.1.1B). The new microballistic concept was theoretically modeled and experimentally demonstrated. Deep penetration capabilities were demonstrated by firing the nB from an array of static Mc into a phantom gel target.

US-triggered microbubble vaporization is an extremely attractive candidate for externally triggering the actuation of such micro/nanoscale ballistic tools, as it is biocompatible[27,28] and has been previously used to enhance the permeation and delivery of therapeutics into blood vessels and tissue.[29-39] However, there are no reports of acoustic microcannons capable of firing nanobullets. We expect that the new US-based ballistic

approach could lead to efficient delivery devices capable of delivering a wide range of payloads deep into an identified target.

3.1.2 Experimental Methods

Perfluorononane emulsion preparation

Perfluorononane (PFN) nanoemulsions purchased in Sigma Aldrich (St Louis) were prepared in phosphate buffer saline (PBS). A volume ratio of 3:1:1 of PBS : Anionic fluorosurfactant : PFN was prepared through probe-type sonication. The tube containing PBS was immediately placed in a heating block at 90 ºC for 5 minutes and 200 µL of Zonyl FSE (Sigma Aldrich, St Louis) anionic fluorosurfactant was added. The solution was vortexed until homogenized. A 200 µL aliquot of PFN (from Sigma Aldrich, St Louis) was added to the PBS-Zonyl FSE mixture. The probe of the sonicator was lowered in the tube about 8 mm from the bottom. While still in the ice bath, the sonicator was operated with a LabVIEW program interfaced with the sonicator via (a foot pedal input and a reed relay board. The program delivered three 0.5 second bursts and was repeated 60 times. The short bursts prevented the solution from stirring violently and producing foam; a 2 sec delay between each set of 3 bursts served to prevent overheating. This process resulted in a 20 % vol. PFN emulsion which was stable and turbid in appearance. Emulsion sizes and zeta potentials were measured by dynamic light scattering with a Zetasizer Nano-ZS (Malvern Instruments, Worcestershire, UK). The 20 % vol. PFN emulsion was diluted to 1% vol. by a PBS pH 7.4 solution before incubating with the Mcs.

Microcannon synthesis

The Mcs were prepared by electrochemical template synthesis of graphene and gold layers.[36] The outer layer of electrochemically reduced graphene oxide (erGO) was prepared by the electrochemical reduction of graphene oxide (GO, graphene supermarket, New York, USA) into 5 μm diameter conical pores of a polycarbonate membrane (Catalog No. 7060–2513; Whatman, Maidstone, UK). A thin gold film was first sputtered on the branched side of the membrane to serve as a working electrode. The membrane was assembled in a Teflon plating cell with aluminum foil serving as an electrical contact for the subsequent electrodeposition. Graphene oxide (GO, 0.1 mg mL–1) was first dispersed in a solution containing 0.1 M H_2SO_4 and 0.5 M Na_2SO_4 purchased in Sigma Aldrich (St. Louis) by ultrasonication for 15 min. The resultant homogeneously dispersed brown GO can be stable for several weeks because of the high presence of oxygen functionalities. The simultaneous electrochemical reduction and deposition of GO was carried out using cyclic voltammetry (CV, over +0.3 to –1.5 V vs. Ag/AgCl (3 M KCl) from (CH Instrument, Austin, USA), at 50 mV s^{-1}, for five cycles; n = 5), using a Pt wire as counter electrode. Subsequently, a gold layer was plated inside the erGO layer acting as a scaffold or supporting layer for the graphene not to collapse. The gold layer was plated at –0.9 V using a charge of -1.5 C from a commercial gold plating solution (Orotemp 24 RTU RACK; Technic Inc.). The sputtered gold layer was gently removed by hand polishing with 3–4 μm alumina slurry.

Gelatin purchased in a local supermarket was prepared at 40 mg mL-1 by dissolving in water heating at 40 ºC and later cooling it to room temperature allowing it to solidify. 100 μL PFN (dilution 1:100 from the synthesized), 50 μL silica particles (1 μm

Polysciences,) and 50 μL gelatin were infiltrated in the resulted membrane and allowed to cool and dry until complete dryness and solidification of the gelatin in the pores. The surplus gelatin outside of the pores was washed thoroughly with a swab. The membrane was then dissolved in methylene chloride for 5 min to completely release the Mcs. The Mcs were collected by centrifugation at 7000 rpm for 3 min and repeatedly washed with ethanol and three times with ultrapure water (18.2 Ω cm), with a 3 min centrifugation following each wash. All Mcs were used after synthesis at room temperature. For the tailored loading of nB inside the Mc, the density of the embedded silica Nb was controlled by changing the concentration from the original commercial Silica solution (MicroSil Microspheres), obtaining 'high loading' at 1:1 ratio, 'medium loading' at 1:100 dilution ratio and 'low loading' at 1:1000 dilution ratio.

For static Mc experiments, the same Mc synthesis and cargo loading methodology was used, but without dissolving the polycarbonate membrane template, allowing to act as an array of statics Mc. Note that for the fluorescence experiments with static Mc, the Mc were loaded by infiltrating with a solution of 50 μL of Fluorospheres microsphere solution (f8803 invitrogen, USA; 0.5 mg/mL), instead of the silica particles. These fluorescence experiments were performed inside a phantom tissue gel made of 0.5% weight of Agarose (Sigma-Aldrich, USA).

Acoustic-microcannon firing of nanobullets.

Mc propulsion was initiated by exposure to a focused ultrasound pulse using a custom-designed ultrasound and microscope system.44 A PCI-5412 arbitrary waveform (National Instruments, Austin, TX) was used to create a single 10 ms long US pulse at 2.25 MHz. A 300 W amplifier (Vox Technologies, Richardson, TX) was used to create a peak negative pressure of 1.9 MPa at the focal zone with a Panametrics V305-SU transducer (Olympus NDT Inc., Waltham, MA). A custom-designed LabVIEW 8.2 program was utilized to initiate the US pulses. The transducer was submerged in a water tank while a Petri dish containing the sample was positioned at the water surface placing the sample in both the focal zone of the optics and the US transducer as previously described by Ibsen *et. al.*[44]

In order to capture the Mc propulsion, videos were acquired at 10,000 or 18,000 frames per second (fps) using a FASTCAM 1024 PCI high-speed camera (Photron, San Diego, CA) and a 20X objective. Frame rates of 45,000 and 109,500 fps were used for capturing the motion of bubbles resulting from emulsion vaporization. For static Mc experiments, the template membrane with the embedded motors was placed on a Petri dish. Experiments showing the ejection of silica nB from the Mc were performed in water in a Petri dish. The experiments showing the ejection of fluorescent Fs were performed with static Mc anchored in the flexible template membrane strips embedded at the bottom of a 0.5 % agarose tissue phantom that was placed inside. After applying the ultrasound pulse, the tissue phantom was sectioned and imaged in cross section using a Nikon Eclipse 80i upright microscope with a fluorescence B2-A FAM filter to determine the distance over which the fluorescent Fs nB had penetrated into the phantom. It should be noted that there

is a small agar filled gap between the template membrane and the petri dish, generating a green fluorescent line at the bottom of the membrane after the US pulse The SEM images were taken with a Phillips XL30 ESEM.

3.1.3 Experimental Results

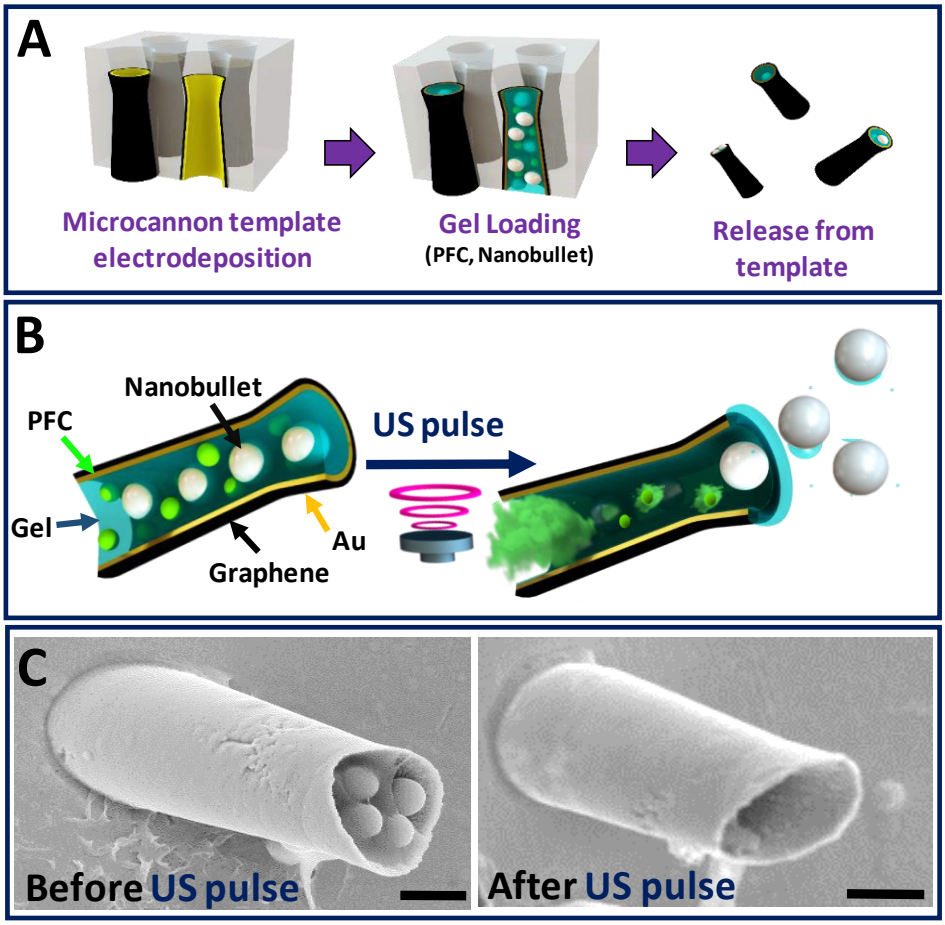

Figure 3.1.1. Ultrasound triggered nB firing based on vaporization of PFC droplets as a propulsion system. (A) Microcannon (Mc) fabrication by template electrodeposition, loading of cargoes by infiltrating them inside a gel matrix into the interior of the hollow Mcs and releasing the Mc from the template. (B) Mc composition (left) and schematic illustrating the firing of nanobullets (nB) from Mc by the spontaneous PFC vaporization upon application of US pulse (right). (C) SEM images (different Mc from the same batch) showing the nB-loaded Mc before (left) and after (right) the US-triggered firing. Scale bar, 20 μm.

A schematic of the synthesis of acoustically-triggered Mcs is illustrated in Figure 3.1.1A. First, the hollowed cone structure of the Mc was fabricated using template electrodeposition of electrochemically reduced graphene oxide (erGO) and gold (Au) on the walls of micropores in a polycarbonate membrane; see experimental section and further details in Martin et al.[40] Afterward, a liquid gel matrix (at 40 ºC), containing 1 μm silica nBs and PFC emulsions, was infiltrated by gravitational and capillarity forces into the hollow Mcs anchored in the template membrane.[41,42] After cooling down to room temperature, the particles were entrapped in the solidified gel matrix which served as a stabilizer and scaffold to protect and retain the loaded nB and PFC emulsion within the Mc interior.

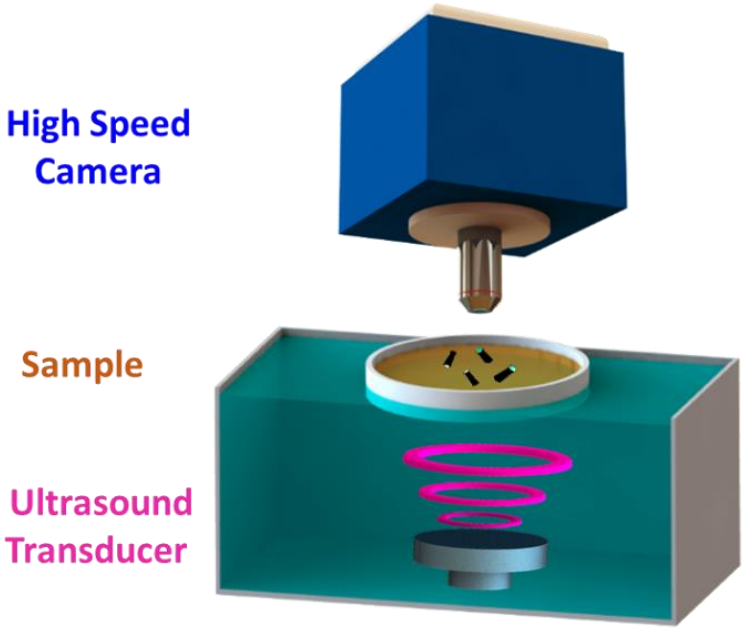

Figure 3.1.2. Schematic of the Ultrasound Set up: The operation consists of a piezoelectric transducer submerged in water, a petri dish which contains the sample, and the firing of the microcannons is recorded by a high-speed camera on top.

A schematic of the Mc components and operation is shown in Figure 3.1.1B. Upon application of a focused ultrasound pulse by a piezoelectric transducer as shown in Figure 3.1.2), the nBs are ejected rapidly from the Mc. The mechanism responsible for the propulsion thrust of the nB relies on the momentum associated with the ultrasound-induced spontaneous vaporization of the PFC emulsion droplet into a rapidly expanding microbubble. The subsequent expulsion of these microbubbles from one opening of the Mc structure leads to the ejection of nBs, thereby displacing the Mc. The ejection of the nB from the Mc structure is further supported by Figure 3.1.1C and Figure 3.1.3. which shows SEM micrographs of MC before and after the US pulse. While the nBs are initially packed in the gel within the Mc, the cannon is nearly empty after the ultrasound pulse, reflecting the PFC vaporization and the ejection of the nBs.

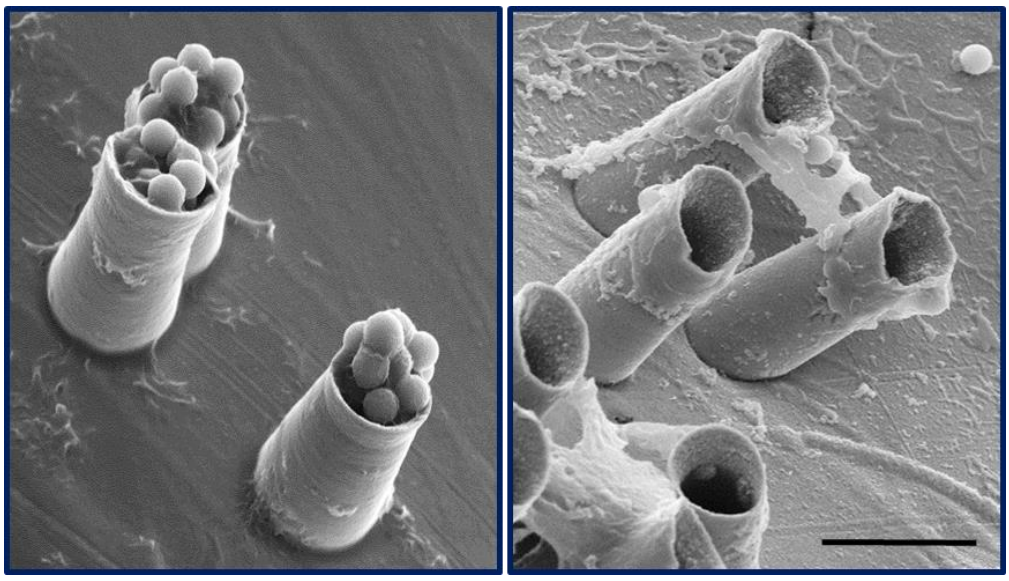

Figure 3.1.3. SEM characterization showing multiple nanobullet-loaded Microcannons before (left) and after (right) the Ultrasound-triggered firing (scale bar, 5 μm).

Figure 3.1.4A illustrate a vaporized PFC gas bubble which is clearly visible after the US pulse. The rapid emulsion expansion during the vaporization process provides a sudden impulse that projects and displaces both Mc and nB out of the microscope field vision leaving a PFC gas cloud behind. In our case, perfluorononane is used as the PFC fuel, and although it has a boiling point of 125-126 ºC,[43] under application of an ultrasound pulse it displays a spontaneous phase shift from a liquid to a gas state.[35] Such vaporization event results from the collapse of the PFC gas microbubbles after the peak negative pressure exceeds its threshold, indicating that this process does not follow linear or exponential dependence on the applied ultrasound power.

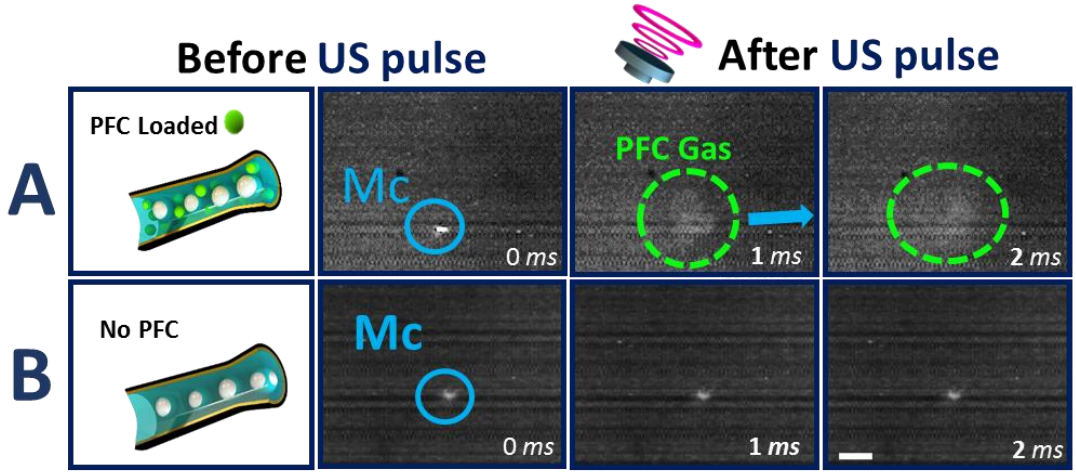

Figure 3.1.4. Mc loading schematic and time-lapse images of the Mc before (left) and after (right) application of US pulse. (A) Images illustrating the US-triggered vaporization of the PFC-emulsion embedded inside the Mc. The rapid expansion of the PFC microbubble is responsible for the firing and propulsion thrust of the nB. (B) In the absence of PFC in the Mc, no firing, motion or ejection is produced. Scale bar, 45μm.

While the nB ejection from the Mc cannot be recorded from these images, such firing will be clearly documented in the following sections. Subsequent control experiments were performed using silica nB-loaded Mc structures without the PFC emulsion. No firing, motion of Mc or ejection of bullets are observed in this case (see Figure 3.1.4B), supporting the hypothesis that the firing is caused by vaporization of the PFC emulsion (as was demonstrated previously by Kagan *et al*[19]), and not by an acoustic pressure displacement.

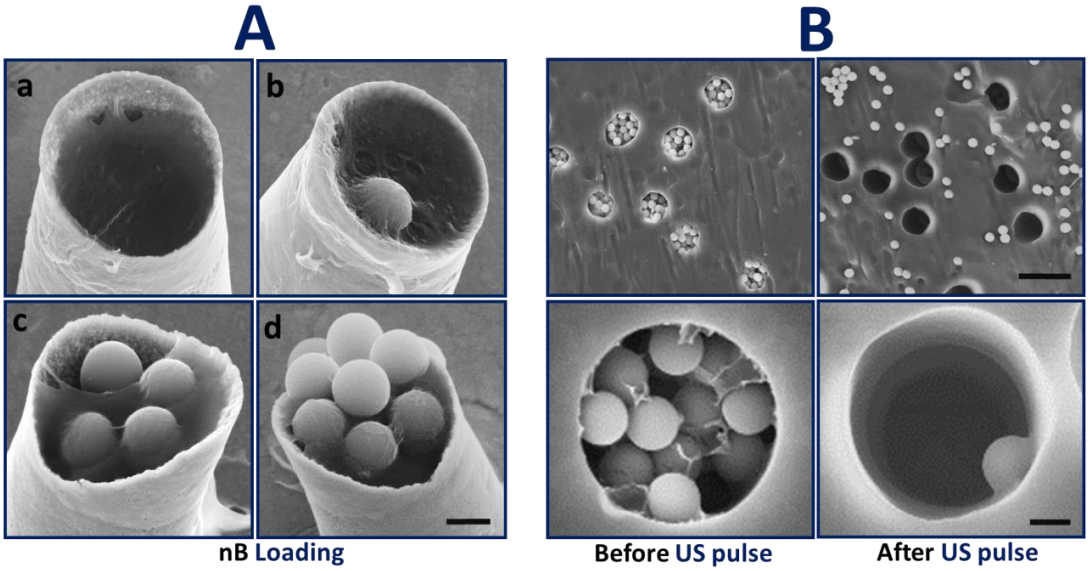

Figure 3.1.5. (A) Tunable nB loading density in the gel matrix: (a) no nB, (b) low nB concentration, (c) medium nB concentration and (d) high nB concentration (scale bar, 1 μm). (B) SEM micrographs showing firing characterization of static Mc confined within multiple micropores of the template membrane (top, scale bar 10 μm) and detail of single Mc. (bottom scale bar, 1 μm); before the US pulse (left) and the ejection of cargo nB after the US pulse (right).

The number of nB loaded into the Mc can be adjusted by controlling the density of the nB embedded in the gel matrix, as shown in Figure 3.1.5A. These scanning electron microscopy (SEM) micrographs demonstrate the efficient and tailored loading of different

nB concentrations inside the Mc structure: from a gel matrix not containing nBs (Figure 3.1.5A,a) to a high packing density of nB (with minimal gaps) using the original commercial nB concentration (Figure 3.1.5A,d). Further (1:1000 and 1:100) dilutions of the original concentration result in low or medium nB loadings, respectively (Figure 3.1.5A, b-c).

To obtain a better characterization and visualization of the firing mechanism, we evaluated static Mcs prepared using the same template electrodeposition protocol, but without dissolving the polycarbonate template. This leads to an array of multiple confined microcannons pointing in the same direction. The SEM images of Figure 3.1.5B illustrate the loading and ejection of nBs from the static microcannons (eight Mcs on top and a single one on bottom). Each micropore of the template membrane contains a bilayer graphene/gold tubular Mc structure and is fully loaded with PFC emulsions and silica-nBs within the gel matrix. The loading mechanism of the cargo by a gel matrix is efficient, reproducible and essential to maintain the tightly-packed cargo inside the cannon; free nBs outside the micropore membrane structure are removed during a thorough washing procedure (see Figure 3.1.5B left). After application of the US pulse, the silica nBs are ejected from the micropores and released toward the upper part of the membrane. A negligible number of silica bullets remain in the Mc structure (see Figure 3.1.5B right). Such ability to fire a large amount of nBs is essential for enhanced effectiveness (e.g., therapeutic efficacy in drug delivery).

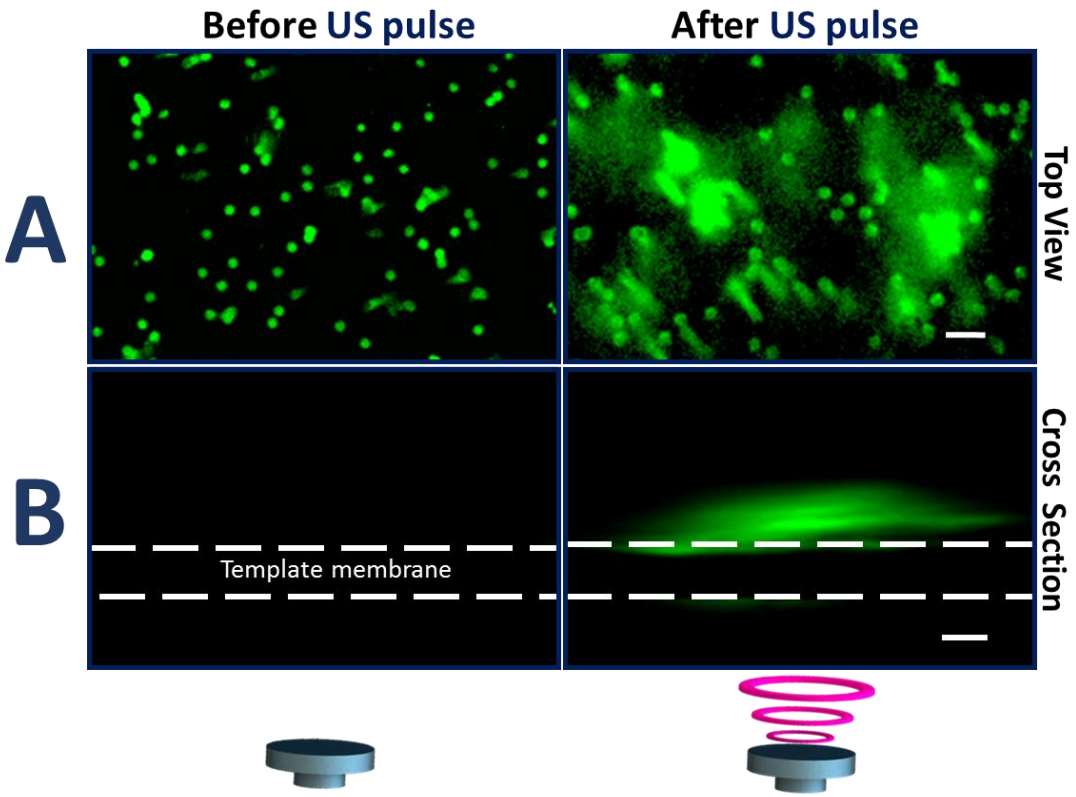

Figure 3.1.6. Fluorescence images of Fluorosphere (Fs)-loaded static Mcs confined in the template membrane (left) and the distribution of the Fs bullets after the US-triggered firing inside a tissue phantom gel matrix (right). (A) Top view, where each point represents one microcannon loaded with Fs bullets. Scale bar 20 μm. (B) Cross section view showing the distance of the bullet penetration within the Agar. Scale bar 20 μm.

To further assess the distance reached by the nBs and demonstrate the versatility of the microballistic approach for loading and shooting different cargoes, static Mcs, confined in the template membrane (as in Figure 3.1.6), were loaded with Fluorospheres (Fs) that were fired towards a tissue phantom gel. The loading of the Fs nBs and the PFC was similar to the previous approach involving silica nBs (see experimental section for details). The tissue phantom gel has acoustic and mechanical properties comparable to real tissues, [44] allowing for the measurement of the distance traveled by these fired nBs and the

examination of the penetration capabilities of the presented microballistic approach. Figure 3.1.6 shows the corresponding fluorescence (top and cross-section) images before and after the US pulse. The top view in Figure 3.1.6A illustrates the Mcs filled with the fluorescent particles prior to the US pulse (3.1.6A left) with each point represents a Mc. A fluorescence 'cloud' is observed after the US-triggered firing (3.1.6A right), illustrating the Fs distribution on the tissue phantom and demonstrating the successful ejection of the Fs nBs from the static Mc upon application of ultrasound. The cross section view in Figure 3.1.6B shows the nBs penetrating 17.5 ± 3.7 μm into the tissue phantom after application of the ultrasound pulse.

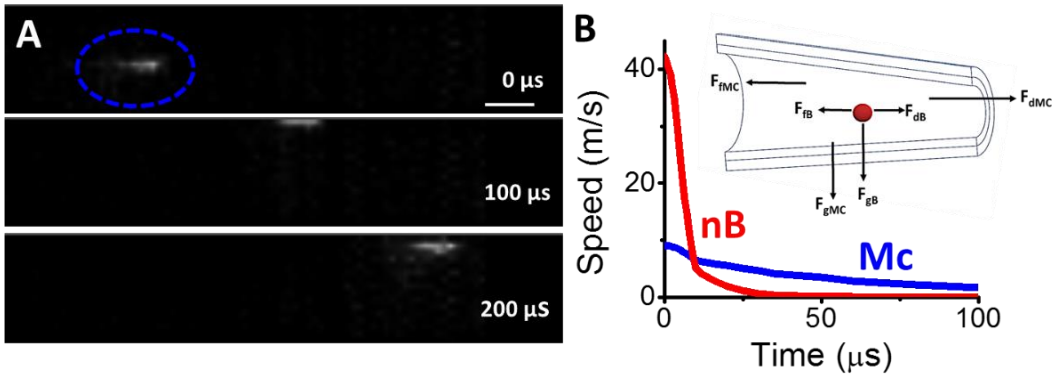

Figure 3.1.7 Experimental and theoretical behaviors of microcannon (Mc, blue) and nanobullet (nB, red) upon firing. (A) Time-lapse frames (0-200 μs) illustrating the displacement of the Mc (circled in blue) upon application of a US pulse recorded under high frame rate (the nB ejection is not shown due to their ultrafast speed). Scale bar 20 μm. (B) Theoretical speed profile of the Mc and nB upon firing; the inset shows schematic of the forces experienced by the Mc and nB, including force of friction (Ff), force of gravity (Fg) and drag force (Fd), the latter being the dominating force.

Due to technological limitations for capturing the nB ejection from the Mc (associated with their ultrafast ejection speed and size), a theoretical model was used to

predict the nB behavior. Taking into consideration that both the Mc and the nB are exposed to the same propulsion thrust of the PFC explosion, the speeds for nB could be modeled by measuring the displacement of the Mc (Figure 3.1.7A) and extrapolating the force to the nB. The Reynolds number, which estimates the relation between viscous and inertial forces,[4, 9] was calculated to be 13.7.

This low Re means that the Mc moves in a laminar flow where viscous forces dominate the motion; thus, the inertia of the objects is negligible.[3,45] Figure 3.1.7B shows a scheme of the forces acting in the two objects under study, the Mc and the nB. These include the force of friction (not considered for the calculation), the gravitational force and the hydrodynamic drag force. The latter is the primary force involved in the propulsion, defined by Stokes's law, and is proportional to the speed of the object. The proportionality constant, k, depends on the shape of the object under study, so it differs from the Mc (cylinder) and the nB (sphere). Since the drag force is responsible for the movement, the instantaneous and initial speeds for an object subject to this propulsion mechanism will be defined following Equations 1 and 2, respectively, were v and v_0 are the instantaneous and initial speeds, respectively, the interval of time in which the object displaces by Δx and m is the mass of the object. The drag factors k for a cylindrical-shaped Mc and for a spherical nB, [46] were calculated to be $8.8 \cdot 10^{-8}$ kg·s^{-1} and $1.9 \cdot 10^{-8}$ kg·s^{-1} respectively.

$$v = v_0 \, e^{(-kt/m)} \qquad \text{Equation 1.}$$

$$v_0 = k\Delta x/(\, m(1 - e^{(-kt/m)} \,) \qquad \text{Equation 2.}$$

The Mc displacement was captured using high-speed camera by considering the change in position of the microcannon over the time considered, resulting in average speed of 1.05 ± 0.26 m/s (n=3). Then, the initial Mc speed was estimated to be 9.0 $m \cdot s^{-1}$, according to Equation 2. This value is in agreement with other microstructures propelled by perfluorocarbon.[19] The theoretical speed of the nB and the consequent initial nB velocity were calculated to be 42.2 m s^{-1} could be estimated, which is around 5 times faster than the speed of the Mc. The instantaneous speed-time profile was theoretically modeled for both the Mc and the nB, as shown in Figure 3.1.7B. The nB attains faster initial speed during the initial microseconds and then rapidly slows down while the speed of the Mc decays more slowly. For simplicity, these approximations were carried out considering that the force is applied only to a single nB; future studies will focus on developing a more precise theoretical simulation accounting for the ejection of multiple nBs. Overall, these theoretical predictions are in agreement with the experimental observations of the optical, fluorescence and SEM images and indicate an ultrafast ejection of the nanobullet from the microcannon.

The Mc displacement was captured using high-speed camera with an average speed for Mc (recording at 109,500 frames per second), by considering the change in position of the microcannon in the time considered lead to 1.05 ± 026 m/s average speed of the microcannons. The visualization of nB firing presents a technological challenge to image and measure its average speed, in part due to their small size and high speed. Therefore, a theoretical approach was used to predict how the nB will react upon ultrasound (US) triggered firing of a Mc free in solution, taking into consideration the forces acting on the

MC, due to both Mc and nB are exposed to the same propulsion thrust of the PFC explosion. The calculation of an approximation of the nB speed was carried out considering that the force is only applied to one nB for simplicity. In order to know which forces dominate in this movement, whether viscous or inertial forces, the Reynolds number was calculated as follows:

$R_e = \rho v L/\mu$ Equation 3.

Re is the Reynolds number that gives information about the type of flow of the object under study. Since the media of study is water and considering ρ, density of the water, 103 kg/m^3, μ, viscosity of the water, 1.0 x 10^{-3} kg m^{-1} s^{-1}, v the speed of the Mc 1.05 m s^{-1} and L, the length, in average 13 μm , Re was calculated to be 13.7. This low Reynolds number suggests that the Mc moves in a laminar flow where the viscous forces dominate the motion and the inertia of the microscale objects is no longer important. This fact was previously explored for other nano/micromachines. Thus, the Mc moves due to the vaporization of the PFN and the expansion of the gas on the cavity, being this one the driving force, then, the primary force is the hydrodynamic drag force, the rest of the forces involved will not be considered. Furthermore, the nB is also experienced by the same force, drag force. Consequently, the force applied to the Mc, FMc is the same that the one applied to the nB loaded in the Mc. The force of the nB will be defined as FnB.

$\overrightarrow{F_{Mc}} = \Sigma n_{nB} \cdot \overrightarrow{F_{nB}}$ Equation 4.

The speed calculations herein estimated must be considered as an approximation because of the important instrumental limitations. Moreover, the measurement of the

distance that the Mc moved in a short period of time should also be considered not completely accurate since it only possible to capture the bullet for 5 or 6 frames under 109,500 frames/s videos. For calculation of the drag factor, the microcannon was modeled with a cylindrical shape, as in previous papers of nano/micromotors fabricated with the same template-based methodology, being the k factor obtained from the Equation 3. Considering the dimension of the Mc, L, length 13 μm, R, radius of 5 μm, k_{MC} was calculated to be 8.8 x 10^{-8} kg/s.

$$k_{MC} = \frac{2\pi\mu L}{Ln\left(\frac{2L}{R}\right) - 0.72}$$ Equation 5.

The mass of each Mc was calculated considering the mass of the gold deposited, the graphene mass contribution was considered negligible o. For that, as the charge, Q, deposited was 1 C, and considering 100% efficiency for the electrodeposition, the mass of gold deposited was estimated using the gold molecular mass, Mmol, the number of electrons involved in the electrodeposition, n, 3 for gold and the Faraday constant, F, 96485 C mol^{-1}.

$$W_{metal} = \frac{M_{mol}\, Q}{n\, F}$$ Equation 6.

The mass of gold deposited was 68 mg, considering that there are around 2.5 x 10^{6} pores in each membrane template, the mass of each microcannon was estimated to be around 2.72 x 10^{-13} kg. The mass contribution of graphene was considered negligible. The bullets are subjected to the same total force than the Mc, however, the sphere shape of the nB (silica particle) make that the drag constant, kNb be calculated as follows,

$k_{NB} = 6\pi\mu R$ Equation 7.

Considering for a water medium, μ, the water viscosity (10^{-3} kg/m s) and R, the radii of the nB sphere, 1.0 μm, the drag constant, k had a value of kNB= 1.89 x 10^{-8} kg/s. Knowing that the density of the silica particles is 2.2 g/cm^3 and the volume of a sphere, 4.2 x 10^{-18} m^3, thus the mass of a particle is 9.24 x 10^{-15} kg.

Another approximation should be required since the Mc and nB are propelled by the same force, drag force, which causes the movement of both objects, thus the initial velocity of the bullet was 42.2 m/s around 5 times faster than the Mc. This approximations were carried out considering the force is only applied to a single nB for simplicity, future studies will focus on developing a more precise theoretical simulation considering the greatest fraction of space occupied by spheres defined by Gauss to be a close-packing of equal spheres with a value of $\pi/(3\sqrt{2})$ the maximum number of spheres which could be loaded will be 45 spheres.

Finally, to demonstrate the potential applications and enhanced permeation ability of this microballistic methodology, a microcannon patch was evaluated for nerve agent decontamination. The loading protocol and skin mimicking phantom models were similar in all experiments. The decontamination experiments were carried out by using the microcannon patch to fire CeO_2 microdoses to decontaminate a skin phantom from the nerve agent methyl paraoxon. This organophosphate agent is of serious concern due to its widespread availability as a pesticide and potential misuse as a chemical warfare agent.[50-

[52] The microballistic decontamination process was quantified by the recovered absorption peak signal of methyl paraoxon under different experimental conditions (Figure 3.1.8A).

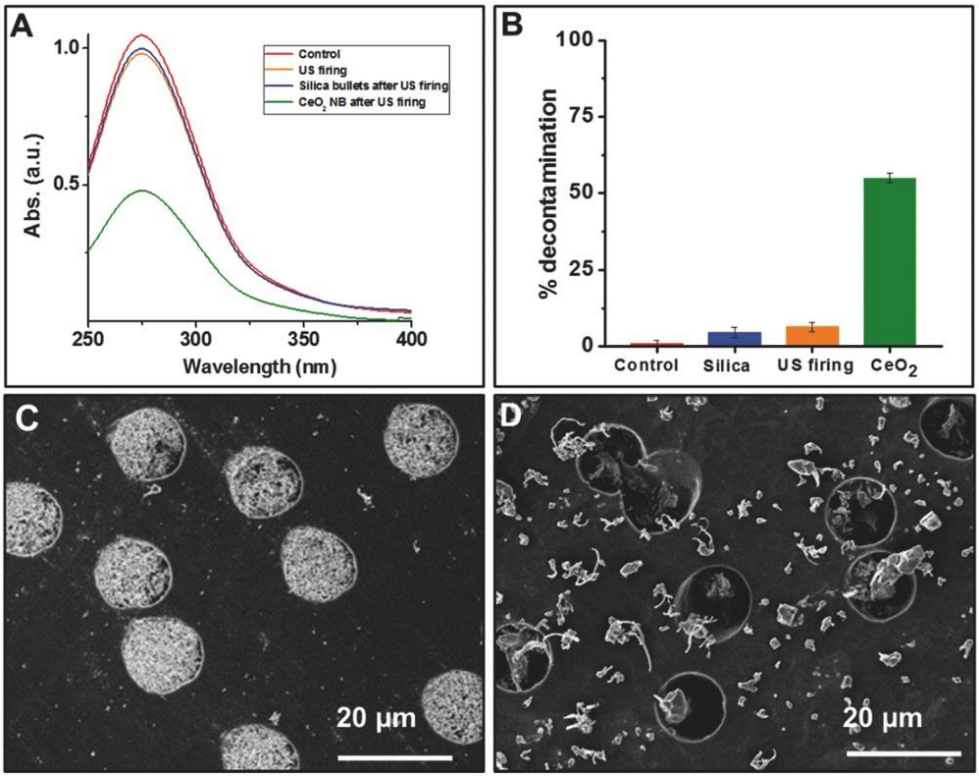

Figure 3.1.8 Use of microcannon patch for OP nerve agent decontamination. Graph illustrating A) the absorption peak of methyl paraoxon and the B) extent of decontamination estimated for diverse controls, measured by UV–vis spectroscopy. SEM micrographs showing firing characterization of multiple micropores of the US patch C) before the US pulse and D) after the ejection of cargo. US parameters: 10 ms, 2.25 MHz.

The initial control experiment, using a microcannon patch, containing only the perfluorocarbon/gel emulsion (without a loaded microdose) and no ultrasound pulse, indicated negligible decontamination; this scenario was set as 0% decontamination. Similarly, independent control experiments were performed to study the effects of both the

applied ultrasound pulse and the firing of inert silica particles (1.2 μm) microdose toward the contaminated phantom skin. These control experiments resulted in an extremely small (<5%) decontamination efficiency. By contrast, the firing of a CeO_2 microdose loaded tattoo patch resulted in nearly 55% decontamination of methyl paraoxon, as illustrated in Figure 3.1.8B. Such decontamination occurs by the absorption/degradation of the methyl paraoxon molecules by the CeO_2 particles.[53,54] Furthermore, when the same quantity of CeO_2 particles was topically administered (drop‐casted) to the skin phantom, only 20% methyl paraoxon decontamination was observed. These data indicate the advantage of the US‐based microparticles penetration into the phantom skin. The successful ejection of these microparticles from the patch is shown by scanning electron micrographs (SEM), illustrating the firing characterization of multiple micropores of the US patch before the US pulse (Figure 3.1.8C) and after the ejection of the microdose (Figure 3.1.8D). It should be noted that, that although the majority of the particles are ejected from the pores, some particles remain trapped inside the pore and gel matrix in the interior of the pores.

3.1.4 Conclusions

We have demonstrated the successful ballistic operation of acoustic microcannons, which allow the efficient loading and firing of nanoscale cargoes as nanoprojectiles. Such firing of large amount nB has been modeled theoretically and demonstrated experimentally. The experimental data supports the theory that the ejection of nanobullets from the microcannon occurs due to PFC vaporization, presenting high power, fast displacement speed and a large biologically-relevant tissue penetration depth. These nanobullets could

thus be used to drive drugs directly deep into diseased tissues or deliver genetic material into cell nuclei for gene therapy, thus revolutionizing drug delivery and the treatment of human diseases. The materials used for fabricating the microcannon (graphene and gold layers) are biocompatible and widely used for biomedical applications.[47-49]

Future work will thus aim at developing this microbullet platform technology for delivering a wide range of therapeutic payloads (including co-delivery of several drugs) and expanding the practical utility of the acoustic microcannons, for their use as single or arrays devices for transporting drug cocktails and vaccines, respectively. The shape and density of the bullet could be further studied to reduce resistance so that the nanobullets would penetrate through the target tissue without dispersing much of its energy. In addition, adding magnetic cargo would allow positioning of the microcannons while firing their load. This study thus paves the way for creating next-generation efficient nanoscale delivery devices capable of delivering their payloads into an identified target, towards the realization of the 'magic bullets' vision.

Chapter 3.1 is based, in part, on the material as it appears ACS Nano, 2015, Fernando Soto, Aida Martin, Stuart Ibsen, Mukanth Vaidyanathan, Victor Garcia-Gradilla, Yair Levin, Alberto Escarpa, Sadik C Esener, Joseph Wang. and Advanced Materials Technologies, 2017 Fernando Soto, Rupesh K. Mishra, Robert Chrostowski, Aida Martin, Joseph Wang. The dissertation author was the primary investigator and author of these papers.

3.1.5 References

1. .R. Sanhai, J. Sakamoto., H.R. Canady, M. Ferrari, Nat. Nanotechnol. 2008, 3, 242244

2. J. Wang, Nanomachines: Fundamentals and Applications; Wiley- VCH: Weinheim, Germany, 2013.

3. E,M. Purcell, Am. J. Phys 1977, 45, 3-11.

4. R.P. Feynman, Eng. sci. 1960, 23, 22-36.

5. D. Walker, M. Kübler, K.I. Morozov, P. Fischer, A.M. Leshansky, Nano Lett. 2015, 15, 4412-4416.

6. G. Zhao, N.T. Nguyen, M. Pumera, Nanoscale, 2013, 5, 7277.

7. B.J. Nelson, I.K. Kaliakatsos, J.J Abbott, Annu. rev. biomed. eng. 2010, 12, 55-85.

8. A.A. Solovev, S. Sanchez, M. Pumera, Y.F. Mei, O.G. Schmidt, Adv. Funct. Mat. 2010, 20, 2430-2435.

9. W. Wang, W. Duan, S. Ahmed, T.E. Mallouk, A. Sen, Nano Today 2013, 8, 531-554.

10 H. Wang, M. Pumera, Chem. Rev. 2015, 115, 8704-8735.

11. A. Chałupniak, E. Morales-Narváez, A. Merkoçi, Adv. Drug Deliv. Rev. DOI: 10.1016/j.addr.2015.09.004.

12. K. Kim, J. Guo, X. Xu, D.L. Fan, Small, 2015 11, 4037–4057.

13. S. Sánchez, L. Soler, J. Katuri, Angew. Chem. Int. Ed., 2015, 54, 1414–1444.

14. L. Soler, V. Magdanz, V. Fomin, S. Sanchez, O.G. Schmidt, ACS Nano 2013, 7, 9611–9620.

15. V.V. Singh, F. Soto, K. Kaufmann, J. Wang, Angew. Chem. Int. Ed. 2015, 54, 6896-6899.

16. R. Cheng, W. Huang, L. Huang, B. Yang, L. Mao, K. Jin, Q. ZhuGe, Y. Zhao, ACS Nano, 2014, 8, 7746-7754.

17. W. Gao, R. Dong, S. Thamphiwatana, J. Li, W. Gao, L. Zhang, J. Wang, ACS Nano 2015, 9, 117–123.

18. W. Xi, A.A. Solovev, A.N. Ananth, D.H. Gracias, S. Sanchez, O.G. Schmidt, Nanoscale 2013, 5, 1294-1297.

19. D. Kagan, M.J. Benchimol, J.C. Claussen, E. Chuluun-Erdene, S. Esener, J. Wang, Angew. Chem. Int. Ed. 2012, 51, 7519-7522.

20. W. Wang, S. Li, L. Mair, S. Ahmed, T.J. Huang, T.E. Mallouk, Angew. Chem. Int. Ed, 2014, 53, 3201-3204.

21. B. Esteban-Fernandez de Ávila, A. Martin, F. Soto, M.A. Lopez-Ramirez, S. Campuzano, G.M. Vasquez-Machado, W. Gao, L. Zhang, J. Wang, ACS Nano 2015, 9, 6756-6764.

22. U. K Gautam, L.S. Panchakarla, B. Dierre, X. Fang, Y. Bando, T. Sekiguchi, A. Govindaraj, D. Golberg, C.N.R. Rao, Adv. Funct. Mat. 2009, 19, 131-140.

23. D. Pissuwan, S.M. Valenzuela, C.M. Miller, M.B.A. Cortie, Nano Lett. 2007, 7, 3808-3812.

24. E. Elinav, D. Peer, ACS Nano 2013, 7, 2883-2890.

25. T. Giesecke, K. Hynynen. Ultrasound in Medicine & Biology 2013, 29, 1359-1365.

26. N. Reznik, O. Shpak, E.C. Gelderblom, R. Williams, N. de Jong, M. Versluis, P.N. Burns, Ultrasonics 2013, 53, 1368-1376.

27. E. Litvak, K.R. Foster, M.H. Repacholi, Bioelectromagnetics 2002, 23, 68-82.

28. C.I Zanelli, S. De Marta, C.W. Hennige, M.M. Kadri,. IEEE Ultrasonics Symposium 1993, 1233-1238.

29. S. Ibsen, M. Benchimol, D. Simberg, C. Schutt, J. Steiner, S. Esener, Journal of Controlled Release, 2011, 155, 358-366.

30. I. Rosenthal, J.Z. Sostaric, P. Riesz, Ultrason. Sonochem. 2004, 11, 349-363.

31. K. Tachibana, L.B. Feril Jr, Y. Ikeda-Dantsuji,. Ultrasonics. 2008, 48, 253-259.

32. K. Okada, N. Kudo, N. K. Niwa, K.A. Yamamoto, J. Med. Ultrasonics. 2005, 32, 3-11.

33. V. Zarnitsyn, C.A. Rostad, M.R. Prausnitz, Biophys. J. 2008, 95, 4124-4138.

34. D.M. Skyba, R.J. Price, A.Z. Linka, T.C. Skalak, S. Kaul, Circulation 1998, 4, 290-293.

35. S. Ibsen, C.E. Schutt, S, Esener, Drug Des Devel Ther. 2013, 7, 375-388.

36. W.J. Duncanson, L.R. Arriaga, W.L. Ung, J.A. Kopechek, T.M. Porter, D.A. Weitz, Langmuir 2014, 30, 13765-13770.

37. I. Lentacker, S.C. De Smedt, N.N. Sanders, Soft Matter 2009, 5, 2161-2170.

38. C. Wang, S. Kang, Y. Lee, Y.; Luo, Y.; Huang, Y.; Yeh, C. Aptamer-Conjugated and Drug-Loaded Acoustic Droplets for Ultrasound Theranosis. Biomaterials 2012, 33, 1939-1947.

39. H. Huang, H. Liu, P. Hsu, C. Chiang, C. Tsai, H. Chi, S. Chen, Y.A Chen, Adv Mater 2015, 27, 655-661.

40. A. Martin, B. Jurado-Sánchez, A. Escarpa, J. Wang, Small 2015, 11, 3568-3574.

41. Z. Wu, X. Lin, X. Zou, J. Sun, Q. He, ACS Appl. Mater. Interfaces 2015, 7, 250-255.

42. B. Daglar, G.B. Demirel, T. Khudiyev, T. Dogan, O. Tobail, S. Altuntas, F. Buyukserin, M. Bayindir, Nanoscale 2014, 6, 12710-12717.

43. E.C Lugert, T.P. Lodge, P. Bühlmann, J. Polym. Sci. Pol. Phys. 2008, 46, 516-525.

44. S. Ibsen, M. Benchimol, S. Esener, Ultrasonics 2013, 53, 178-184

45. J.G. Gibbs, Y. Zhao, Small 2009, 5, 2304-2308.

46. L. Li, J. Wang, T. Li, W. Songa, G. Zhanga, Soft Matter 2014, 10, 7511-7518

47.C. Bussy, H. Ali-Boucetta, K. Kostas, Accounts of chemical research, 2012, 43, 692-701.

48. Bianco, A. Graphene: Safe or Yoxic? The Two Faces of the Medal. Angew. Chem. Int. Ed., 2013, 52, 4986-4997.

49. N, Li, P. Zhao. D. Astruc, Angewandte Chemie International Edition, 2014, 53, 1756-1789.

50 B. E. Mileson, J. E. Chambers, W. Chen, W. Dettbarn, M. Ehrich, A. T. Eldefrawi, D. W. Gaylor, K. Hamernik, E. Hodgson, A. G. Karczmar, Toxicol. Sci. 1998, 41, 8.

51 R. Rapini, G. Marrazza, Compr. Anal. Chem. 2016, 74, 3.

52 R. K. Mishra, A. V. Mohan, F. Soto, R. Chrostowski, J. Wang, Analyst 2017, 142, 918

53. A. Salerno, T. Devers, M. ‐ A. Bolzinger, J. Pelletier, D. Josse, S. Briançon, Chem. ‐ Biol. Interact. 2017, 267, 57.

54. P. Janos, P. Kuran, M. Kormunda, V. Stengl, T. M. Grygar, M. Dosek, M. Stastny, J. Ederer, V. Pilarova, L. Vrtoch, J. Rare Earths 2014, 32, 360.

3.2 Mechano-chemical blood clot degradation by acousto-ballistic microengines

3.2.1 Introduction

Nanomachines consist of nano/microstructures capable of converting local or external forces into motion in order to perform specific tasks.[1-8] In recent years, these tiny machines have been applied to multiple practical application in a diverse range of fields.[9-16] They particularly demonstrate a unique potential to revolutionize treatment of human diseases, in part due to their ability to enhance fluid transport at small scales, thereby, accelerating reactions and recognition events,[17-21] to be precisely localized to reach places and operate where macroscopic tools cannot,[27-29] and to selectively release diverse cargoes.[22-26] More specifically, nanomachines are ideal candidates as surgical tools for unclogging blocked blood vessels, as traditional tools, such as catheters[30,31] and pharmaceuticals,[32,33] are not always desired due to their invasiveness and side effects, respectively.

In this direction, we introduce a nanodevice named cardio-bullet as new surgical tool for mechano-chemical degradation of blood clots. The cardio-bullet consists of a hollow truncated multilayer (graphene, gold, and iron) microcone structure which is loaded with a perfluorocarbon fuel emulsion and Tissue plasminogen activator (Tpa). A high-intensity focus ultrasound pulse is used to trigger the rapid vaporization of the loaded fuel, which generates a directional thrust to eject the cardio-bullet against its target. The cardio-bullet can operate powerfully in real-life biological media such as whole blood. Additionally, the magnetic properties (given by its iron segment) allow, by using a

magnetic field, to control its location close to the targeted blood clot. The unclogging of the blocked vessel was carried out inside a partially obstructed vessel with circulating fluid flow. The generation of a traveling stress shockwave through the blood clot surface due to the cardio-bullet firing, in combination with Tissue plasminogen activator, results in the degradation of the blood clot from the obstructed artificial vessel wall, and further recovery of the original flow speed. Through offering access to reach challenging places and reducing the side effect of pharmaceuticals, this new microballistic approach to mechanically unclog blocked vessels could pave the way for the enhancing treatment of cardiovascular diseases.

3.2.2 Experimental Methods

Cardiobullet Fabrication

The cardio-bullets were prepared using a template electrodeposition methodology.[38-40] This synthesis consists of sequential electrodeposition of materials into a porous polycarbonate (PC) membrane containing 5 µm conical-shaped micropores (Catalog No. 7060-2513; Whatman, Maidstone, U.K.). Firstly, a gold film is sputter (equipment, 90 sec, 3 mtor, 65 rotation speed) on one side of the membrane to serve as the working electrode. A Platinum wire and an Ag/AgCl electrode (1 M KCl) were used as counter and reference electrodes, respectively. Graphene oxide solution (1 g/mL, 0.1 M H_2SO_4, 0.5 M Na_2SO_4) was electrochemically reduced by cyclic voltammetry (+0.3 to -1.5 V, 50 mVs^{-1}, 5 scans) within the micropores being the outer layer of the cardio-bullet.[39] Subsequent layers of gold and iron were deposited using amperometric methods. For the

gold deposition, -1.5 C of commercial plating solution (Orotemp 24 RTU RACK; Technic, Inc., Anaheim, CA) was electrodeposited at -0.90 V, and for iron, -1.5 C of a solution of 0.2 M $FeSO_4$, 0.4 M H_3BO_3, 0.7 M Na_2SO_4, pH 2.5, was deposited at -1.15 V.

Then, the gold sputter was polished using alumina beads (0.3 μm), and afterward a hydrogel containing40 mg/mL gelatin, 1 μg of tPA (ProSpecBio) and a 1:100 perfluorocarbon emulsion where infiltrated within the pores. The membrane template was finally dissolved by methylene chloride for 5 min to completely release the cardio-bullets. They were collected by centrifugation at 7000 rpm for 3 min and repeatedly washed with ethanol and then three times with ultrapure water (18.2 Ω cm), with a 3 min centrifugation between washes. Cardio-bullets were used after synthesis at room temperature.

Blood Clot and microfluidic fabrication

The blood clots were prepared by mixing 40 μL of whole blood, thrombin and calcium chloride on a 1.5 mL centrifuge tube, the blood was left to coagulate and cut into small segments. These pieces were stored in saline solution before testing. Y Shaped PDMS microchannels were fabricated via UV-lithography on pre-coated AZ1512on a 4 inches silicon wafer using 20 nm Cr metal layer. The wafer was exposed and develop with AZ MIF 300 Developer, and etching of the Cr layer, the silicon wafer was dry etched (Oxford Plasmalab 100 RIE/ICP, Oxford Instruments, UK) getting 450 μm depth features. Sylgard 184 Silicone Elastomer Curing Agent (Dow Corning, MI, USA) and Sylgard 184 Silicone Elastomer Base were mixed at 1:10 weight ratio, casted on top of the silicon mold, and cured at 80 °C for 60 min. A blood clot was later placed manually inside the PDMS

channel. Finally, the glass substrate and the PDMS microchannels were both treated with ozone and bonded.

Cardio-bullet imaging and ultrasound equipment

For dynamic cardio-bullet firing on the clot, images and videos were taken in an inverted optical microscope (Nikon Eclipse Instrument Ti-S), coupled with 4X objectives, and a Hamatsu digital camera C11440 and FrameLink Express software. To capture the cardio-bullet propulsion, videos were acquired at 6000 (fps) using a FASTCAM 1024 PCI high-speed camera (Photron, San Diego, CA) and a 20X objective. Cardio-bullet propulsion was performed by exposure of a focused ultrasound pulse using a custom designed ultrasound and microscope system.[38,41] A PCI-5412 arbitrary waveform (National Instruments, Austin, TX) was used to create a single 10 ms long US pulse at 2.25 MHz. A 300 W amplifier (Vox Technologies, Richardson, TX) was used to create a peak negative pressure of 1.9 MPa at the focal zone with a Panametrics V305-SU transducer (Olympus NDT Inc., Waltham, MA). A custom-designed LabVIEW 8.2 program was utilized to initiate the US pulses. The transducer was submerged in a water tank while a Petri dish containing the sample was positioned at the water surface placing the sample in both the focal zone of the optics and the US transducer[38]. For cardio-bullet performance (magnetic guidance and movement), cardio-bullet on whole blood were placed in a Petri dish. However, for dynamic experiments, a microfluidic chip was used.

3.2.3 Experimental Results

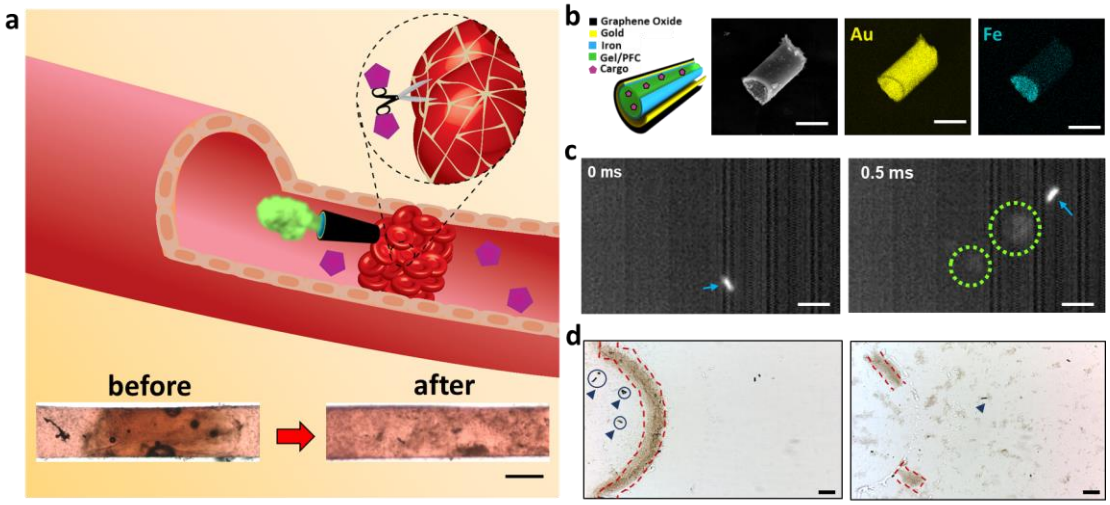

Figure 3.2 1. Use of cardiobullet as a surgical tool for unclogging blocked vessels. (a) Schematic of the cardiobullet's firing and releasing TPA (purple hexagons) at blood clog, inset: actual mechano-chemical degradation before and after firing TPA-loaded cardiobullets. Scale bar, 250 μm. (b) Scheme of cardiobullet's composition (i) consisting in, a graphene oxide outer (black) layer followed by gold (yellow) and iron (blue) layers, filled with gel containing the cargo (red) and PFC emulsion (green). (ii) SEM picture and EDX for (iii) gold and (iv) iron content. (c) cardiobullet's firing mechanism, illustrating still frame images which show the formation of a bubble cloud from the tail of a PFC-loaded Cb upon firing of an US pulse signal. (Blue arrow indicates Cadiobullet position; green dotted lines outline the of a PFC gas bubble). Scale bars: 5 μm. (d) Images illustrating the cardiobullet induced rupture of a clot barrier before (left) and after US firing (right). (Blue Arrows indicates the cardiobullets' position; red dotted lines outline the blood clot). Scale bars: 50 μm. US parameters: 20 ms, 2.25 MHz.

The operation of cardio-bullets to unclog blocked vessels is illustrated in Figure 3.2.1a which shows images of a blocked and unblocked vessel before and after the use of the cardio-bullets for mechanochemical degradation of the blood clot, respectively, is presented in The cardio-bullets are synthesized through template electrodeposition within the micropores of a polycarbonate membrane.[38-40] Figure 3.2.1b shows a schematic of the

materials composition of the cardio-bullet, and scanning electron microscopy images along with EDX of a single cardio-bullet, which clearly illustrate a truncated cone structure, with measurements of 5 μm in diameter and 13 μm in length. From outer to inner layers, the cardio-bullet is composed of different electrodeposited layers of electrochemically reduced graphene oxide (erGO), gold, and iron. The built-up cardio-bullet structure is then filled with a liquid gel matrix containing a perfluorocarbon emulsion, via gravity and capillary forces. The activation of the cardio-bullets relies on the application of a targeted high-intensity focus ultrasound pulse generated by a piezoelectric transducer, which induces the vaporization of the perfluorocarbon fuel. Such rapid gas expansion inside the cardio-bullet structure generates enough thrust[41,42] to launch the cardio-bullet (Figure 3.2.1c) This process is similar to that of gunpowder of a bullet exploding within a gun barrel and propelling the bullet forward. The mechanical rupture of a clot wall produced by a swarm or cardio bullet is shown in Figure 3.2.1d, thus demonstrating the effect of application of mechanical force on the clot structure.

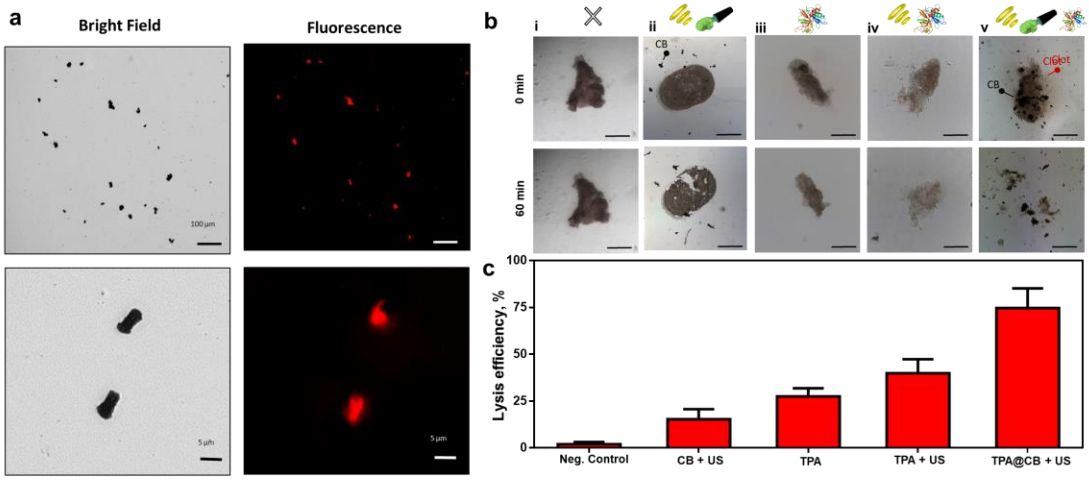

Figure 3.2 2. Static Assay Evaluation of blood clot degradation under diverse experimental conditions. (a) Bright field and fluorescence micrograph illustrating CB loading with Rhd-B. (b) Actual pictures at 0 min (top) and 60 min (bottom) after, (i) no treatment conditions, negative control, (ii) firing of TPA@Cb triggered by US pulse, (iii) addition of 40 µg/ml of free TPA, (iv) addition of 40 µg/mL of free TPA and application of US pulse, and after (v) firing of TPA@Cb triggered by US pulse. Conditions schematized on top. Scale bar: 100 µm. US parameters: 20 ms, 2.25 MHz. c) Lysis efficiency correspondent to the normalized blood clot area after one hour, upon application of the different experimental conditions shown in panel a. (Error bars, n =4).

Optical and fluorescent images were carried out to examine loading of a model therapeutic imaging agents. Figure 3.2.2a shows a group of cardiobullets loaded with Rhd-B (red). The full coverage of the dye illustrated in the fluorescence microscopy images indicates the successful incorporation of the model drug inside the cannon structure. The use of the mechano-chemical approach towards blood degradation was first tested by using large blood clots pieces (~150 µm in diameters) and subjecting them to diverse experimental conditions, following by an examination of lysis efficiency by measuring the change in area of the blood clot. (Figure 3.2.2b) As expected, the negative control did not present significant change. The use of cardiobullets alone resulted the cracking of the blood clot. Nevertheless, the blood clot mostly remained as one large piece, indicating that

mechanical force alone is not enough to reduce the size of the clot. The use of free enzyme in solution displayed a 2% amount of degradation and this value increase to 18% in the presence of an ultrasound pulse. In contrast the blood clot degradation increased to 75 % by the combinatorial use of the cardiobullet mechanical force and TPA enzymatic degradation. Overact the graph in figure 3.2.2c. Clearly demonstrate, the key advantage of combining the mechanical force with the high enzymatic activity of TPA towards mechano-chemical blood clot degradation.

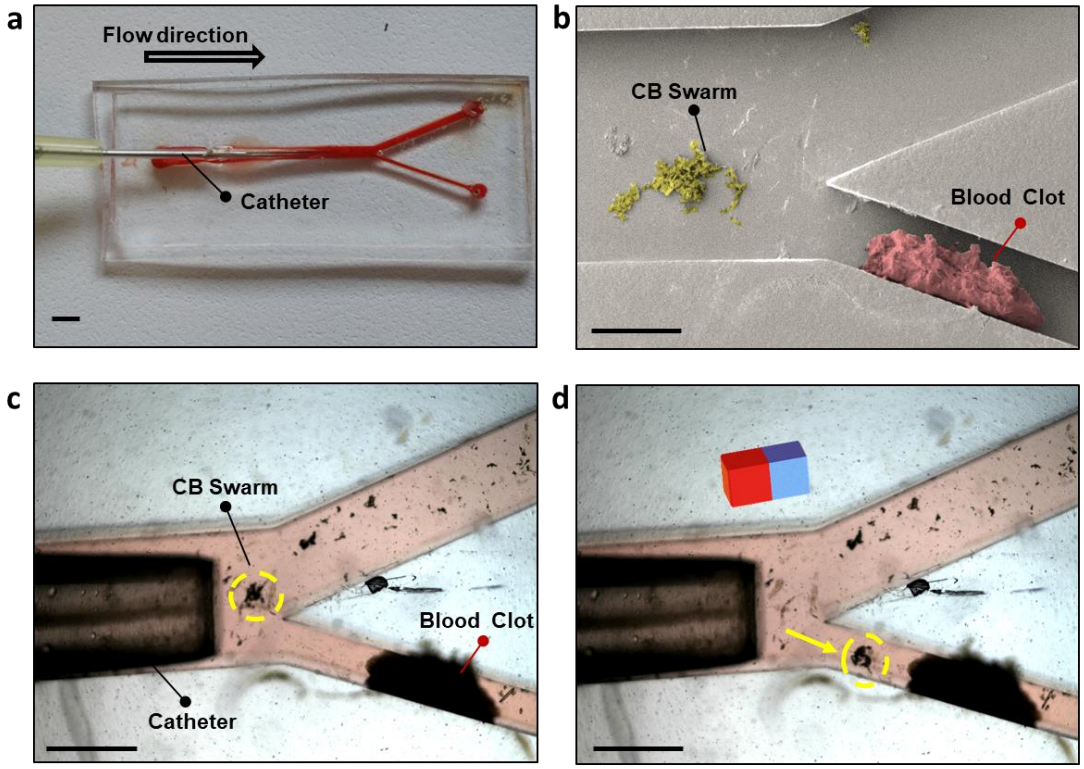

Figure 3.2 3.Clogged microfluidic blood vessels. a) Microfluidic Y-shape device including one broad and one thin channels downstream. b) Scanning electron micrograph with false-color for highlighting blood clot (red) and CB swarm (yellow) inside a microfluidic vessel. c) Real picture showing the catheter not able to reach the blood clot, while d) CB swarm can be magnetically driven to the blood clot. Scale bars, 500 µm

The ability to deploy large numbers of cardiobullets in vessel-like environments, is essential towards potential biomedical applications. Herein, we demonstrated the ability to transport and deliver the cardiobullets within a clot microfluidic channel network. A PDMS-based microchip device with a Y-shaped channel was used to test the localization of the cardiobullets towards an embed blood clot. A 22 gauge catheter (Figure 2.3.3a) was used to deliver a swarm of cardiobullets to the vessel mimicking microfluidic channel. The size ratio between a swarm of cardiobullets and a blood clot blocking one the Y-Shape channels, is shown in (Figure 2.3.3b). The cardio-bullets were magnetically guided towards the blood clot using an external permanent magnetic field over distances in the centimeter range, allowing them to be spatially located in the desired location within the artificial vessel. (Figure 3.2.3 c and d).

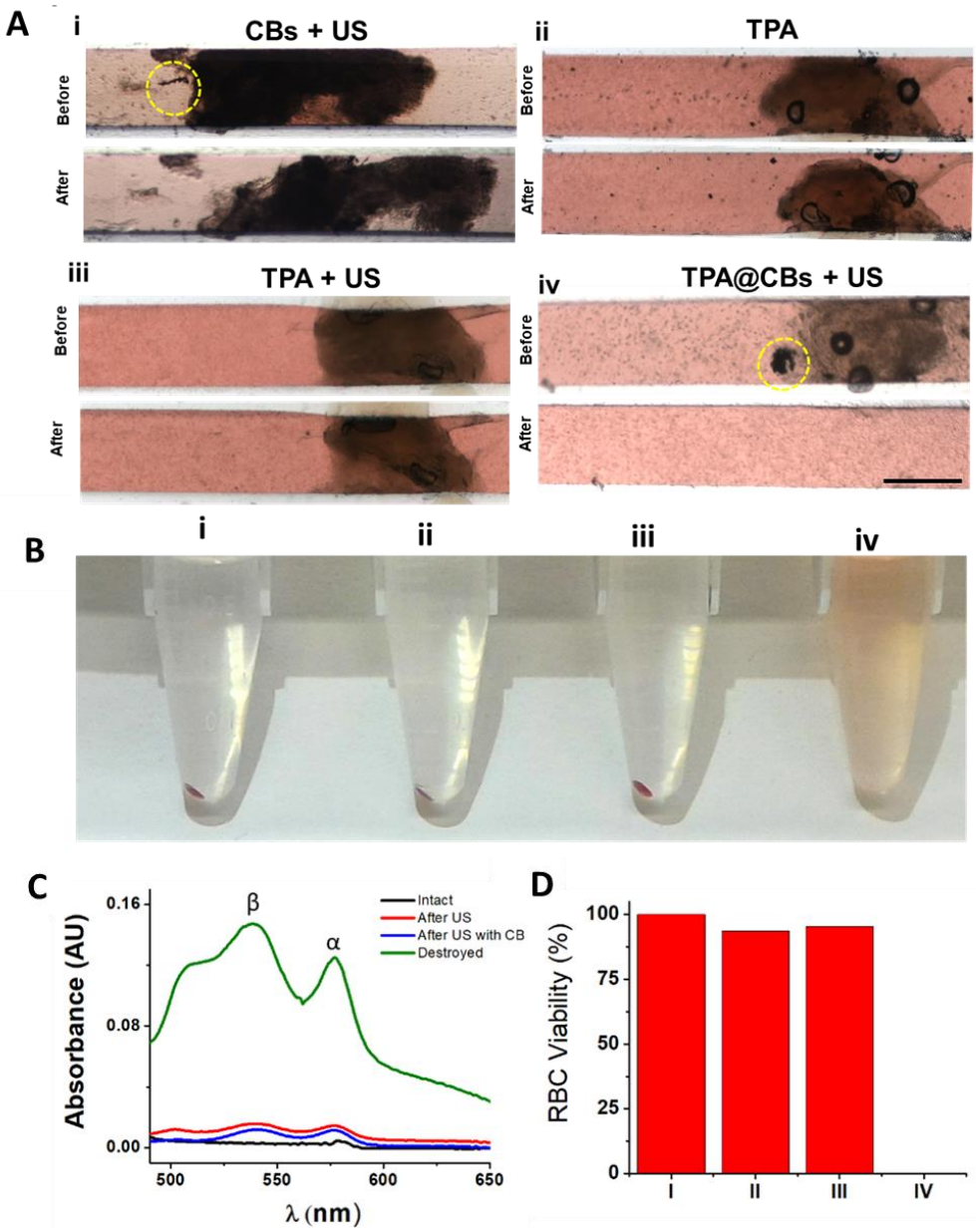

Figure 3.2 4. Unclogging microfluidic blocked mimicking vessels. Microscopy images on blot clot degradation during (i) firing cardiobullets (ii) treatment with free TPA (40 µg/mL), (iii) treatment with free TPA (40 µg/mL) and US pulse, and (d) firing of loaded Tpa@cardiobullets. At time 0 min (top) and 30 min after treatment and flow (bottom). Scale bar, 250 µm. Viability of Red blood cells. b) Pictures of centrifuged RBC under, i) no treatment, intact cells, ii) after US pulses, iii) after US pulses in presence of cardiobullets and iv) destroyed RBC. c) UV-Vis spectra of hemoglobin release in the supernatant showing α and β UV-bands. d) Graph indicating the RBC viability percentage after the different treatments.

We tested the use of cardiobullets as a surgical tool for unclogging dynamic blocked mimicking vessels. To test such capabilities, we tested the effect of diverse experimental conditions towards destroying a blood clot trap in a 300 μm channel after 30 minutes of constant fluid flow. The firing of a swarm of cardiobullets dislodged a segment of the blood clot, but most of its structure remained unaffected, and continue to block the channel. The use of free TPA (40 μg/mL) and TPA with the application of a high intensity ultrasound pulse also presented reduction in the blood clot surface, but the clot remained blocking the channel. In contrast the combinatorial use of cardiobullets loaded with TPA, resulted in the breaking and degradation of the blood clot, and eventually to recover flow in the channel. The mechanism behind the unclogging phenomena is based on the induced shockwave stress generated by the cardio-bullets upon the blood clot, which enables the TPA molecules to permeate through the clot biological barrier. Finally, we tested the viability of regular RBCs to the different experimental conditions, including application of a high-intensity ultrasound pulse with and without cardiobullets and destroyed RBC. The images figure show RBC after the different treatments. There were minor damages to the RBC structure as shown in graph and d illustrating the UV-Vis spectra and graph of hemoglobin release in the supernatant showing α and β UV-bands (Figure 3.2.4 C and D).

3.2.4 Conclusions

We have demonstrated the ability of magnetically guided and ultrasound triggered cardio-bullets to unclog blocked artificial vessels in dynamic environments. We hypothesize that the powerful thrust generated by the perfluorocarbon rapid vaporization is capable of creating a shock wave through the blood clot structure, which combined with the chemical degradation produced by the TPA enzymes, results in the degradation of the blood clot from the obstructed vessel wall, thus recovering the original flow circulation. This new microballistics mechanochemical approach unclog block vessels could pave the way to development of powerful nanorobots capable of revolutionizing treatment of human diseases by offering access for hard to reach places and reducing the side effect of pharmaceuticals.

3.2.5 References

1. J. Wang, Nanomachines: Fundamentals and Applications; Wiley- VCH: Weinheim, Germany, 2013.

2. M. Palagi, A.G. Mark, S.Y. Reigh, K. Melde, T. Qiu, H. Zeng, C. Parmeggiani, D. Martella, A. Sanchez-Castillo, N. Kapernaum, F. Giesselmann, D.S. Wiersma, E. Lauga, P. Fischer, Nat. Mater. 2016, 15, 647– 653

3. B. Dai, J. Wang, Z. Xiong, X. Zhan, W. Dai, C.C. Li, S.P. Feng, J. Tang, Nat Nanotech, 2016, 11, 1087.

4. S. Schuerle, I.A.Vizcarra, J. Moeller, M.S. Sakar, B. Özkale, A.M. Lindo, F. Mushtaq, I. Schoen, S. Pané, V. Vogel, B.J. Nelson, Science Robotics, 2017, 2, eaah6094.

5. F. Wong, A. Sen, ACS Nano, 2016, 10, 7172.

6. C. Chen, F. Mou, L. Xu, S. Wang, J. Guan, Z. Feng, Q. Wang, L. Kong, W. Li, J. Wang, Q. Zhang, Adv. Mater. 2017, 29.

7. Y. Tu, F. Peng, X. Sui, Y. Men, P. B. White, J. C. M. V. Hest, D. A. Wilson, Nature Chemistry 2016, 9, 480.

8. J. Li, W. Liu, T. Li, I. Rozen, J. Zhao, B. Bahari, B. Kante, J. Wang, Nano Letters, 2016, 16, 6604.

9. Sánchez, S., Soler, L. and Katuri, J. (2015), Chemically Powered Micro- and Nanomotors. Angew. Chem. Int. Ed., 54:

10. W. Wang, W. Duan, S. Ahmed, T.E. Mallouk, A. Sen, Nano Today, 2013, 8, 531.

11. J. Li, B. Esteban-Fernández de Ávila, W. Gao, L. Zhang, J. Wang, Sci. Robot., 2017, 2, 1.

12. K. Kim, J. Guo, X. Xu, D.L. Fan, Small, 2015, 11, 4037.

13.A.A. Solovev, S. Sanchez, M. Pumera, Y.F. Mei, O.G.Schmidt, Adv. Funct. Mat. 2010, 20, 2430.

14. H. Wang, M. Pumera, Chem. Rev. 2015, 115, 8704-8735.

15. M. Guix, C. Mayorga-Martinez, A. Merkoçi Chem. Rev., 2014, 114, 6285.

16. X. LIn, Z. Wu, Y. Wu, M. Xuan, Q. He, Adv. Mater., 2016, 28, 1060.

17. J. Orozco, B. Jurado-Sánchez, G. Wagner, W. Gao, R. Vazquez-Duhalt, S. Sattayasamitsathit, M. Galarnyk, A. Cortés, D. Saintillan, J. Wang, Langmuir 2014, 30, 5082.

18. S. K. Srivastava, M. Guix and O. G. Schmidt, Nano Lett., 2016, 16, 817–82.

19. V.V Singh, F. Soto, K. Kaufmann, J. Wang, Angew. Chem. Int. Ed. 2015, 54, 6896-6899.

20. J. Parmar, D. Vilela, E. Pellicer, D. E.-D. L. Ojos, J. Sort, S. Sánchez, Advanced Functional Materials 2016, 26, 4152.

21. J. Li, P. Angsantikul, W. Liu, B. Esteban-Fernández De Ávila, S. Thamphiwatana, M. Xu, E. Sandraz, X. Wang, J. Delezuk, W. Gao, L. Zhang, J. Wang, Angew. Chem. Int. Ed. 2017, 129, 2188.

22. V. Magdanz, M. Guix, F. Hebenstreit, O.G. Schmidt,Advanced materials, 2016, 28 4084.

23. Z. Chen, M. Hoop, N. Shamsudhin, T. Huang, B. Özkale, Q. Li, E. Siringil, F. Mushtaq, L. Di Tizio, B. J. Nelson, S. Pané, Adv. Mater. 2016,

24. 35. B. Esteban-Fernández de Ávila, A. Martín, F. Soto, M. A. Lopez-Ramirez, S. Campuzano, G. M. Vásquez-Machado, W. Gao, L. Zhang and J. Wang, ACS Nano, 2015, 9, 6756-6764.

25. T.Y. Huang, M.S. Sakar, A. Mao, A. J.,Petruska, F. Qiu, X.B.Chen, S. Kennedy, D. Mooney, B.J. Nelson, Adv. Mater, 2015, 27, 6644.

26. J. Li, S. Thamphiwatana, W. Liu, B.Esteban-Fernández de Ávila, , P. Angsantikul, E. Sandraz, E. Wang, T. Xu, F. Soto, V. Ramez, X. Wang, ACS nano, 2016, 10, 9536.

27 R,P..Feynman, Eng. sci. 1960, 23, 22-36.

28. W.Volker, A. Dullaart, A.K. Bock, A. Zweck. Nat Biotechn, 2016, 24, 1211.

29. W. R. Sanhai, J. H. Sakamoto, R. Canady and M. Ferrari, Nat. Nanotechnol., 2008, 3, 242– 244.

30. M.L Linenberger, Journal of the National Comprehensive Cancer Network, 2009, 4, 889.

31. M. C. Bildsoe, G. P. Moradian, D. W. Hunter, W. R. Castaneda-Zuniga, K. Amplatz, Radiology 1989, 171, 231.

32. W. Hacke, JAMA: The Journal of the American Medical Association 1995, 274, 1017.

33. R. Cheng, W. Huang, L. Huang, B. Yang, L. Mao, K. Jin, Q. ZhuGe, Y. Zhao, ACS Nano 2014, 8, 7746.

34. A.A. Solovev, A. N. Ananth, D.H. Gracias, S. Sanchez, O.G. Schmidt, Nanoscale 2013, 5, 1294.

35. D. Walker, B. Ka Sdorf, H.H. Jeong, O. Lieleg, P. Fischer, Science Advances 2015, 1.

36. J. J. Kwan, R. Myers, C. M. Coviello, S. M. Graham, A. R. Shah, A. E. Stride, R. C. Carlisle and C. C. Coussios, Small, 2015, 11, 5305.

37. D. Kagan, M.J. Benchimol, J.C. Claussen, E. Chuluun-Erdene, S. Esener, J. Wang, Angew. Chem. Int. Ed. 2012, 51, 7519-7522.

38. F. Soto, A. Martin, S. Ibsen, M. Vaidyanathan, V. Garcia-Gradilla, Y. Levin, A. Escarpa, S. C. Esener and J. Wang, ACS Nano, 2016, 10, 1522–1528.

39. A. Martin, A. B. Jurado-Sánchez, A. Escarpa, J. Wang, Small 2015, 11, 3568.

40. A. Jodra, F. Soto, M.A. Lopez-Ramirez, A. Escarpa, J. Wang. Chemical Communications, 2016, 52, 11838.

41. S. Ibsen, M. Benchimol, D. Simberg, C. Schutt, J. Steiner, S. Esener, Journal of Controlled Release, 2011, 155, 358.

42. P. Zhang, T. Porter, Ultrasound in medicine & biology, 2010, 36, 1856.

43.L. Soler, C. Martinez-Cisneros, A. Swiersy,.S. Sanchez, O.G. Schmidt, Lab Chip, 2013, 13, 4299.

44. G. Zhao, M. Viehrig, M. Pumera, Lab on a Chip 2013, 13, 1930.

45. J. R. Baylis, J. H. Yeon, M. H. Thomson, A. Kazerooni, X. Wang, A. E. S. John, E. B. Lim, D. Chien, A. Lee, J. Q. Zhang, J. M. Piret, L. S. Machan, T. F. Burke, N. J. White, C. J. Kastrup, Science Advances 2015, 1.

46. P. L. Venugopalan, R. Sai, Y. Chandorkar, B. Basu, S. Shivashankar, A. Ghosh, Nano Letters 2014, 14, 1968.

47. E. Karshalev, C. Chen, G. Marolt, A. Martín, I. Campos, R. Castillo, T, Wu, J. Wang, Small, 2017, 13, 1700035.

48. Z. Li, L. Bai, C. Zhou, X. Yan,L. Mair, A. Zhang, L, Zhang, W. Wang, Particle & Particle Systems Characterization, 2017, 34, 1600277.

3.3 Non-invasive Transdermal Delivery System of Lidocaine Using an Acoustic Droplet-Vaporization Based Wearable Patch

3.3.1 Introduction

Given the staggering global prevalence of chronic and acute pain affecting ≈1.5 billion individuals, there is a growing need to develop novel therapeutic and delivery strategies that can provide suitable treatment for pain management.[1-6] Current therapy modalities have successfully addressed the treatment of neuropathic, anti-inflammatory, and other classes of pain medications. The search for local delivery therapies that offer alternatives to hypodermic injection[7-10] and opioid prescription,[11-13] is both challenging and potentially rewarding, as they could reduce systemic side effects and substance abuse. Current local delivery platforms include the use of microneedles,[14-16] jet injection,[17-20] electroporation,[21-23] and directed physical forces.[24-27] The grand challenge in the field relies on developing wearable and noninvasive platforms that lend themselves to scalability over a wide range of applications without sacrificing their therapeutic efficiency.[28-34] For example, noninvasive lidocaine patches, a local anesthetic used for myofascial and neuropathic pain currently used by pain-management physicians, rely solely on slow diffusion processes, resulting in delayed therapeutic effects.[35-37] Indeed, while dealing with chronic and acute pain patients, a fast therapeutic effect and pain relief are highly desired.

Herein, we present a wearable and noninvasive active method for the transdermal delivery of lidocaine, based on a robust bullet-like acoustic droplet vaporization (ADV) system that breaches dermal barriers. The wearable epidermal patch consists of a flexible

drug reservoir containing hundreds of micropores loaded with lidocaine, and mixed with a perfluorocarbon (PFC) emulsion. The ultrasound-triggered vaporization of the PFC compound[38-41] provides the necessary force to enhance significantly skin penetration and delivery of drug payloads when compared to common systems based solely on passive diffusion or ultrasound pulses.

Moreover, unlike microneedle delivery devices that require to pierce the skin interface, our system achieves enhanced drug permeability through a non-penetrative highly localized stress force produced by the ADV mechanism and suggests a potential non-immunogenic method of delivery. The ability of ADV to deliver large microparticles from microporous membranes[42,43] has been demonstrated earlier toward enhanced decontamination processes. Finally, we demonstrate the preclinical utility of the wearable patch through enhanced delivery and penetration of lidocaine in ex-vivo pigskin model (a model that simulates human skin), as well as achieving high delivery efficacy at significantly shorter periods of time. These findings provide the groundwork for future clinical development where our wearable patch technology could serve as a conduit to target different nerves with diverse depths based on individual patient anatomy, and in connection to other pain-killing drugs, e.g., opioids.

3.2.2 Experimental Methods

Wearable Patch Preparation

Custom made molds were constructed and used to prepare patches using commercial Ecoflex polymer and polyvinylpyrrolidone (PVP). First, a master mold

(Blueacre technology) was reproduced by making counter molds. The master mold was first cleaned and placed in a vacuum pump for 5 min and exposed to CO_2 for 1 min. Next, a PVP mixture was prepared (100 mg mL^{-1} in ethanol) and mixed at 2800 rpm for 5 min, then poured over the mold before letting sit in a vacuum pump overnight to dry. Once the counter-mold was solid, a mixture of commercial Ecoflex was poured over the mold, and subsequently placed in the vacuum pump for 5 min. The mold was lastly put in an incubator at 40 °C to dry for 5 min.

PFC Emulsion Synthesis

PFC emulsions were prepared using an ultrasound probe generator, by mixing PFC with a phosphate buffered solution (PBS) solution in the presence of a lipid monolayer of 1,2-distearoyl-SN-glycero-3-phosphocholine (DSPC) (10 mg mL^{-1}) and methoxypoly(ethylene glycol) 1,2-distearoyl-SN-glycero-3-phosphoethanolamine (mPEG-DSPE) 5k (10 mg mL^{-1}). First, the lipids were dissolved in chloroform and evaporated under nitrogen. Next, the lipids were resuspended in 500 PBS solution and 50 µL of perfluorononane (Sigma). The components were sonicated at maximum power for 5 s using an ultrasonic probe (Ultrasonics Fs 150 N). The emulsion was stored at room temperature.

Piezoelectric Transducer

A V305-SU transducer was submerged underwater (Olympus NDT Inc., Waltham, MA) and generated a high-intensity focus ultrasound pulse (25 ms, 2.25 MHz, and 12 V.)

The focal point of the ultrasound pulse was aimed towards a reservoir contacting the patch, thus resulting in the ADV of the PFC.

Preparation of Agar Gel

A 1% solution of agarose was used to prepare agar gels. For preparing a 100 mL solution of agarose, 100 mL of water was heated on a hotplate at 200 °C until steaming, then 1 g of agarose was added and stirred with a magnetic stir bar. The temperature was increased to 300 °C until the solution became clear, before being brought back to 100 °C. Subsequently, the solution was poured into custom made molds and left to dry for 5 min. For drug delivery experiments, the patch was loaded with a mixture of a 40 µL of a 30 mg mL^{-1} of lidocaine solution, combined with 20 µL of the perfluorononane emulsion.

Electrochemical Measurements

Electrochemical experiments were carried out with a µAutolab Type II, controlled by NOVA software version 1.11. The three-electrode system was performed in a batch system. The three electrodes consist of screen-printed carbon electrodes as the working (WE) and counter electrodes (CE), and a screen-printed Ag/AgCl electrode as the pseudo-reference electrode (RE). SWV was used to determine the electrochemical signals of lidocaine. Voltammograms were investigated at a frequency of 2.5 Hz, an amplitude of 150 mV, and a potential step of 5 mV.

Pigskin Assays

Pigskin was bought at the local supermarket and set to an average thickness of 1.5 mm, thinning it using a stainless steel blade. For penetration assays, samples were subject to a cross section cut utilizing a stainless steel blade and analysis of penetration in an EVOS FL Imaging System Microscope using a 4X objective lens and red fluorescent protein (RFP) filter. For electrochemical measurements the protocol was used as previously described, substituting the phantom tissue with pigskin. For penetration assays, a UV green dye (Bitspower) was used.

COMSOL Multiphysics Finite Element Analysis Simulation:

The solid mechanic's interaction module from COMSOL was chosen to analyze the acoustic cavitation–induced shockwave distribution upon the human skin. A 2D model of human skin with different layers of biological tissues (stratum corneum, epidermis, and dermis) was built. The patch was simplified to the top boundaries of the model. The shockwave force from the patch was applied at the skin interface. The time-dependent study was computed with the time arrangement of 25 ms and the time step of 0.25 ms. The calculated results of von Mises stress were employed to describe the process of the penetration and to evaluate the performance of drug delivery.

3.3.3 Experimental Results

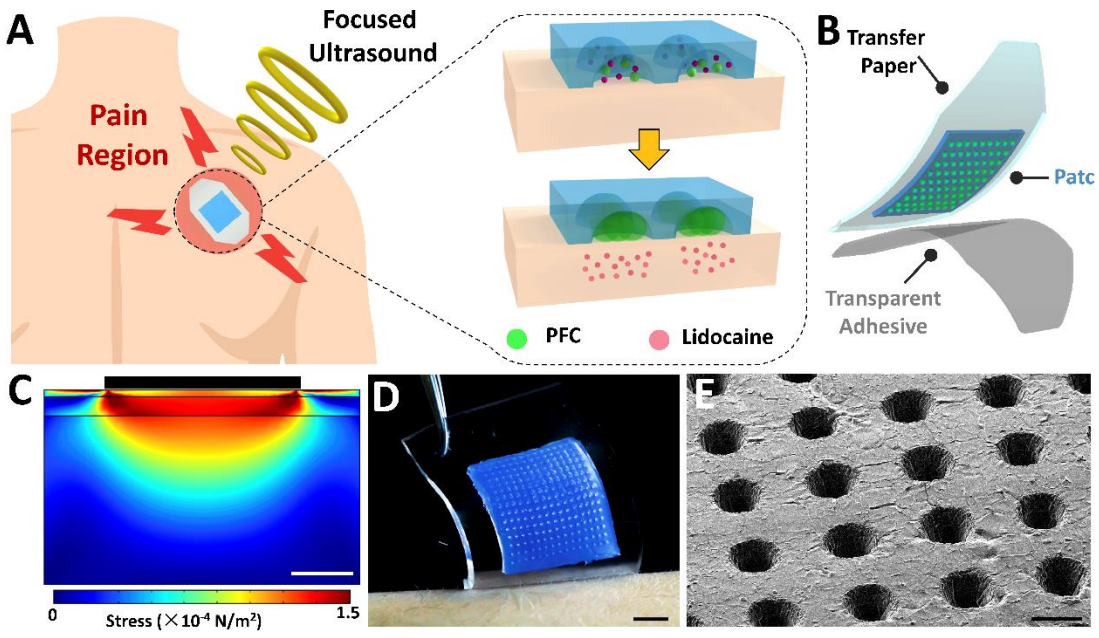

Figure 3.3 1. Principles of the wearable ADV-based drug-delivery patch. A) Scheme of pain management and operational principle of ADV delivery. B) Scheme of different layers of the patch. C) Theoretical simulation of the stress produced upon the dermis by the ADV-based wearable patch. D) Digital photograph of the fabricated lidocaine patch. E) Scanning electron micrograph (SEM) illustrating an array of micropores. Scale bars: (C) 1 mm; (D) 3 mm (E) 250 µm.

This wearable patch combines the commodity and resilience of a disposable flexible medical patch with the faster payload delivery advantages of the ADV platform. The scheme in Figure 3.3.1A illustrate the application of the patch in the pain area and the working principle of ADV delivery, based on the rapid vaporization of the PFC emulsion loaded within the micropores of the patch, leading to the enhanced penetration of lidocaine into the dermis.

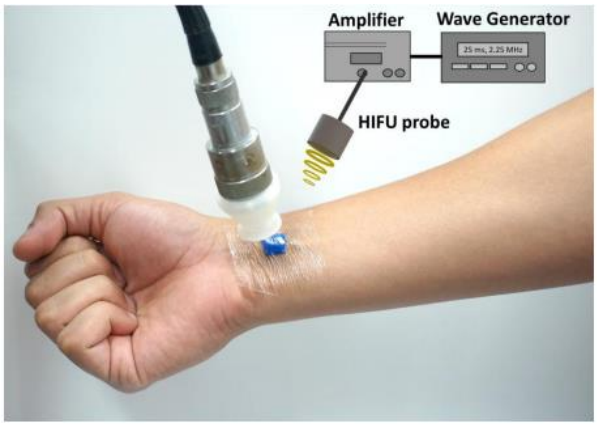

Figure 3.3 2. Proposed translational system towards future tests, illustrating the use of external piezoelectric probe that generates the high intensity focus ultrasound pulse for triggering the ADV mechanism.

Figure 3.1.2 in illustrates the external piezoelectric probe that generates the high intensity focus ultrasound pulse responsible for triggering the ADV mechanism. Figure 3.3.1B shows the distinct layer composition of the ADV patch. The drug reservoir contains hundreds of micropores loaded with lidocaine and PFC emulsion. The US Food and Drug Administration has approved both substances under control dosages.[37, 44]

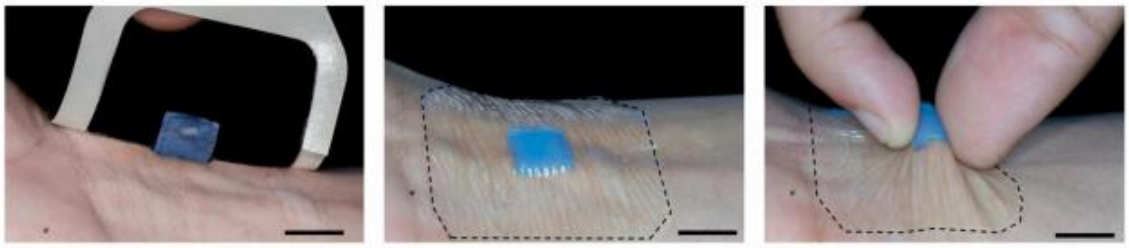

Figure 3.3 3. Application of ADV patch: (left to right) transferring of patch onto the skin; conformational adhesion of the patch on the skin and resiliency test of the skin-worn patch after application of mechanical strain (pinching). A blue dye was added into the patch for enhancing the image by contrasting with skin. Scale bar: 1 cm.

Figure 3.3.3, show the application and adhesion of the patch to the dermis. The patch remained attached to the dermis after 25 continuous pinches, demonstrating its resiliency to mechanical deformation. In addition to emulating real daily-life applications, the flexibility of both patch and adhesive is also essential to minimize the air gap between the patch-skin interfaces, as desired for a more efficient drug delivery procedure. The simulation of the physical force generated by the ADV patch toward the skin is shown in Figure 3.3.1C. The stress is localized close to the epidermis layer, resulting in enhanced payload permeation through the skin. The visual examination of the ADV patch next to the skin is illustrated by a digital photograph of the patch (Figure 3.3.1D) and the scanning electron micrograph (Figure 3.3.1E), showing in detail an array of micropores.

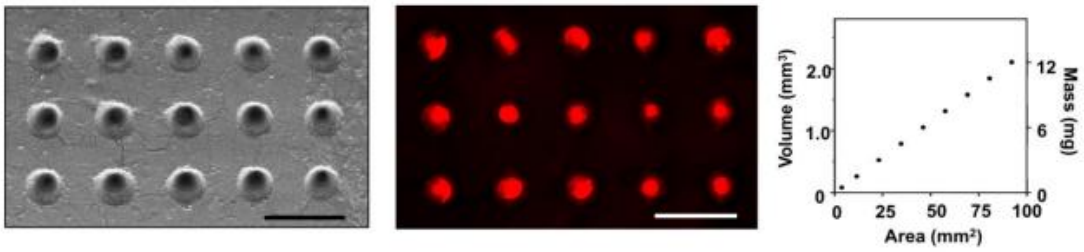

Figure 3.3.4. Characterization of ADV patch. Scanning electron micrograph (SEM) showing a section of the top view of the wearable patch (left) and fluorescence images of Rhodamine 6G-loaded pores (middle). Theoretical volume (left axis) and mass (right axis) loading capacity in different sized patches (right). Scale bars: 480 µm.

Additional characterization of the patch is shown in Figure 3.3.4 in the Supporting Information, which illustrates a top view scanning electron micrograph image of an array of micropores (average pore diameter of 250 µm loaded with a rhodamine 6G dye (center), along with the theoretical loading volume and lidocaine mass loading capacity calculated for different sized patches (right).

We evaluated the delivery of the lidocaine payload under different experimental conditions. Initially, we employed a square-wave voltammetry (SWV) electroanalytical technique for evaluating, in real-time, of the drug delivery kinetics. The scheme in Figure 3.3.6A illustrate the electrochemical setup used, composed of a three-electrode system located at the bottom of the phantom tissue. The phantom tissue model was chosen due to its similar mechano-acoustic properties to human skin.[45,46] Only the lidocaine payload crossed through a 3.0 mm phantom tissue barrier, later being detected by the sensing electrode. These current signals are directly associated with the drug dosage that passed through the skin/reservoir interface.

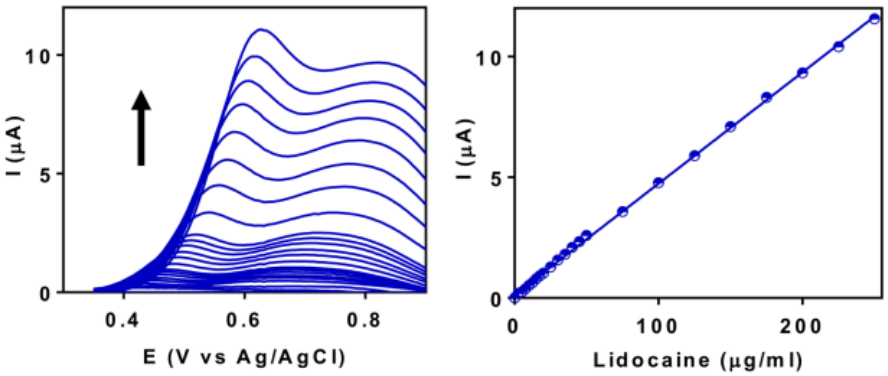

Figure 3.3.5. Square wave voltammograms (SWVs) for different concentrations of lidocaine (left).Corresponding lidocaine calibration plot (right). Currents subtracted by the background response.

The resulting SWV, presented in Figure 3.3.5, showing two distinct oxidation peaks, corresponding to the two-step anodic reactions of lidocaine at the reactive amino group.[47,48] A well-defined calibration plot is obtained within the 2.5–250 µg mL^{-1} lidocaine range using the anodic peak at 0.55 V (sensitivity, 46 µA mg^{-1} mL).

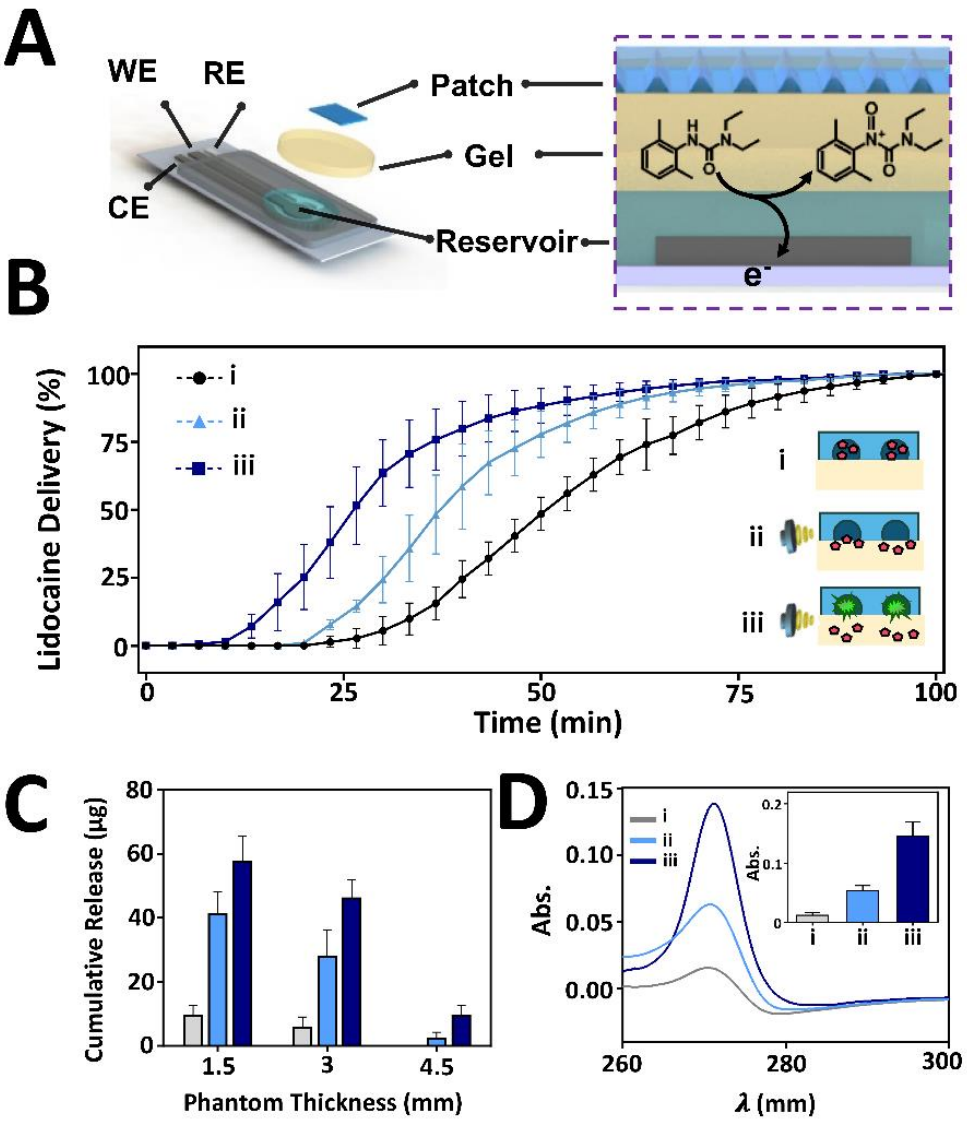

Figure 3.3.6. ADV-based lidocaine delivery evaluation. A) Schematic of the electrochemical set up coupled with the three sensing electrodes (working, reference, and counter electrodes: WE, RE, and CE, respectively) and detection method. B) Release kinetics of lidocaine illustrating the delivery within the mimicking phantom skin (of 3.0 mm thickness). For all subsequent tests, the lidocaine delivery produced by (i) passive diffusion, (ii) ultrasound pulse, and (iii) ADV firing were detected (n = 5). C) Graph of lidocaine delivery obtained after 40 min of application by the experimental conditions previously described, using different phantom gel thickness. (n = 5) D) Additional spectroscopic validation by the recovered ultraviolet (UV)-absorption peak signal and inset plot of the optical signal after 30 min of application of passive diffusion (i), ultrasound pulse only (ii), and ADV (iii), inset illustrating a plot, the recovered UV absorption peak signal produced by different experimental conditions. n = 3.

We compared the delivery efficiency of different experimental conditions, including i) passive diffusion, ii) ultrasound pulse only, and iii) ADV delivery. The release kinetics of each experimental condition is illustrated in the graph of Figure 3.3.6B. A clear advantage of the ADV approach is observed at the 15 min mark, where only the ADV method gives a signal, while no signals are detectable using both the passive diffusion and ultrasound-alone controls. Moreover, at the 30 min mark, the ADV method delivered a higher lidocaine dosage (3.5 µg), compared with diffusion (0.3 µg) and ultrasound only (1.3 µg), represented a 11 and 3 times advantage, respectively. It should be noted that after 90 min, all experimental approaches delivered a similar dose (5.6 µg) of lidocaine.

We also tested the delivery efficacy over phantom tissue with different thickness (1.5, 3.0, and 4.5 mm), as shown in Figure 3.3.6C, illustrating the cumulative lidocaine release 40 min after application. Notice that no signal was observed with passive diffusion after 40 min. In addition to the electrochemical detection, the payload delivery efficiency was also quantified by the recovered UV lidocaine's absorption peak signal after 30 min of different applied experimental conditions. Figure 3.3.6D illustrates the UV absorbance spectra and inset plot, showing the spectrochemical signal of lidocaine that passed through a 3.0 mm phantom tissue. In all cases, the ADV approach presents a distinct advantage of significantly higher delivery efficacy at desirably shorter periods of time.

The potential clinical applicability of our method and its prospects of breaching dermal barriers were evaluated using a pigskin model. Figure 3.3.7A photograph illustrates the screen-printed electrode sensor used to monitor the lidocaine delivery. A skin sample (2.5 mm in thickness) was placed on top of a reservoir containing a phosphate buffer.

Following this step, a patch containing lidocaine was placed on top of the skin sample. Figure 3.3.7B,C illustrate the SWV bar chart of the electrochemical signal of lidocaine that passes through the skin at the 30 min time mark, using passive diffusion (0.17 ± 0.03 μA), ultrasound only (0.36 ± 0.06 μA), and ADV firing (0.73 ± 0.08 μA). The ADV firing enhanced the delivery dosage of lidocaine in short time periods, e.g., fourfold higher, compared with the passive diffusion approach. Figure 3.3.7D,E show fluorescent cross-sectional micrographs and a penetration bar chart of fluorescent molecules (mimicking the drug) permeating through the pigskin, under i) passive diffusion, ii) only ultrasound, and iii) ADV delivery.

The ADV approach (1.2 ± 0.08 mm) enables the therapeutic payload to pass faster through the skin, compared with passive diffusion (0.52 ± 0.05 mm), and ultrasound only (0.96 ± 0.09 mm). Both the ultrasound alone and ADV approaches displayed enhanced penetration when compared to passive diffusion. In the former case, the ultrasound pulse can induce the formation of gaps in the epidermal cell matrix, which facilitate the diffusion of small molecules through such pathways.[49, 50] Nevertheless, the directional stress force produced by the PFC emulsion cavitation resulted in deeper penetration and faster dispersion when compared to the penetration effect associated with acoustic pressure displacement.

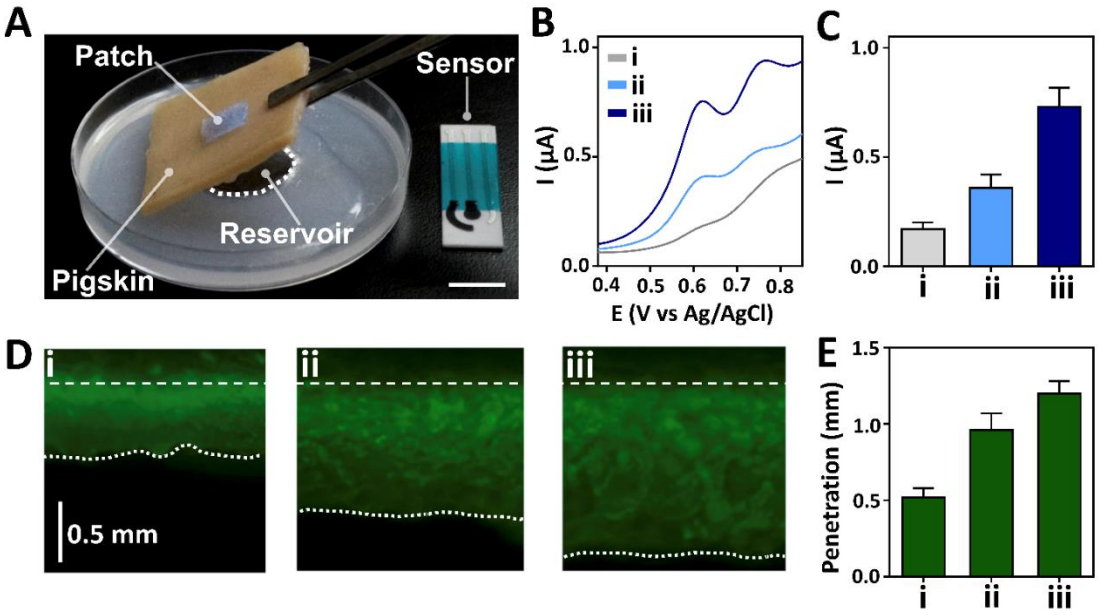

Figure 3.3.7. ADV delivery in pigskin model. A) Photograph illustrating the electrochemical sensor used for measurement of the lidocaine transdermal delivery. B) SWVs of lidocaine delivered through the skin after 30 min by (i) diffusion, (ii) ultrasound only, and (iii) ADV approach. C) Plot showing, the electrochemical signal produced by different experimental conditions. n = 3 D) Fluorescence images of cross-section view, illustrating the penetration depth of the fluorophore within the pigskin by (i) passive diffusion, (ii) ultrasound alone, and (iii) ADV. E) Plot showing the fluorophore penetration by the different treatments (n = 5). Scale bar: (A) 10 mm.

3.3.4 Conclusions

We have demonstrated a noninvasive local lidocaine delivery platform, based on the ADV enhanced therapeutic transdermal transport, aimed at addressing the delayed therapeutic effect and slow pain relief of passive diffusion approaches. Our methodology offers a noninvasive demonstration to deliver drug across the dermis, accomplishing faster delivery to the target site, and promise for tuning the dosage penetration based on modulating the applied ADV force. Further large-scale clinical validation, targeting

different areas of the body with varying nerve depth targets, is required to evaluate the potential of the ADV delivery approach as a chronic pain therapeutic platform and viable opioid sparing approach to treat chronic pain. Moreover, improvements in miniaturization of portable ultrasound probes could leverage this technology to have widespread use as a point-of-care medical device in the clinical setting. In addition, this platform could be further integrated with other wearable devices, opening new possibilities for sensing and transdermal delivery, offering patients a superior alternative to traditional over the counter drug delivery devices relying on passive diffusion such as commercially available topical lidocaine patches. The ADV patch noninvasive platform opens the potential to deliver other drugs, vaccines, or genetic elements, exciting future avenues for ongoing research.

Chapter 3.3 is based, in part, on the material as it appears Small, 2018, Fernando Soto, Itthipon Jeerapan, Cristian Silva‐López, Miguel Angel Lopez‐Ramirez, Ingrid Chai, Lu Xiaolong, Jian Lv, Jonas F Kurniawan, Ian Martin, Krishnan Chakravarthy, Joseph Wang. The dissertation author was the primary investigator and author of this paper.

3.3.5 References

1. Relieving Pain in America: A Blueprint for Transforming Prevention, Care, Education and Research, IOM (Institute of Medicine), 2011, 55 https://www.nap.edu/read/13172/chapter/2 (accessed: August 15, 2017).

2. Global Pain Management Market, Global Industry Analysts, Inc. 2011 http://www.prweb.com/pdfdownload/8052240.pdf (accessed: August 15, 2017).

3. D. S. Goldberg, S. J. McGee, BMC Public Health2011, 11, 770.

4. Al. Taylor, J Law Med. Ethics2007, 35, 556.

5. M. Glajchen, J. Am. Board Fam. Pract.2001, 3, 211.

6. K. V. Chakravarthy, F. J. Boehm, P. J. Christo, Pain Med.2017, 19, 243.

7. N. D. Volkow, A. T. McLellan, N. Engl. J. Med.2016, 13, 1263

8. B. Godin, E. Touitou, Adv. Drug Delivery Rev.2007, 59, 1152.

9. K. S. Paudel, M. Milewski, C. L. Swadley, N. K. Brogden, P. Ghosh, A. L. Stinchcomb, Ther. Delivery2010, 1, 109.

10. R. H. Guy, Handbook of Experimental Pharmacology, Transdermal Drug Delivery, Vol. 197, Springer, Berlin, Heidelberg 2010, p. 339.

11. P. Artursson, J. Karlsson, Biochem. Biophys. Res. Commun.1991, 175, 880.

12. D. Fleisher, C. Li, Y. Zhou, L. H. Pao, A. Karim, Clin. Pharmacokinet.1999, 36, 233

13. L. Manchikanti, A. Singh, Pain Physician2008, 11, 63.

14. Y. Zhang, K. Brown, K. Siebenaler, A. Determan, D. Dohmeier, K. Hansen, Pharm. Res.2012, 29, 170.

15. G. Valdés-Ramírez, J. R. Windmiller, J. C. Claussen, A. G. Martinez, F. Kuralay, M. Zhou, N. Zhou, R. Polsky, P. R. Miller, R. Narayan, J. Wang, Sens. Actuators, B2012, 161, 1018.

16. J. Yu, Y. Zhang, Y. Ye, R. DiSanto, W. Sun, D. Ranson, F. S. Ligler, J. B. Buse, Z. Gu, Proc. Natl. Acad. Sci. U. S. A.2015, 112, 8260.

17. S. Mitragotri, Nat. Rev. Drug Discovery2006, 5, 543.

18. J. Schramm, S. Mitragotri, Pharm. Res.2002, 19, 1673.

19. M. M. Lunoe, A. L. Drendel, M. N. Levas, S. J. Weisman, M. Dasgupta, R. G. Hoffmann, D. C. Brousseau, Ann. Emerg. Med.2015, 66, 466.

20. M. An, H. Liu, Small2017, 13, 1700164.

21. M. S. Wallace, B. Ridgeway, E. Jun, G. Schulteis, D. Rabussay, L. Zhang, Reg. Anesth. Pain Med. 2001, 26, 229.

22. J. Gehl, Acta Physiol. Scand.2003, 177, 437.

23. A. R. Denet, R. Vanbever, V. Préat, Adv. Drug Delivery Rev.2004, 56, 659

24. M. Arruebo, R. Fernández-Pacheco, M. R. Ibarra, J. Santamaría, Nano Today2007, 2, 22.

25. J. Li, W. Xu, D. Li, T. Liu, Y. S. Zhang, J. Ding, X. Chen, ACS Nano2018, 12, 6685.

26. S. N. Murthy, S. M. Sammeta, C. Bowers, J. Controlled Release2010, 148, 197.

27. T. Neuberger, B. Schöpf, H. Hofmann, M. Hofmann, B. Von Rechenberg, J. Magn. Magn. Mater.2005, 293, 483.

28. W. Zhang, W. Xu, C. Ning, M. Li, G. Zhao, W. Jiang, J. Ding, X. Chen, Biomaterials 2018, 181, 378.

29. Y. Yang, W. Gao, Chemical Society Reviews, 2019, 48, 1465.

30. T. Wang, H. Yang, D. Qi, Z. Liu, P. Cai, H. Zhang, X. Chen, Small 2018, 14, 1702933.

31. I. Jeerapan, J. R. Sempionatto, A. Pavinatto, J. M. You, J. Wang, J. Mater. Chem. A 2016, 4, 18342.

32. W. Gao, S. Emaminejad, H. Y. Y. Nyein, S. Challa, K. Chen, A. Peck, H. M. Fahad, H. Ota, H. Shiraki, D. Kiriya, D.-H. Lien, G. A. Brooks, R. W. Davis, A. Javey, Nature2016, 529, 509.

33. A. Martín, J. Kim, J. F. Kurniawan, J. R. Sempionatto, J. R. Moreto, G. Tang, G. A. S. Campbell, A. Shin, M. Y. Lee, X. Liu, X. J. Wang, ACS Sens. 2017, 2, 1860.

34. W. Zhang, C. Ning, W. Xu, H. Hu, M. Li, G. Zhao, J. Ding, X. Chen, Theranostics2018, 8, 3331.

35. W. G. Brose, M. J. Cousins, Pain1991, 45, 145.

36. J. Mao, L. L. Chen, Pain Med.2000, 1, 7

37. A. Taddio, B. Stevens, K. Craig, P. Rastogi, S. Ben-David, A. Shennan, P. Mulligan, G. Koren, N. Engl. J. Med.1997, 336, 1197.

38. N. Reznik, R. Williams, P. N. Burns, Ultrasound Med. Biol.2011, 37, 1271.

39. C. Y. Lin, W. G. Pitt, BioMed Res. Int.2013, 2013, 404361.

40. O. Shpak, M. Verweij, H. J. Vos, N. de Jong, D. Lohse, M. Versluis, Proc. Natl. Acad. Sci. U. S. A.2014, 111, 1697.

41. D. Kagan, M. J. Benchimol, J. C. Claussen, E. Chuluun-Erdene, S. Esener, J. Wang, Angew. Chem.2012, 124, 7637.

42. F. Soto, A. Martin, S. Ibsen, M. Vaidyanathan, V. Garcia-Gradilla, Y. Levin, A. Escarpa, S. C. Esener, J. Wang, ACS Nano 2015, 1, 1522.

43. F. Soto, R. K. Mishra, R. Chrostowski, A. Martin, J. Wang, Adv. Mater. Technol.2017, 2, 1700210.

44. J. G. Riess, Artif. Cells, Blood Substitutes, Biotechnol.2005, 33, 47.

45. R. O. Bude, R. S. Adler, J. Clin. Ultrasound 1995, 23, 271.

46. M. M. Burlew, E. L. Madsen, J. A. Zagzebski, R. A. Banjavic, S. W. Sum, Radiology 1980, 134, 517.

47. R. T. Oliveira, G. R. Salazar-Banda, V. S. Ferreira, S. C. Oliveira, L. A. Avaca, Electroanalysis 2007, 19, 1189.

48. G. Yang, F. Zhao, J. Mater. Chem. C 2014, 2, 10201

49. S. Mitragotri, D. Blankschtein, R. Langer, Science 1995, 269, 850.

50. N. Huebsch, C. J. Kearney, X. Zhao, J. Kim, C. A. Cezar, Z. Suo, D. J. Mooney, Proc. Natl. Acad. Sci. U. S. A. 2014, 111, 9762.

Chapter 4. Use of robotic plataform for Decontamination

4.1 Introduction

Microrobots[1-7] are potentially promising tools for environmental remediation, specifically for accelerated decontamination of biological and chemical pollutants from water resources. The state-of-the-art motile microrobots have proven successful for the enhanced degradation of aqueous pollutants at the laboratory scale, overcoming the slow pollutant diffusion and absorption rates by reactive materials common to passive remediation methods. A major challenge in the field is to translate and scale up these microrobotic applications to relevant environmental settings by addressing limitations associated with toxic chemical fuels, short time span[22-24] and the small domain operation of externally-actuated microrobots.[25-29] One plausible solution is to develop biohybrid microrobots.[30-35] that integrate self-propelling microorganisms with functionalized synthetic nanostructures. The current generation of biohybrid platforms is based primarily on flagellated microorganisms[36-43] which survive only in delicate living conditions and may not provide sufficient fluid mixing for enhancing decontamination processes. Moreover, while enzymatically-powered micropumps[44-45] have been utilized to generate fluid mixing, they are tailored to operate under specific environmental conditions and with their respective substrates.

We report here on biohybrid microrobots whose operation can be scaled up to realistic aqueous environmental settings. Among the microorganism candidates, we selected the marine rotifer (Brachionus, size ~100-300 μm) and hence named the resulting biohybrid microrobot “rotibot”. Over millions of years, rotifers have adapted to and harvest

their energy from their environments. (e.g., puddles, rivers, lakes and ocean) They rely on the beating of their cilia bands to control the fluid flow for efficient locomotion and feeding. The microorganism engine of the resulting rotibots thus mixes the solution locally and transports it efficiently towards its functionalized mouth. The rotifer not only can serve as an extremely efficient self-propulsion engine of the biohybrid microrobot's self-propulsion engine, but can also integrate sensing capabilities that respond to environmental signals and maneuver effectively in their environment.[48-51]

We engineered the rotibot as a self-propelling microcleaner by exploiting the negative charge on its cilia surface for confining positively-charged functional particles. The generated flow field transports the functional microbeads towards the mouth and accumulating them underneath the lips. The numerous cilia outside the mouth, actuating in a coordinated cilia-stroke pattern, generate a vortex flow field near the rotibot head. The flow streamlines are closely dominated by the operation modes of the rotifer, e.g. moving or feeding, and contribute to highly efficient solution mixing around the rotibot. The experimentally observed flow streamlines correlate well with our theoretical simulations.

We fine-tuned the active decontamination sites on the microbeads to create specialized reactive microcleaner towards a dramatically accelerated pollutant degradation. Three examples of environmental remediation applications were used to demonstrate the remarkable efficiency and versatility of the new rotibot microcleaners. Lysozyme and organophosphorus hydrolase (OPH) tagged microbeads have thus been used for illustrating the enhanced enzymatic biodegradation of *E. coli* and the nerve agent methyl paraoxon, respectively. We also used ligand-modified meso-2,3-dimercaptosuccinic acid (DMSA)

Janus microbeads for improved chelation and removal of heavy metal contaminants. The high flow rate towards the mouth forces efficient transport of the pollutant solution over the reactive microbead aggregate structures that rapidly degrade the transported pollutants. Such remediation is realized in the absence of harmful fuels or external stirring, and with relative high speeds and low cost that indicate promise for scaling up cleanup processes. Our results thus illustrate that coupling functionalized nanostructures and marine rotifer offers tremendous promise for developing self-propelling fuel-free microcleaners for large-scale remediation action towards diverse environmental applications.

4.2 Experimental Methods

Marine Rotifer Preparation and Recording:

Marine rotifers (*Brachionous)* were purchased from Carolina Biological Supply and used without further treatment. A stock solution was cultured using an ocean water sample collected at La Jolla, California. Rotifers were collected from the stock culture and diluted into aliquots containing approximately 40 rotifers/mL. To record the motion of Rotifers, images and videos were taken in an inverted optical microscope (Nikon Eclipse Instrument Ti-S), coupled with 4×, 10× and 20× objectives, and a Hamamatsu digital camera C11440 and FrameLink Express software. NIS elements software was used to measure rotifer locomotion speed and mean squared displacement of tracer particles. For Propulsion experiments in different media, the rotifers were collected using an extended pipet tip (20 µL) and placed in 200 µL of the different studied Media. To calculate the mean square displacement under which different microswimmers produce, we used 1 µm

polystyrene microbeads and measured their mixing capabilities, including displacement under Brownian motion, locomotion of platymonas (Carolina Biological Supply.), locomotion of bubble propelled chemical microrockets, synthesize using template electrodeposition[61] and under rotifer Locomotion.

Microbead surface coating:

Carboxylated Fluorobeads with 1 μm in diameter (Spherotech cat no, cfp-0856-2) were used as a model for particle attachment to rotifer body. The attachment relies on electrostatic interaction. Three different coatings were used in this work. Firstly, the beads were coated with a positive charge polydopamine layer, which consisted of incubating the beads overnight with a dopamine solution (2 mg dopamine/L of 10 mM tris, pH 8.5).[52] These beads were then incubated with marine rotifer for 30 min before evaluation of attachment. Fluorescence imaging was performed using a B2 filter which allows differentiating the fluorobead and the rest of rotifer. The particle displacement image stacking was performed using Image J software and Flow trace plug-in.[62] The enzymes lysozyme and organophosphorus hydrolase were functionalized into the carboxylated fluorobeads, via activation of the carboxylic moieties using a NHS (20 mM)/EDC (10 mM) in 0.1 M MES buffer (pH 6.5) for 30 min. Next, the beads were washed and immersed in solutions containing 5 mg/mL of lysozyme or 3.5 mg/mL of organophosphorus hydrolase.

Bacteria Killing:

The antibacterial activity of rotibots was examined by analyzing *E. coli* bacteria cells (from Sigma-Aldrich, St Louis, 384 MO). *E. coli* bacteria (9.2×10^9 CFU mL^{-1}) was

mixed with 20 rotibots and lysozyme modified microbeads. The mixture was allowed to react for 5 min, and after that, the mixture was centrifuged at 14000 rpm for 10 min to isolate the bacteria pellet. The pellet was resuspended in 100 μL of a mix of Syto-9 dye and propidium iodide dye previously dissolved in water following the specifications of the L13152 LIVE/DEAD BacLight™ Bacterial Viability Kit (from Thermo Fisher Scientific). Microtubes were covered with aluminum foil and gently mixed for 20 min. Subsequently, they were centrifuged (14000 rpm for 10 min) and the pellet was resuspended in 100 μL of water for counting, taking 2 μL aliquots for obtaining the fluorescence images. All other control experiments were analyzed following the same protocol.

Nerve agent Decontamination:

The nerve agent decontamination activity was examined using 20 rotibots based on OPH- functionalized microbeads. Firstly, 40 μL of each solution (including 100 ng OPH solution) were incubated with 40 μL of methyl paraoxon. The biocatalytic degradation of the pesticide to *p*-nitro phenol was monitored by applying square wave voltammetry over the potential range from +0.30 to +1.20 V (vs Ag/AgCl), amplitude, 25 mV, and a frequency of 10 Hz. Control experiments indicated that neither the spheres nor the rotifers alone resulted any degradation.

Heavy Metal Removal:

Electrochemical experiments were carried out with a μAutolab Type II system, controlled by NOVA software version 1.11. The three-electrode system was performed in a batch system. The three electrodes consist of conventional glassy carbon (GCE),

Ag/AgCl (3 M KCl), and Pt electrodes as the working (WE), reference (RE), and counter (CE) electrodes, respectively. The GCE was polished using 3–4 μm with Al_2O_3 powder and then rinsed with ultrapure water. The electrode was then immersed in 1 M HNO_3 for 5 min to fully remove metal residues.

The square wave anodic stripping voltammetry detection was performed in a 1.5 mL electrochemical cell, containing 0.1 M acetate buffer (pH 4.5), 1 mg L^{-1} Bi^{3+}, and amounts of Cd^{2+} and Pb^{2+}. A concentration of 400 μg L^{-1} was used in the experiment to study the removal of heavy metals under different experimental conditions. After incubation with the rotibots and control experiemnts, the solution was centrifuged, the supernatant was used to perform SWV in an electrochemical cell. The preconcentration was carried out at -1.4 V for 300 s under stirring where Bi^{3+} and the target analytes were simultaneously electrodeposited on the GCE surface. After the accumulation step, the stirring was stopped. The stripping voltammogram was then recorded by applying a square-wave voltammetry (SWV) with a positive-going potential scan at a frequency of 10 Hz, an amplitude of 5 mV, and a potential step of 5 mV. The electrode was cleaned at +0.3 V for 180 s under stirring condition and followed by electrode polishing prior to the next experiment. All experiments were conducted at room temperature in air atmosphere.

4.3 Experimental Results

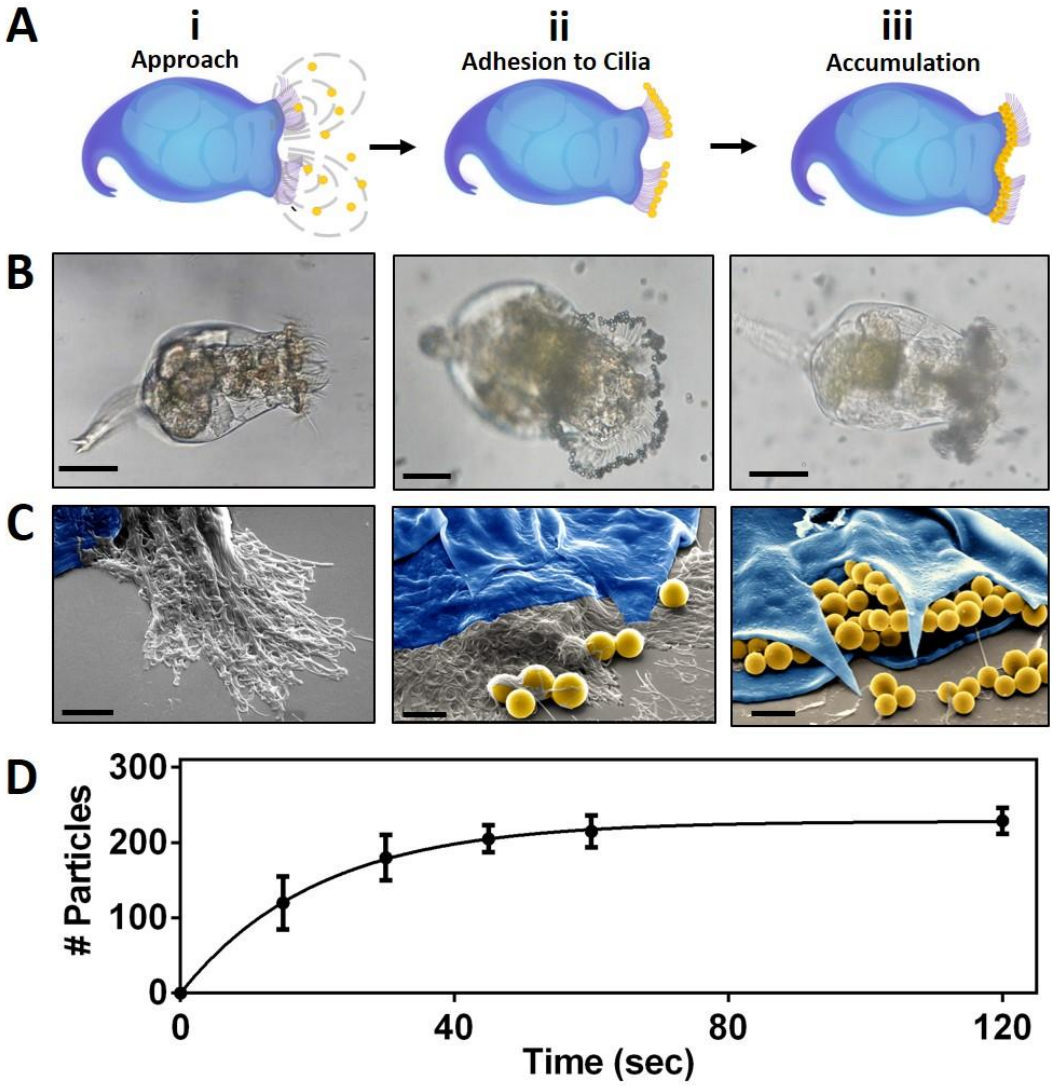

Figure 4.1. Mechanism for the formation of the rotibot: (A) scheme, (B) microscopy images and (C) scanning electron microscopy images, illustrating the steps towards rotifer (blue) uptake of the functionalized microbeads (yellow). (i) Microbeads approaching the rotifer's mouth due to a strong directional flow; (ii) upon contact with the cilia the beads adhere in their tips; (iii) the cilia within the inner lips of the rotifer accumulate the particles in that location and frees up the cilia for subsequent adhesion. (D) Time dependence of the microbead accumulation in the rotibot's mouth (n=5). Scale bars: B: 50 μm; C: 5 μm.

The rotibots were fabricated by absorbing positively-charged microbeads on the negatively-charged surface of the rotifer's cilia[47-49] and subsequently accumulating the microbeads underneath the lips via particle trapping. Figure 4.1 illustrates the attachment of the beads to the rotifer lips, by intermediate steps: (i) transport of the microbeads towards the cilia bands due to the strong flow field towards the rotifer mouth, (ii) absorption of the microbeads onto the cilia, and (iii) accumulation of the beads onto the rough surface of the inner mouth lip, (Figure 4.2) serving as a pocket that traps the microbeads.

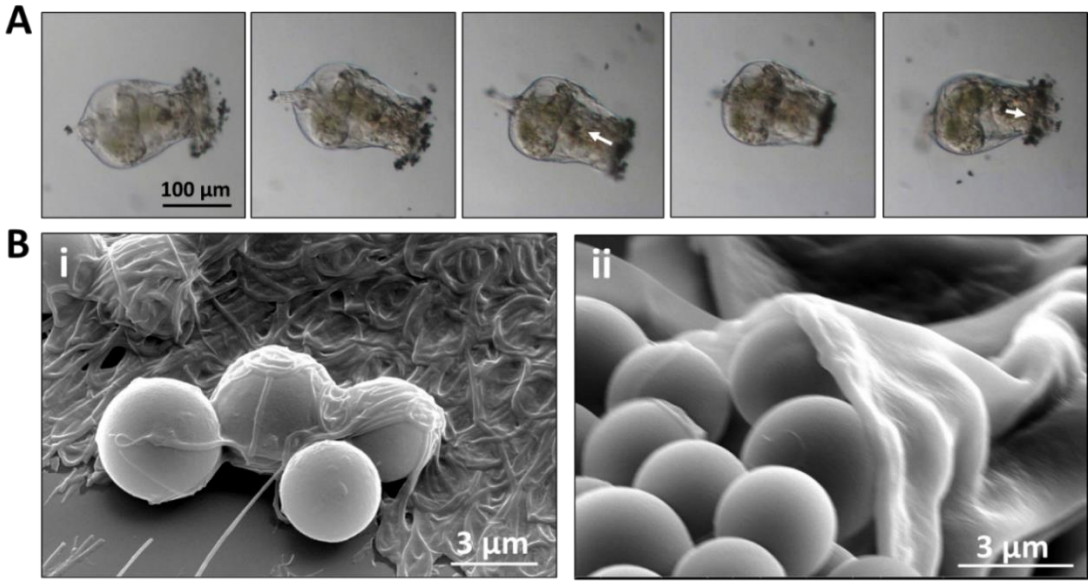

Figure 4.2. Transfer of microbeads from the cilia onto the inner mouth lip illustrated by A) time-lapse microscope images (0.3 s intervals) and B) scanning electron microscopy images of the microbeads attachment to i) cilia and ii) inside the inner mouth lip.

These accumulation steps are illustrated in the scheme of Figure 4.1A, the microscopy images of Figure 4.1B, and scanning electron microscopy images of Figure 1C. The strong electrostatic interactions between the cilia's negative charge (ζ = -12.4 mV) and the positively-charged microbeads (ζ = +59 mV) lead to the physical binding of microbeads

to the cilia. On average, the rotifer's mouth is saturated with the microbeads within approximately 120 sec (see Figure 1D). While small particles were accumulated successfully inside the rotifer mouth, particles larger than 4 μm did not show any long-lasting attachment. To study the localization of the microbead adhesion inside the rotifer mouth, we also relied on positively-charged fluorescent beads coated with a polydopamine layer. [40,52] (Figure 4.3)

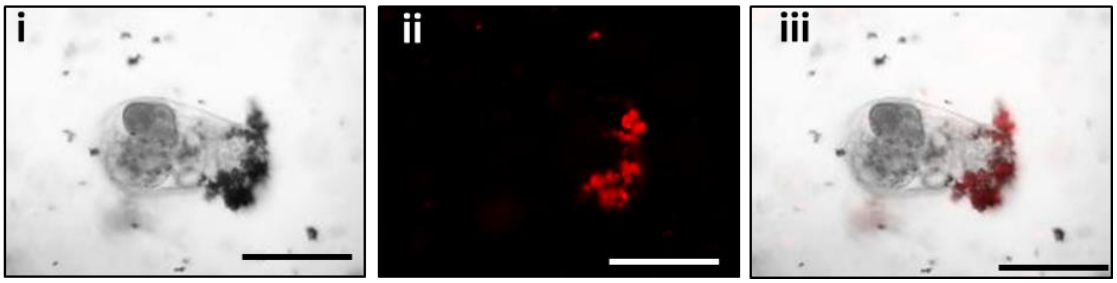

Figure *4.3*. Rotibot made out of polydopamine coated fluorescent microbeads aggregated inside rotifer's mouth. Aggregation of fluorescent beads inside rotifer's mouth illustrated by i) bright field and, ii) fluorescence microscopy images, and iii) the overlap the two. Scale bars: 100 μm

While some microbeads are dislodged upon the rapid movement of the rotibots, the majority of the microbeads remained firmly trapped in the mouth over long periods (>30 min). No microbead attachment was observed on other parts of the rotibot body. Control experiments using negatively-charged (carboxylated) microbeads and neutral polystyrene microbeads indicated negligible bead attachment to the rotifer's mouth, thereby supporting the importance of the electrostatic accumulation of the charged beads.

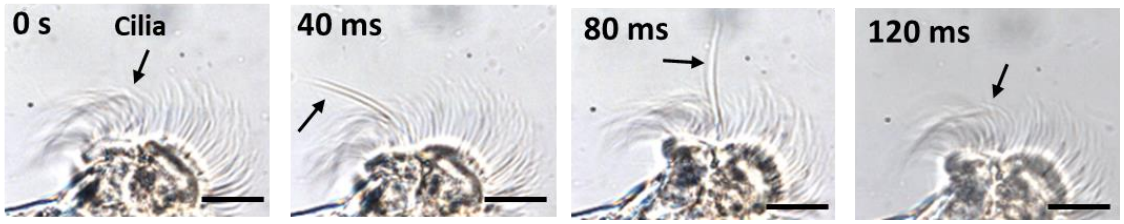

Figure 4.4. Time-lapse micrographs of a typical cilia stroke pattern, (v_0~ 451μm/s). Scale bar: 10 μm.

The locomotion of rotibot is based on the rotifers' coordinated strokes of cilia bands, which induce a tangential flow field near the head. The cilia movement involves repeated cycles of power and recovery strokes, as shown in the time-lapse micrographs in Figure 4.4. The generated flow streamlines are closely dominated by the rotifer's operation mode, such as moving or feeding, etc.[52-55] The translocation of freely-swimming rotibots allows them to transport active materials while generating disordered open streamlines and providing efficient local mixing. Figure 4.5 examines the rotibot enabled fluid mixing and hydrodynamics. Figure 4.5A displays track lines of a rotibot and a bare rotifer over a 4 s period, while Figure 4.2B shows the bar charts, corresponding to the average speed. The functional rotibots display a slightly lower speed (of 179 μm/s) compared to the bare rotifers (236 μm/s). Such rotibot movement result in higher mixing and hence significantly enhance the mass transport for decontamination. We deduced this fact by analyzing the mean-squared displacement of tracer particles and comparing with the mean-squared displacement of these particles undergoing Brownian motion, and also tracer particles in the vicinity of flagellated microorganisms or chemically-propelled synthetic micro-rockets, as shown in Figure 4.5C.

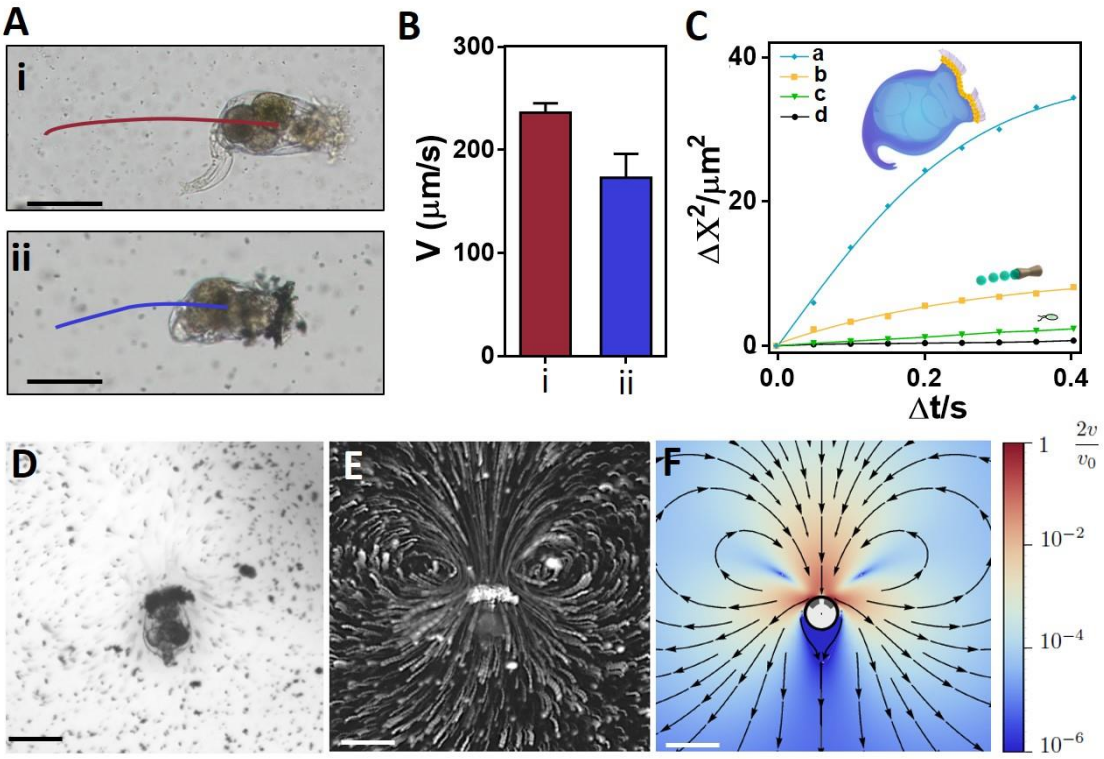

Figure 4.5. Rotibot enabled fluid mixing and hydrodynamics. (A) Images illustrating the movement of i) bare rotifer and ii) rotibot during 4 s tracking lines. (B) Average speed of the rotifer before and after modification (n=5). (C) Mean squared displacement of 3 μm tracer particles produced by (a) freely swimming rotibot, (b) chemically propelled synthetic microrocket, (c) flagellated microorganism and (d) Brownian motion. (D) Bright-field optical microscopy of a stationary rotibot in a solution containing functionalized fluorescent microbeads. (E) Visualization of vortices generated by overlapping a stack of 30 fluorescence microscopy images, corresponding to 1 second of the same rotibot. (F) Simulation of the flow field generated by a rotibot, illustrating the significant faster fluid flow near the mouth in units of maximum speed created by cilia around the rotifer. Scale bars: D-F: 100 μm.

The rotibots exhibit adaptive self-locomotion and survival in diverse aqueous environments over long periods including pond water (104 μm/s), residual water (163 μm/s), lake water (175 μm/s), pool water (176 μm/s), and seawater (179 μm/s). In addition,

freely swimming rotibots can generate localized fluid mixing and swim against the direction of a flow current in confined channels. (Figure 4.6).

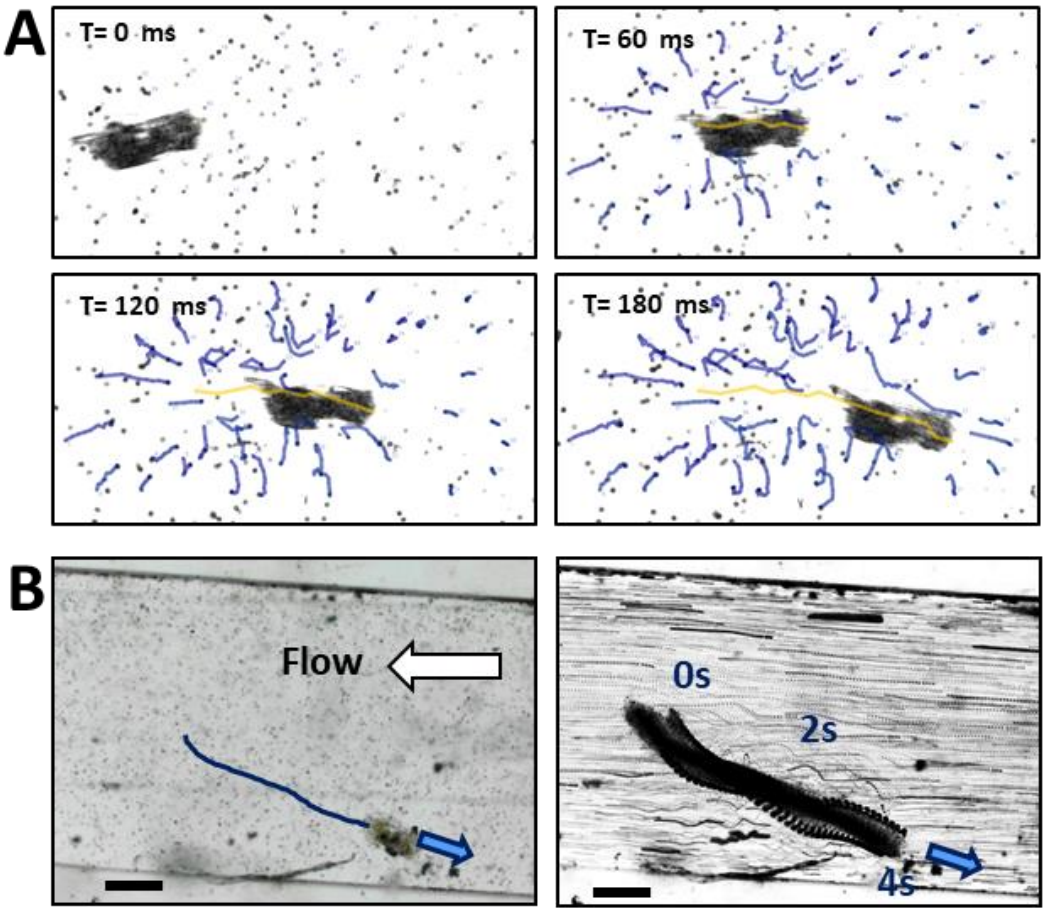

Figure 4.6. Visualization of mixing generated by freely swimming rotibot. A) Trackline illustrating the displacement of tracer particles (blue) produced by a freely swimming rotibot. B) Swimming of a rotibot (left) against the flow in a microchannel. (right) Stacking of video frames for a rotibot motion during 4. The tracer particles are 3.3 μm in diameter.

The fluid flow pattern around the rotibot changes as its rotifer engine changes from the swimming to the feeding modes. Figure 2.5D shows the bright field microscopy image

of a stationary rotibot (attached to the surface) in the feeding mode with fluorescent microbeads coated with a polydopamine layer. Figures 2.5E overlaps a stack of 30 fluorescent microscopy images (during a 1 second period) of the same rotibot. The visualized vortices are attributed to the effect of boundaries and confinement near the rotibot. For a typical microswimmer of length ~150 μm and tracer particle speed ~150 μm/s in water with density 1000 kg/m^3 and viscosity 8.90 × 10^{-4} Pa, the Reynold number is ~0.08. Thus, the flow velocity field ν follows Stokes equation:

$$\mu\nabla^2 v=\nabla p \text{ and } \nabla\cdot v=0 \qquad \text{Equation 1.}$$

The rotibot is bound to swim between two parallel horizontal glass slides and the cilia bands could generate tangential flow near the rotibot head, leading to a velocity field v_s (on the rotibot surface of ~451μm/s). The resulting flow field is shown in Figure 4.5F. Such simulation of the flow field generated by a rotibot illustrate the significant faster fluid flow near the mouth in units of maximum speed created by cilia around the rotifer. The effect of confinement and the tangential flow thus leads to the formation of vortices that are responsible for large particle displacement and efficient local mixing. The microbead aggregates thus have a significantly higher rate of exposure to solutes in the fluid, compared to microbeads suspended in the solution. Such remarkable pumping action towards the mouth forces efficient solution transport towards the confined reactive microbead aggregate structures and will be used in the following sections towards accelerated remediation processes without added fuel or external mixing.

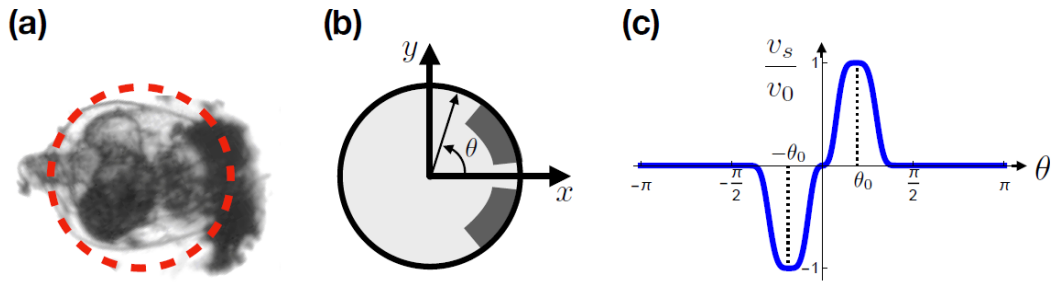

Figure 4.7. Modeling the rotibot (a) micrograph of a rotibot whose top view is approximated by a circle (dashed red line). (b) The rotibot geometry is modeled by a cylinder moving between two parallel plates (c) The effect of cilia region [dark gray bands in (b)] is modeled by non-zero velocity peaks and the rest of the rotibot surface follows no-slip boundary condition, represented by Eq. (S1) with c = 1/3.5 and d = 1/1000.

Figure 4.7 illustrates the geometry and boundary condition to model the flow field generated by the biohybrid swimmer. The rotibot (light gray) was approximated by a cylinder with the cilia bands (in dark gray) located at the front of the cylinder. The fluid below and above the rotifer with the same top view cross-section is assumed to be part of the cylinder, where the velocity field on the swimmer surface ($v_s(\theta)$) is modeled by

$$v_s(\theta) = \frac{1}{2}v_0\left[\mathrm{sgn}(\theta)\exp\left(-\frac{[\sin(\theta/2)-\sin(\theta_0/2)]^4}{d}\right) - \mathrm{sgn}(-\theta)\exp\left(-\frac{[\sin(\theta/2)-\sin(\theta_0/2)]^4}{d}\right)\right] \quad \text{Equation 2.}$$

where $\mathrm{sgn}(\theta)$ is the sign function, and v_0 is the maximum velocity induced by cilia on the swimmer surface, d determines the width of the cilia region on the rotifer, and $\theta_0 > 0$ is the location of the maximum cilia beating speed (as shown in Figure 4.7c). In the experimental setup, the rotibot is swimming between two horizontal glass slides and thus we consider two infinite horizontal planes with no-slip boundary condition. Expanding the surface velocity field in terms of its Fourier components,

$v_s(\theta) = \sum_{n=1}^{\infty} A_n \sin(n\theta)$ Equation 3.

with expansion coefficients $A_n = \frac{2}{\pi}\int_0^{\pi} v_s(\theta)\sin(n\theta)\, d\theta$, the velocity field around the rotibot is

$v(x, y; k) = \sum_{n=1}^{\infty} A_n[v_x^{(n)}\hat{x} + v_y^{(n)}\hat{y}]$ Equation 4.

where $k = (h/a)^2$ is the square of the ratio of the cylinder height h to its radius a. Also, k-dependent $v_x^{(n)}$ and $v_y^{(n)}$ are the x and y components of the velocity field for the Fourier mode n corresponding to the surface velocity field $\sin(n\theta)$ on the swimmer surface. We obtained $v_x^{(n)}$ and $v_y^{(n)}$ by adapting the solution from Pepper *et. al.* in polar coordinates to Cartesian coordinates system.

For a typical rotibot of effective radius $a \cong 100$ μm and the distance between the horizontal parallel glass slides $h \cong 300$ μm we have $k = (h/a)^2 \cong 9$. Figure 4.8, illustrates (a) the experimental flow observations, (b) the theoretical flow pattern and (c) the overlap of both images, which indicates that the result of the theoretical model is consistent with the experimental observation.

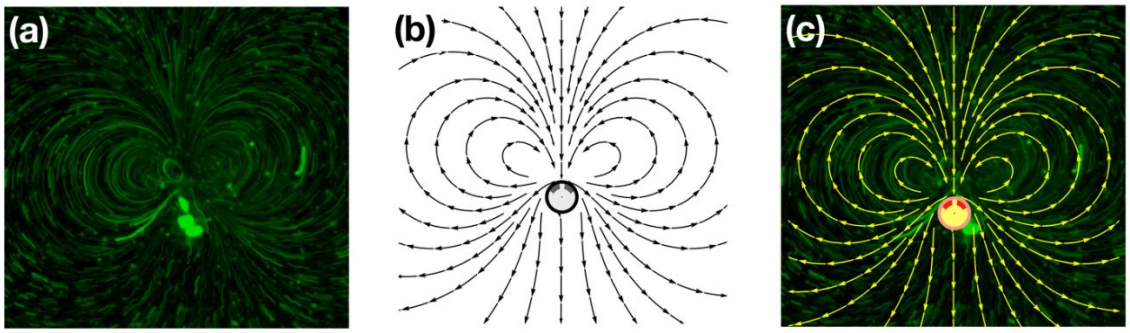

Figure 4.8. Rotifer fluid mixing experiment and modeling. (a) Experimental visualization of vortices made by stacking fluorescence microscopy images of fluorescent dispersed in the fluid around the rotifer. (b) Simulation of the flow field generated by a rotifer, illustrating the vortices around its head. (c) Overlap of experimental and theoretical streamlines.

The remarkably enhanced fluid dynamic associated with the rotibot platform offers considerable promise for increasing the efficiency of a variety of decontamination processes. The major benefits of such built-in sample solution mixing have been illustrated towards the decontamination of diverse environmental pollutants, including bacteria (*E. coli*), nerve agent (methyl paraoxon) and heavy metal ions (Cd and Pb) from aqueous solution. Such greatly enhanced decontamination has been realized by functionalizing the microbeads with enzymes or chelating agents, which serve as active sites for specific remediation tasks. The rotifer exposure to the different pollutants did not affect their movement or viability during the experiments.

The rotibots were evaluated initially as potential antibacterial microcleaners. For this purpose, microbeads were functionalized with lysozyme enzymes capable of cleaving glycosidic bonds of peptidoglycans present in the cell wall of different bacteria.[29,56] Details

of the functionalization protocols of the microbeads are described in the experimental section. Figure 4.9 displays a schematic of the lysozyme-modified microbeads attached to the rotibot. The mixing effect of the directed flow field produced near the rotibot's mouth lead to intensified bacteria-lysozyme contacts and to a greatly improved antibacterial efficiency. Figure 4.9B shows SEM images of *E. coli*, taken before and after a 5 min treatment with the lysozyme-modified rotibot. These images illustrate a notable change in bacteria morphology upon degradation of the bacteria membrane. The antibacterial capacity of the rotibots were quantified using a bacterial viability commercial kit, based on the use of two dyes that estimate the numbers of viable and nonviable bacteria. We compared the antibacterial efficiency under different experimental conditions, negative control, bare rotifers, lysozyme-microbeads, and lysozyme-modified rotibots.

The bacterial-killing efficiency of each experimental condition is illustrated in the graph of Figure 4.9C. While there was a negligible bactericidal effect using the water alone (0%) and bare rotifers (1%) controls, the biohybrid approach results in an 8-fold higher bacteria killing efficiency (83%), compared to the lysozyme microbeads alone (10.2%). The fluorescent images of Figure 4.9D illustrate the total of living *E. coli* (i, in green) and dead *E. coli* (ii, in red), obtained after the corresponding treatment. The rotibot facilitated the elimination of most of the bacteria population within less than 5 min (d), compared to the high bacteria survival rate observed in different control experiments (a-c).

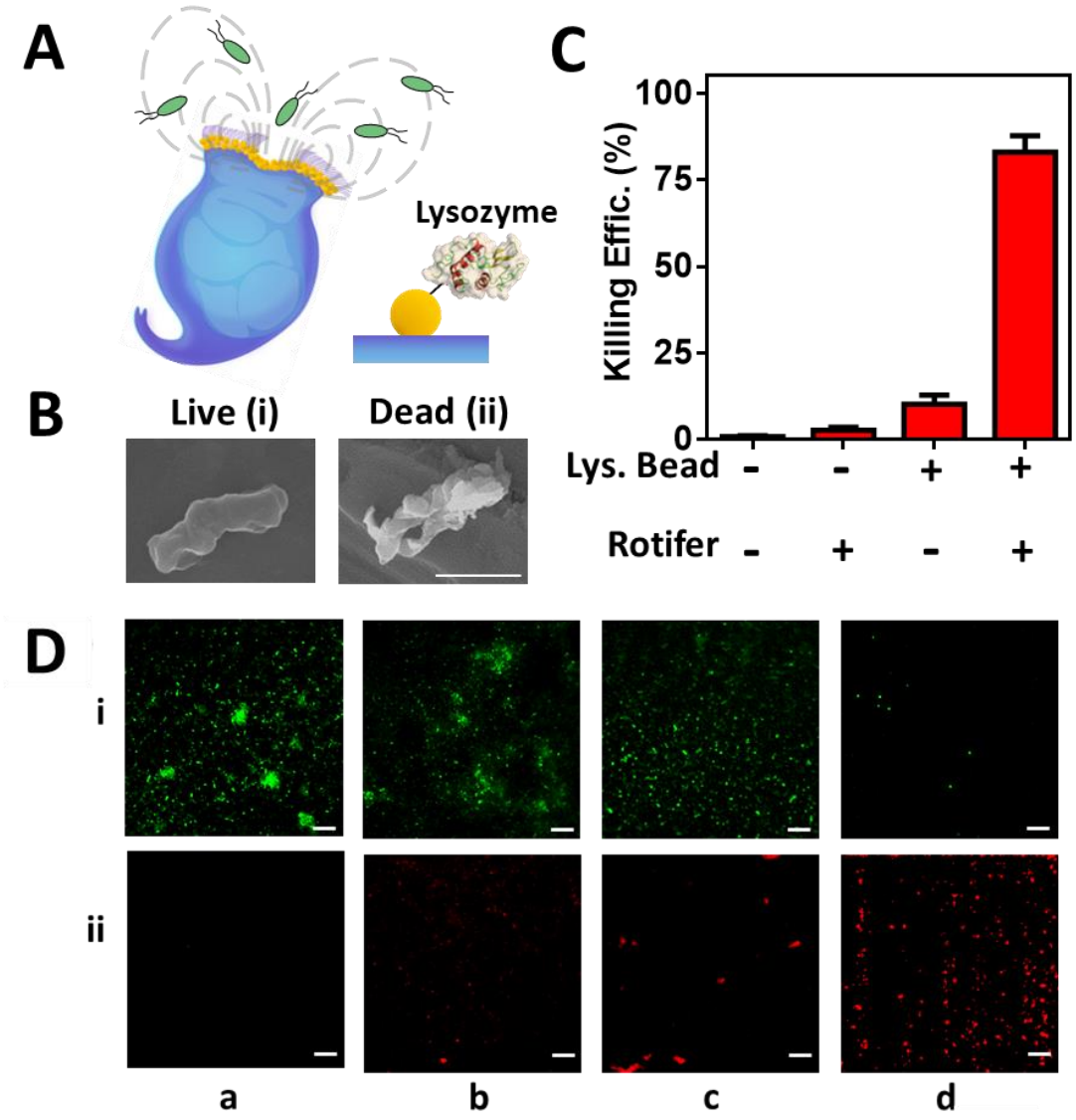

Figure 4.9. Lysozyme-modified rotibot-based antibacterial treatment. (A) Schematic illustration of lysozyme-microbeads responsible for killing E. coli bacteria. (B) SEM micrographs illustrating (i) live E. coli and (ii) dead E. coli. before and after the treatment with lysozyme-modified rotifers, respectively. Scale bars, 2μm. (C) Statistical plot showing the E. coli bacteria killing efficiency by the different treatment conditions. (D) Fluorescence images illustrating live (in green, top) and dead (in red, bottom) E. coli after 5 min treatment under different conditions including: negative control, bare rotifer, lysozyme-microbeads, and lysozyme-modified rotibot. (a-d) Scale bars, 50 μm. Experimental conditions: bacteria, 9.2×10^9 CFU mL^{-1}; rotifer, 20 units per control; antibacterial treatment time, 5 min.

The versatility of the new rotibots decontamination platform was illustrated also towards biocatalytic degradation of organophosphorus pesticides. Such rotibot-based accelerated enzymatic treatment processes relied on the use of organophosphorus hydrolase (OPH) functionalized microbeads in connection to the organophosphorus methyl paraoxon.[57] Figure 4.10A i displays a schematic of the OPH-modified microbead attached to the rotibot. Electrochemical square-wave voltammetry (SWV) technique was used to measure the nitro-phenolic byproduct of the OPH enzyme hydrolyzation of methyl paraoxon.[58,59] The voltammograms in Figure 410A ii represent different incubation conditions with a methyl paraoxon solution, including (a) negative control, (b) bare rotifers, (c) static OPH-microbeads and (d) OPH-modified rotibots. The nitro-phenol voltammetric peak, observed at +0.795 V, is proportional to the amount of hydrolyzed nerve agent, and thus reflects the efficiency of the methyl paraoxon degradation process under the different treatment conditions, as summarized in the graph bar of Figure 4.10A iii. The OPH biocatalytic degradation efficiency increased significantly (by 8-fold) using rotibots when compared to static OPH-microbeads (29.6 vs 3.6 μA, respectively).

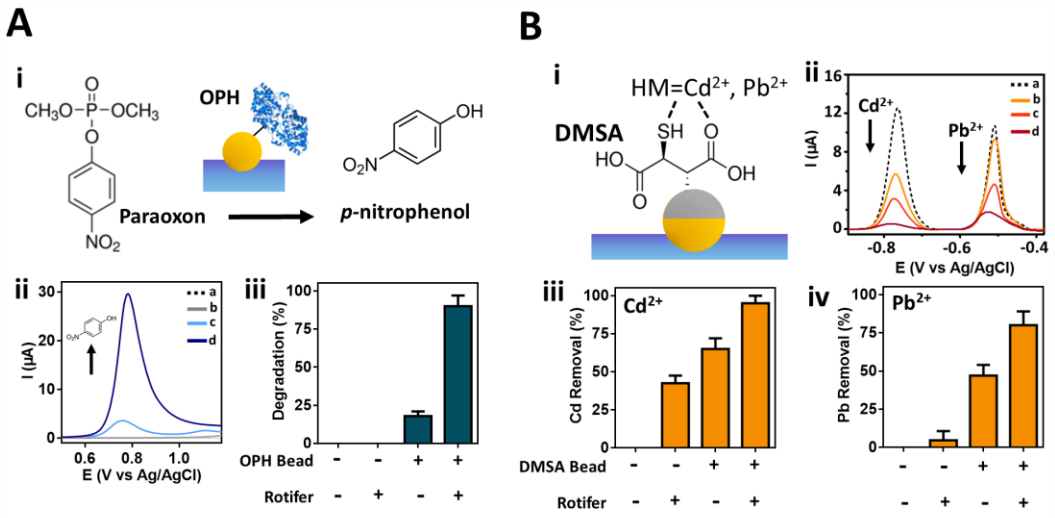

Figure 4.10. Use of rotibots for chemical pollutant remediation. (A) OPH-microbeads modified rotibots for nerve agent decontamination. (i) Schematic illustrating the OPH-based degradation of methyl paraoxon. (ii) Square wave voltammetry (SWV) for decontamination after: negative control, bare rotifer, OPH-microbeads, and OPH-modified rotibot (a-d). (iii) Statistical plot showing the degradation efficiency by the different treatments (n=5). (B) DMSA-Janus microbeads modified rotibots for heavy metal removal. (i) Schematic illustrating DMSA-based chelation of heavy metals. (ii) SWVs for $Cd2^{+}$ and $Pb2^{+}$ presence after: negative control, bare rotifer, DMSA-microbeads, and DMSA-modified rotibot. (a-d) Statistical plot showing the removal efficiency of (iii) $Cd2^{+}$ and (iv) $Pb2^{+}$ by the different treatments (n=3).

The new rotibots platform offers also a significant improvement in the removal of heavy metals from polluted water, in connection to rotifers modified with DMSA-functionalized Janus beads. The scheme in Figure 4.10B i shows the mechanism of heavy metal removal the by DMSA ligand via metal chelation.[60] Cadmium and lead concentrations were measured simultaneously using anodic stripping square-wave voltammetry (SWV) which can detect traces of heavy metals. The advantages of the DMSA-functionalized rotibot were illustrated by incubating the heavy metal solution for 30 min with (a) negative control/buffer, (b) bare rotifers, (c) only DMSA-functionalized

beads, and (d) DMSA-modified rotibots. The resulting SWVs, shown in Figure 4.10 B ii, display two distinct oxidation peaks. The successful simultaneous detection of two heavy metals displays a large peak-to-peak separation between the stripping peaks at -0.85 and -0.50 V, corresponding to $Cd2^{+}$ and $Pb2^{+}$ions, respectively. These peak current signals are proportional to the heavy metal solution concentrations. Figure 4.10B iii and iv illustrate the removal efficiency of $Cd2^{+}$ and $Pb2^{+}$ by the DMSA-functionalized rotibot. The hybrid rotifer offers a significantly higher heavy metal removal efficiency compared to unmodified rotifers or static DMAS particles. The unmodified rotifers also presented some metal removal capability due to absorption of heavy metals into their body. Overall, the rotibots presented a substantially higher heavy metal removal when compared to bare rotifers or to the DMSA particles combined, suggesting a favorable synergistic effect of the large-scale mixing, rather than additive results.

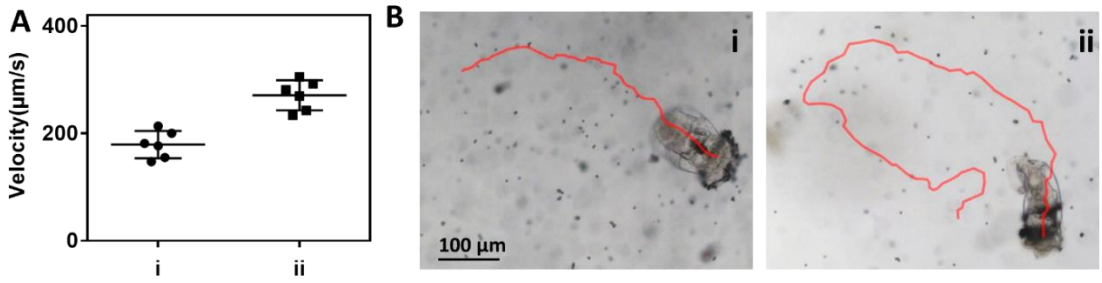

Figure 4.11. Increased motility of rotibot under influence of caffeine. A) Graph illustrating the average rotibot speed i) before and ii) after caffeine spike (20 mM). B) Images illustrating the movement of i) rotibot under typical environment and ii) rotibot under the effect of caffeine.

4.4 Conclusions

We have presented the use of biohybrid rotibots as efficient environmental microcleaners, with marine rotifers serving as the engine of the microrobot. Functionalized microbeads have been confined within the rotifer mouth via electrostatic interaction and particle trapping. The reactive microbeads are subjected to a remarkably high localized fluidic flow, generated by the cilia strokes, that leads to greatly enhanced decontamination processes. Such operation is realized in the absence of external mixing force or harmful fuels, and with relative high speeds and low cost that indicate promise for scaling up remediation processes. The experimentally observed rotibot-enhanced fluid dynamics correlates well with theoretical simulations. Such intrinsic and effective micropumping action towards the entrapped functionalized microbeads results in efficient decontamination processes, as was demonstrated towards diverse environmental pollutants, including *E. coli* bacteria, OP nerve agents and heavy metals such as lead or cadmium. Future decontamination efforts should replace the plastic (latex and polystyrene) microbeads, utilized in this proof-of-concept study, with biodegradable functional microparticles. Such ability to modify and functionalize microorganisms introduces new possibilities for preparing eco-friendly bio-bots and to accelerate a wide range of decontamination processes. Such application would benefit also from the micro swimmer response to certain biomolecules, such as caffeine, that increases their velocity (Figure 4.11), which could prove beneficial for diverse applications. The rotibot biohybrid platform thus holds a considerable promise for environmental remediation and defense neutralization applications.

Chapter 4 is based, in part, on the material as it appears Advanced Funtional Materials, 2019, Fernando Soto, Miguel Angel Lopez‐Ramirez, Itthipon Jeerapan, Berta Esteban‐Fernandez de Avila, Rupesh Kumar Mishra, Xiaolong Lu, Ingrid Chai, Chuanrui Chen, Daniel Kupor, Amir Nourhani, Joseph Wang. The dissertation author was the primary investigator and author of this paper.

4.5 References

1. J. Wang, Nanomachines: Fundamentals and applications, Wiley-VCH: Weinheim, Germany, 2013.

2. W. Wang, W, Duan, S. Ahmed, T.E. Mallouk, A, Sen, Nano Today. 2013, 8, 531.

3. M. Luo, Y, Feng, T, Wang, J. Guan, Adv. Funct. Mater. 2018, 28, 1706100.

4. C. Chen, F. Soto, E. Karshalev, J. Li, J. Wang, Adv. Funct. Mater. 2018, 1806290.

5. L.K. Abdelmohsen, F. Peng, Y. Tu, D.A. Wilson, J. Mater. Chem. B. 2014, 2, 2395.

6. K. Kim, J. Guo, Z. Liang, D. Fan, Adv. Funct. Mater. 2018, 28, 1705867.

7. P. Yánez-Sedeño, S. Campuzano, J. Pingarrón, Appl Mater Today. 2017, 9, 276.

8. J. Parmar, D. Vilela, K. Villa, J. Wang, S, Sánchez. J. Am. Chem. Soc. 2018, 140, 9317.

9. J Orozco, L.A. Mercante, R. Pol, A. Merkoçi, J. Mater. Chem. B. 2016, 4, 3371.

10. W. Gao, J. Wang, ACS Nano. 2014, 8, 3170.

11. A. Nourhani, D. Brown, N. Pletzer, J. G. Gibbs, Adv Mat. 2017, 29, 1703910.

12. B. Jurado-Sánchez, M. Pacheco, R. Maria-Hormigos, A. Escarpa, Appl Mater Today. 2017, 9, 407.

13. J. G. S. Moo, M. Pumera, Chem. Eur. J, 2014, 21, 58.

14. V.V. Singh, F. Soto, K. Kaufmann, J. Wang, Angew. Chem. Int. Ed. 2015, 127, 6896.

15. J. Parmar, D. Vilela, E. Pellicer, D. E.-D. L. Ojos, J. Sort, S. Sánchez, Adv. Funct. Mater. 2016, 26, 4152.

16. R. Kumar, M. Kiristi, F. Soto, J. Li, V.V. Singh, J. Wang, RSC Adv. 2015, 5, 78986.

17. S.K. Srivastava, M. Guix, O.G. Schmidt, Nano Lett. 2015, 16, 817.

18. Z. Lin, Z. Wu, X. Lin, Q. He, Chem. Eur. J. 2015, 22, 1587.

19. T. Maric, C.C. Mayorga-Martinez, B. Khezri, M.Z.M. Nasir, X. Chia, M. Pumera, Adv. Funct. Mater, 2018, 28, 1802762.

20. Maria-Hormigos, B. Jurado-Sánchez, A. Escarpa, Adv. Funct. Mater. 2017, 1704256.

21. H. Wang, M. G. Potroz, J. A. Jackman, B. Khezri, T. Marić, N.-J. Cho, M. Pumera, Adv. Funct. Mater. 2017, 27, 1702338.

22. C. Chen, E. Karshalev, J. Li, F. Soto, R. Castillo, I. Campos, F. Mou, J. Guan, J. Wang, ACS Nano. 2016, 10, 10389.

23. D. Vilela, M.M Stanton, J. Parmar, S. Sanchez, ACS Appl. Mater. Interfaces. 2017, 9, 22093.

24. J. Li, V.V. Singh, S. Sattayasamitsathit, J. Orozco, K. Kaufmann, R. Dong, W. Gao, B. Jurado-Sanchez, Y. Fedorak, J. Wang, ACS Nano. 2014, 8, 11118.

25. Q. Zhang, R. Dong, Y. Wu, W. Gao, Z. He, B. Ren, ACS Appl. Mater. Interface. 2017, 9, 4674.

26. F. Soto, G.L. Wagner, V. Garcia-Gradilla, K.T. Gillespie, D.R. Lakshmipathy, E. Karshalev, C. Angell, Y Chen, J. Wang, Nanoscale. 2016, 8, 17788.

27. M. Hoop, Y. Shen, X.Z. Chen, F. Mushtaq, L.M. Iuliano, M.S. Sakar, A. Petruska, M.J. Loessner, B.J. Nelson, S. Pané, Adv. Funct. Mater. 2016, 26, 1063.

28. B. Esteban-Fernández de Ávila, P. Angsantikul, D.E. Ramírez-Herrera, F. Soto, H. Teymourian, D. Dehaini, Y. Chen, L. Zhang, J. Wang, Sci. Robot. 2018, 3, eaat0485.

29. M. Kiristi, V.V. Singh, B. Esteban-Fernández de Ávila, M. Uygun, F. Soto, D.A. Uygun, J. Wang, ACS Nano. 2015, 9, 9252.

30. S. Palagi, P. Fischer, Nat Rev Mat. 2018, 3, 113.

31. H. Wang, M. Pumera, Adv. Funct. Mater. 2018, 28, 1705421

32. K. Bente, A. Codutti, F. Bachmann, D. Faivre, Small, 2018, 14, 1704374.

33. Z. Hosseinidoust, B. Mostaghaci, O. Yasa, B.W. Park, A.V. Singh, Adv. Drug Deliv. Rev., 2016, 106, 27.

34. H. Xu, M. Medina-Sánchez, V. Magdanz, L. Schwarz, F. Hebenstreit, O.G. Schmidt, ACS Nano, 2017, 12, 327.

35. M. Nagai, H. Asai, H. Fujita, Mech Eng. 2014, 1, MN0038.

36. M.M. Stanton, B.W. Park, D. Vilela, K. Bente, D. Faivre, M. Sitti, S. Sanchez, ACS Nano. 2017, 11, 9968.

37. A.V. Singh, Z. Hosseinidoust, B.W. Park, O. Yasa, M. Sitti, ACS Nano. 2017, 11, 9759.

38. B.W Park, J. Zhuang, O. Yasa, M. Sitti, ACS Nano. 2017, 11, 8910.

39. O. Felfoul, M. Mohammadi, S. Taherkhani, D. De Lanauze, Y.Z. Xu, D. Loghin, S. Essa, S. Jancik, D. Houle, M. Lafleur, L. Gaboury, Nat Nanontechnol. 2016, 11, 941.

40. M.M. Stanton, BW. Park, A. Miguel-López, X. Ma, M. Sitti, S. Sánchez, Small. 2017, 13, 1603679.

41. Y. Alapan, O. Yasa, B. Yigit, I. C. Yasa, P. Erkoc, M. Sitti, Annu Rev Control Robot Auton Syst. 2018, 2.

42. O. Yasa, P. Erkoc, Y. Alapan, M. Sitti, Adv Mat. 2018, 30, 1804130.

43. F. Soto, R. Chrostowski, Front. Bioeng. Biotechnol. 2018, 6, 170.

44. S. Sengupta, D. Patra, I. Ortiz-Rivera, A. Agrawal, S. Shklyaev, K.K Dey,U. Córdova-Figueroa, T.E. Mallouk, A. Sen, Nat Chem. 2014, 6, 415.

45. A. C. Hortelão, R. Carrascosa, N. Murillo-Cremaes, T. Patiño, S. Sánchez, ACS Nano. 2018, 13, 429.

46. C.G. Wilson, P.W. Sherman, Science. 2010, 327, 574.

47. A. Krisko, M. Leroy, M. Radman, M. Meselson, Proc. Natl. Acad. Sci. 2012, 109, 2354.

48. R.D. Holbrook, K.E. Murphy, J.B. Morrow, K.D. Cole, Nat Nanotechnoly. 2008, 3, 352.

49. H.U. Dahms, A. Hagiwara, J.S. Lee, Aquat. Toxicol. 2011, 101, 1.

50. C. Ricci, Hydrobiologia. 2017, 796, 1.

51. D.B.M. Welch, M. Meselson, Science. 2000, 288, 1211.

52. H. Lee, S.M. Dellatore, W.M. Miller, P.B. Messersmith, Science. 2007, 318, 426.

53. T. Kiørboe, H. Jiang, R.J. Gonçalves, L.T. Nielsen, N. Wadhwa, Proc. Natl. Acad. Sci. 2014, 111, 11738.

54. R.E. Pepper, M. Roper, S. Ryu, P. Matsudaira, H.A. Stone, J. Royal Soc. Interface. 2009, 7, 851.

55. W. Gilpin, V.N. Prakash, M. Prakash, Nat Phys. 2017, 13, 375.

56. B. Thallinger, E.N. Prasetyo, G.S Nyanhongo, G.M. Guebitz, Biotechnol J. 2013, 8, 97.

57. R.D. Richins, I. Kaneva, A. Mulchandani, W. Chen, Nat biotechnol. 1997, 15, 984.

58. F. Soto, R.K Mishra, R Chrostowski, A. Martin, J. Wang, Adv. Mater. Technol. 2017, 2, 1700210.

59. S. Cinti, G. Valdés-Ramírez, W. Gao, J. Li, G. Palleschi, J. Wang, Chem. Commun. 2015, 51, 8668.

60. D.A. Uygun, B. Jurado-Sánchez, M. Uygun, J Wang, Environ Sci-Nano. 2016, 3, 559.

61. A. Jodra, F, Soto, M.A. Lopez-Ramirez, A. Escarpa, J. Wang, Chem. Commun. 2016, 52, 11838.

62. W. Gilpin, V.N. Prakash, M. Prakash, J. Exp. Biol. 2017, 220, 3411.

Chapter 5- Summary and Perspectives

5.1 Summary

In this dissertation, the research has been focused on demonstrating the unique capabilities of micro/nanorobotic systems. The principal achievements of this dissertation include:

1) Development of a motile platform for transport and release of cargo based on ultrasound powered microengines. This work demonstrated that shape and density asymmetry are the most relevant design parameters required to provide the propulsive force required for translational motion. Moreover, magnetically guided motion and "on-the-move" capture and transport of multiple cargoes; and internalization and movement inside live MCF-7 cancer cells, were demonstrated.
2) A microballistic platform for the application of mechanical force at small scales, and enchased tissue penetration. An actuation mechanism was developed taking advantage of acoustic droplet vaporization to eject nanobullets at high speeds. The use of arrays of microcannons was used towards mechanochemical blood clot degradation and enhancing drug permeability through the epidermis.
3) A biohybrid microrobotic for environmental remediation, by integrating functionalized microbeads within a motile microorganism (Rotifer) We demonstrated that having built-in sample solution mixing with active materials could improve the decontamination of environmental pollutants, including bacteria (*E. coli*), nerve agent (methyl paraoxon) and heavy metal ions (Cd and Pb) from aqueous solutions.

5.2 Perspectives

In summary, we have presented the challenges and potential advantages of Micro/nanorobots platforms towards performing diverse tasks. These recent accomplishments only show initial steps toward the design of reliable and versatile micro/nanorobots. A number of design permutations can be imagined from the broad scope of propulsion mechanisms and available materials which can lead to promising next-generation nano/micro robotics.

Nevertheless, additional efforts should be devoted towards developing more diverse types of actuation mechanisms that adapt to dynamic changes in the environment in order to make the use of nanomotor in everyday life a reality. To address this challenge, we require new perspectives on materials selection, morphology design, and the purpose of the micro/nanorobot, as their use and design should offer synergistic advantages to achieve functionalities not possible with large scale robots.

We envision that in the future, micro/nanorobot swarms would be capable of collective transport motion and dynamic behavior change upon sensing different environment clues. Moreover, the in -vivo imaging and localization of nanomotor groups should be considered a critical component of design, though this area has been understudied in the literature. The integration of contrast agents' materials in nanomotor designs could allow us to see them operating inside the body. For example, a combination of ultrasound contrast materials could allow for the rapid localization of populations of nanomotors, while a higher resolution technique such as magnetic resonance imaging (MRI)

could be used for individual nanomotor localization, thus leading to precision localized microsurgery and targeted drug delivery.

As our understanding of the design of micro/nanorobotics platforms expands, it becomes feasible to utilize the inherent capabilities of these machines for practical applications. “Intelligent” hybrid micromotors could perform advanced functions in the presence of a hybrid trigger that are not only aimed at locomotion. For example, stimuli such as light or ultrasound can power the micro/nano while also manifesting as excellent triggers for many advanced functions, such as ultrasound triggered drug release or photocatalytic pollutant degradation.

Despite the existing challenges, the most exciting prospect of micro/nanorobots relies on their reliable and controllable propulsion behaviors in relevant environments media. Improved understanding of the design and operation of micro/nanorobots will facilitate the development of highly efficient and powerful artificial micromachines for complex operations in diverse real-life environments. In the not-so-distant future, we envision that with future efforts in Micro/nanorobots design could provide affordable, robust, and versatile tools, ushering in the dawn of a new technological revolution.

Chapter 5.2 is based, in part, on the material as it appears in Advanced Functional Materials, 2019, by Chuanrui Chen, Fernando Soto, Emil Karshalev, Jinxing Li, Joseph Wang. The dissertation author was the primary investigator and author of this paper.